UNIVERSITÀ DEGLI STUDI DI NAPOLI FEDERICO II

International PhD Program on:

Novel Technologies for Materials,

Sensors and Imaging

XXIV cycle

Realization and optimization of organic electronic devices manufactured by innovative technique: inkjet printing

Immacolata Angelica Grimaldi

Tutors: Dr. Fulvia Villani

Dr. Antonio Cassinese

…to angels…

This thesis describes the research activity of I.A.Grimaldi during the three years of the International PhD program on Novel Technologies for Materials, sensors and Imaging (TIMSI – XXIV cicle)- University of Naples “Federico II” (Italy). The activity was performed at ENEA – Portici Research Center in “Nanomaterials and Device Technology” was supported by Italian Ministry of Economic Development in the framework of the Operating Agreement with ENEA for the Research on the Electric System and Technologies and Research for the application of polymers in electronics devices TRIPODE project financed by the University and Research Ministry.

TABLE OF CONTENTS

LIST OF FIGURES

INTRODUCTION

Inkjet printing is a nascent technology that is evolving from text and graphic printing into a major topic of scientific research and R&D, where it can be used as a highly reproducible non-contact patterning technique to deposit liquid functional materials at high speed on either small or large areas of flexible and non-flexile substrates. It is a low cost technique because minimizes the waste products and reduces the process steps.

Nevertheless, the inkjet printing technology has some intrinsic limits, mainly related to the drying process of the printed droplet. In detail, during the drying process the fast evaporation of the solvent at the contact line induces an outward convective flow of the solute to compensate the evaporation losses and, in turn, transports the suspending solute to the edge region. This effect is known as “coffee-stain effect”.

Objective of this PhD thesis was to analyze the critical states of this deposition method and to identify the working parameters for optimizing the deposition conditions. The study on the ink formulation through the definition of its chemico-physical properties, on the wetting of the ink/substrate system through the employment of surface treatments, on the ink processing through the definition of the printing parameters supplies the fundamental elements for controlling the droplet drying and, hence, the quality of the printed material.

The printing parameters act differently on different ink/substrate systems. Therefore, studying the optimization of the deposition for different applications allows to understand how the printing conditions differently affect the working of different devices. In particular, the research activity pertains the employment of the

inkjet printing (IJP) technology for optical and electronic applications, specifically focusing on the realization of optical structures, like microstructuring and microlenses, and organic electronic devices, such as volatile organic compounds (VOCs) sensors, organic field effect transistors (OFETs) and organic solar cells (PSC).

The thesis is organized as follows.

In the first chapter, a brief introduction on the inkjet printing technique and on the employment of the piezoelectric drop-on-demand technology for the organic electronic is given. In particular, a study on the conductor and semiconductor properties of organic materials and on the optical grade polymer is also presented.

In the second chapter, a study on the printing deposition conditions of a conducting polymer nanocomposite material for sensing application is performed. The influence of geometry and thickness of the sensing material on the performances of VOC chemiresistive sensor is discussed. Moreover, a study on plasma treatments (O_2 and CF_4) to improve the wetting of the ink on different substrates (glass, PET and glossy paper) is also carried out. The reported analysis is aimed to correlate the uniformity and morphology of the printed active films to their sensing properties in presence of organic vapours.

The third chapter is dedicated to optical applications and, in particular, to the realization of microlenses and the polymer microstructuring by printing solvent or solvent mixture onto a soluble polymer layer. In this last case, the effects of the substrate temperature, the number of the printed droplets and the chemico-physical properties of the solvents on the geometrical parameters of the microstructures are analyzed. Concerning the microlenses realized by additive deposition of a polymer material, the effects of the ink viscosity and solvents on the optical quality of the microstructures is studied by interferometeric analysis based on a Mach-Zehnder system.

The fourth chapter is focused on the realization of n-type organic field effect transistors (OFETs) by printing Perylene Diimide semiconductor. The developed study is aimed at optimizing the ink chemico-physical properties and the printing parameters in order to improve the uniformity and crystalline structure of the printed

layer. Moreover, the electrical characteristics were analyzed allowing to understand as the control of the molecular organization can affect the device performances.

The fifth chapter pertains the realization of organic solar cells by printing the active layer P3HT:PCBM. The effects of the printing parameters on the power conversion efficiency of devices prepared with different solvents and solvent mixtures are investigated through morphological and electrical analyses. The study on how the printing parameters suitably combined with the volatility properties of the solvents influence the device electrical performances is reported. Moreover, the analysis that shows how these working parameters affect the phase separation between the two components of the active blend is also discussed.

CHAPTER 1
INKJET PRINTING TECHNOLOGY FOR THE ORGANIC ELECTRONICS

Inkjet printing is a very promising technology in the scientific research field for its main characteristics such as high reproducibility, non-contact patterning, high speed and high quality deposition on both small and large areas.

This technique is a cost-effective and flexible method for the deposition of functional fluids, in the form of polymer solution and pure solvents or solvent mixtures, onto various surfaces and substrates. Some examples of functional materials include metal inks, conductive and semiconductive polymers, surface coating, proteins and nanoparticles. The versatility of the inkjet printing is highlighted in several research areas such as chemical, mechanical, optical and life sciences and in a wide range of applications like electronics, opto-electronics and displays.

The present chapter provides a literature survey that describes the main features of inkjet printing technique and a more deepened overview on the inkjet printing category used in this thesis research. Moreover, an introduction to the methodologies for the formulation of the ink and for the modification of the ink/substrate wetting are also mentioned. Finally, an outline on the organic electronics and, in particular, a comprehensive survey of conductor and semiconductor materials, and optical grade polymer are also provided.

1 Inkjet printing techniques

The inkjet technology can be divided in two main classes: continuous inkjet (CIJ) and drop on demand inkjet (DOD). These two main categories can be further divided into other subcategories as shown in Figure 1.1 depending on the different techniques for applying the ink to the substrate.

Continuous inkjet is often used in printers for large-scale production that needs of high-speed printing. The operating principle of a continuous inkjet system is based on the continuous production of the drops during the printing. There are three main categories for this printing technique: Binary Deflection, Multi-Deflection and Hertz.

In the drop on demand technology, the droplets are only generated when required. Four types of drop on demand technologies are available to create a drop: Piezoelectric, Thermal, Electrostatic and Acoustic inkjet.

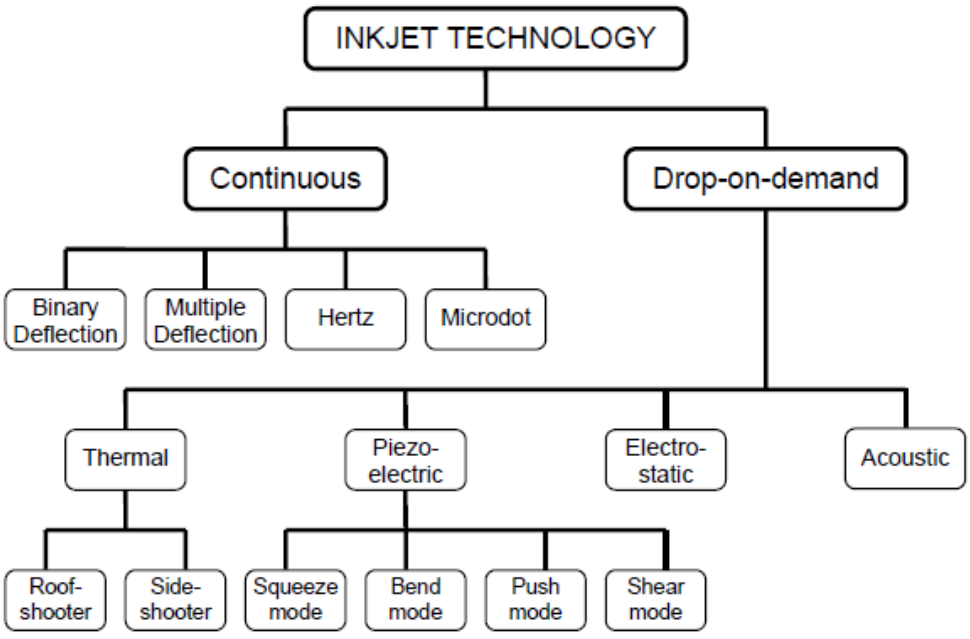

Figure 1.1 Diagram of the available inkjet printing technologies [1].

The state-of-the-art about the printing technology and the main characteristics of each technique are discussed as follows.

1.1 Continuous Ink Jet printing techniques

Continuous inkjet (CIJ) designs are mainly used in high volume applications, such as industrial coding, marking and labelling markets. As the name suggests, the operation of CIJ requires a continuous generation of ink stream from a pressurized fluid reservoir.

1.1.1 Binary Continuous Inkjet

In a Binary Deflection system, the ink drops are either uncharged or charged by an electrode after leaving the nozzle. The electrode controls the printing in the following way: only uncharged drops reaches the substrate while the charged drops are deflected by an electrical field in to a gutter for recirculation (Figure 1.2).

The working principle of this technique is schematically shown in Figure 1.2.

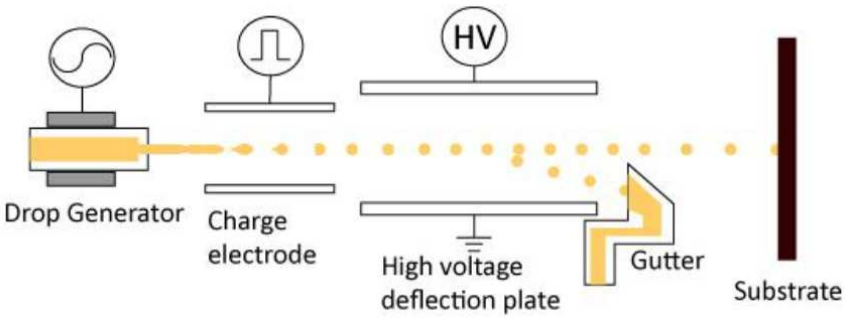

Figure 1.2 Schematic illustration of a binary-deflection continuous inkjet system [1].

1.1.2 Multiple Deflection System

In the Multi-Deflection technique, the inkjet printed drops receive different charge, so that as they pass through electric field they are deflected more or less in different directions. In this way, it is possible to print the droplets in different positions even if

the substrate and the printhead are static. The working of this system is schematically illustrated in Figure 1.3.

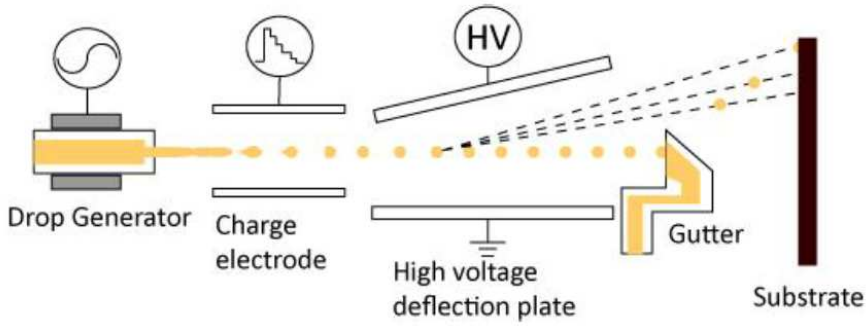

Figure 1.3 Schematic illustration of a multiple-deflection continuous inkjet [1].

1.1.3 Hertz Continuous Inkjet

In 1966, Hertz et al. proposed a method for achieving variable density of printed spots in continuous inkjet printing using the electrostatic dispersion of a charged drop stream to modulate the number of drops which pass through a small aperture. In this method, the amount of ink deposited per pixel is variable. This is achieved by generating very small drops at the speed of about 40 m/s with excitation frequencies of over 1 MHz. The drops uncharged are collected by the gutter (Figure 1.4). The printing drops are less charged to prevent merging in flight.

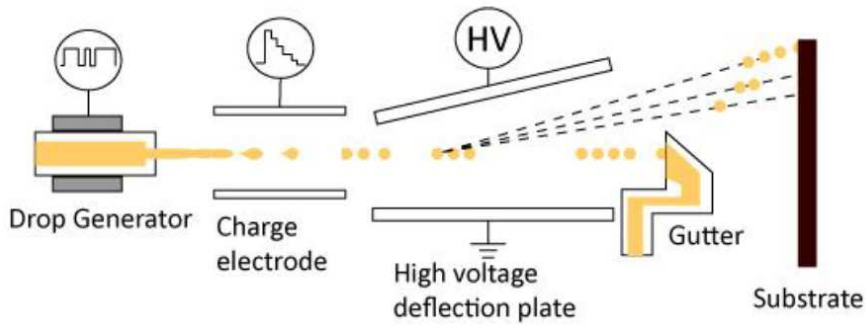

Figure 1.4 Schematic illustration of Hertz continuous inkjet [1].

1.2 Drop on Demand Inkjet printing techniques

Drop on Demand inkjet technology is used in the majority of printers. The smaller drop size and the higher positioning accuracy of DOD inkjet printers are their key advantages for the direct printing of the inks. This approach eliminates the complexity of drop charging and deflection hardware as well as the inherent unreliability of ink recirculation systems required for continuous inkjet technology.

The available DOD techniques can be classified in five main types: Thermal, Piezoelectric, Electrostatic, Focused Acoustic and Piezo-Acoustic DOD inkjet printers.

1.2.1 Thermal Inkjet printing

Thermal Inkjet is considered as the most common inkjet technique and it dominates the market for home users. In this technique, the ink drops are ejected from a nozzle by the growth and collapse of a vapour bubble on the top surface of a small heater located near the nozzle. With a current pulse of less than a few microseconds through the heater, the ink's temperature rises to the critical value for bubble nucleation. When the nucleation occurs, a vapour bubble expands rapidly to force the ink to form a drop outside the nozzle. The whole process of bubble formation and collapse takes place in less than 10 μs. The ink then refills back into the chamber and the process is ready to restart.

This process is schematically illustrated in Figure 1.5.

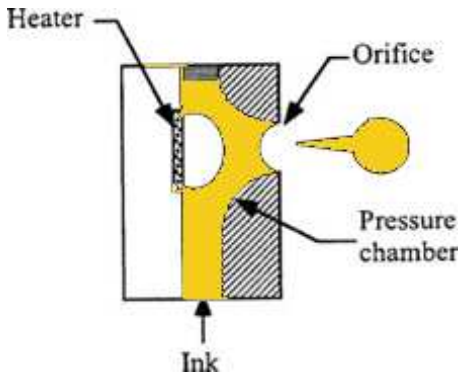

Figure 1.5 Schematic illustration of a thermal inkjet [1].

As shown in Figure 1.6, there are two designs that are usually employed in fabricating thermal inkjet printheads based on where the heating element is located: the roof-shooter design and the edge-shooter design. In a roof shooter design, the heating element is located on top of the nozzle plate parallel to the nozzle orifice, whereas, in an edge shooter design, the heating element is on the side of the fluid chamber perpendicular to the nozzle orifice.

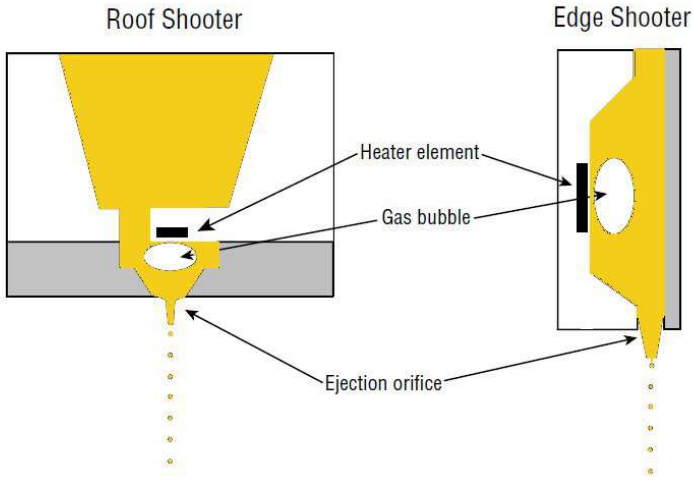

Figure 1.6 Schematic illustration of a roof-shooter design (left) and edge-shooter design (right) of a thermal inkjet device [1].

1.2.2 Piezoelectric Inkjet printing

In a piezoelectric inkjet device, a piezoelectric material is used instead of a heating element to produce the force necessary to eject a droplet. Piezoelectric materials deform when a voltage is applied onto them. In an inkjet head, this deformation can be used to displace volume in a fluid chamber for droplet ejection. Unlike thermal inkjet, the process is purely mechanical and therefore does not present degradation problem of the inks.

Piezoelectric inkjet operation can be categorized into four types, based on the piezoelectric deformation mode: squeeze, shear, push and bend mode.

In squeeze mode (Figure 1.7a), the piezoelectric crystal surrounds a glass capillary-nozzle system. Applying a short rise-time voltage pulse the piezoelectric crystal contracts and “squeezes” the liquid which causes a small amount of liquid to be expelled from the orifice.

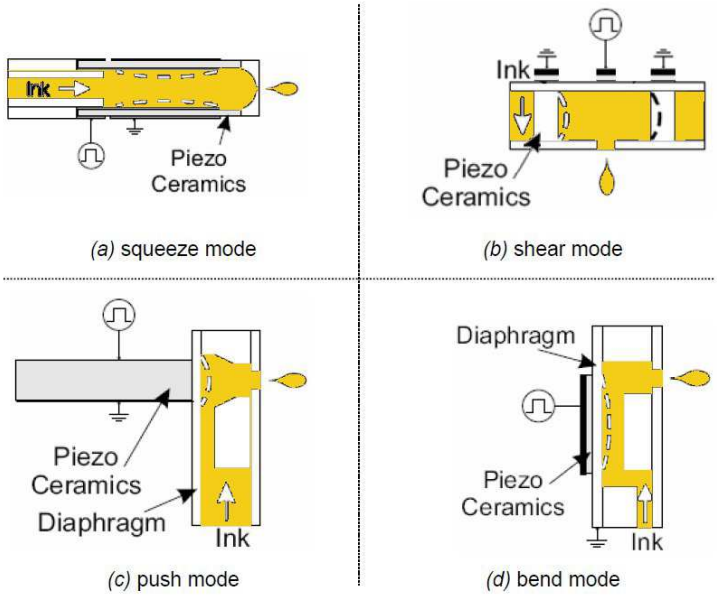

Figure 1.7 Schematic illustration of (a) squeeze mode, (b) shear mode, (c) push mode and (d) bend mode of a piezoelectric inkjet printing [1].

In shear mode (Figure 1.7b), the applied voltage is perpendicular to the polarization of the piezoelectric material. The shear mode design deforms the piezoelectric against ink to eject the droplets. In this case the piezo becomes an active wall in the ink chamber. Interaction between ink and piezoelectric material is one of the key parameters of a shear mode printhead design.

In both push mode (Figure 1.7c) and bend mode (Figure 1.7d), the applied voltage is parallel to the polarization of the piezoelectric material.

In the push mode a piezoelectric rod is used to push out the ink. In practice a thin membrane is placed between the rod and the ink to prevent undesirable interaction.

The bend mode inkjet has piezoceramic plates which are bonded to a diaphragm forming an array of bilaminar electromechanical transducers used to eject the ink drops. By applying a voltage to the piezoelectric plate, the plate is contracted, causing the diaphragm to flex into the pressure chamber. The diaphragm motion pressurizes the printing liquid in the chamber and forces a drop to be expelled from the nozzle. The size of the drops is controlled by the voltage applied to the deflection plate, the pulse duration and the nozzle diameter.

1.2.3 Electrostatic Inkjet Printing

The basic principle of Electrostatic inkjet is to generate an electric field between the ink chamber and the substrate. Contrary to the other techniques mentioned above, where the ink drop is formed and ejected by pressure, the ink drop in electrostatic inkjet is emitted using the electric field. There are several methods for doing this, e.g. using the Taylor Effect or by using thermal effect to change viscosity as controlling mechanism. Some of these methods are very advanced and has proven to be able to produce very small drops [3].

1.2.4 Focused Acoustic Inkjet Printing

In the Focused Acoustic Inkjet Printing, an acoustic wave is focused onto a fluid surface to eject droplets from the liquid. A piezoelectric transducer is attached to one end of a solid rod. On the other end of the rod, an acoustic lens focuses the acoustic waves given out by an RF generator (Figure 1.8).

This technique has the advantage of being potentially unaffected to clogging because the ejection aperture is a large region of a fluid surface defined by the diameter of the focal spot. Another advantage is the possibility to vary the size of the ejected drops shifting the distance between the fluid and the transducer in order to vary the focal spot diameter on the surface of the fluid.

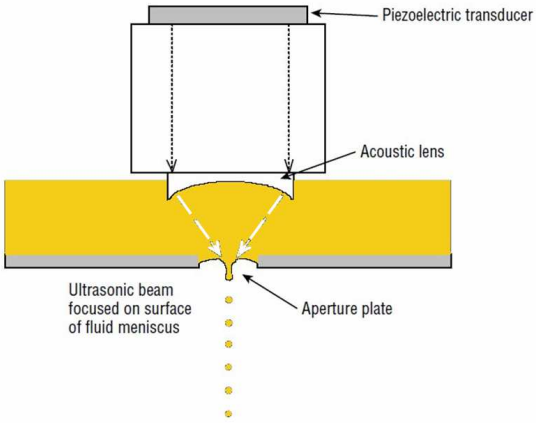

Figure 1.8 Schematic illustration of a Focused Acoustic Inkjet printer.

1.2.5 Piezo-Acoustic Inkjet Printing

In scientific research the piezo-acoustic DoD inkjet system is mainly used, because of its ability to dispense a wide variety of solvents and functional materials such as conductive polymers and nanoparticles [4–6], sol-gel materials [7], cells [8], and structural polymers [9].

In a Piezo-Acoustic inkjet printing technique, when a voltage pulse is applied, the piezoelectric actuator contracts and creates a pressure wave which propagates through the capillary tube into the liquid. In the nozzle region the pressure wave accelerates the liquid forming a droplet, if its kinetic energy is sufficient to overcome the surface energies and the viscous dissipation.

In this thesis work, piezo-acoustic inkjet printheads produced by MicroDrop Technologies (MD-K-130 and AD-K-501 specifically) were used. These inkjet printers are based on apart of the squeeze-mode inkjet printers described in the previous section. In particular, the choice of this kind of technique is based on the necessity to print liquids without heating the fluid which can cause the degradation of the material properties.

The core of the Microdrop dispensing head (Figure 1.9a) consists of a glass capillary (opening nozzle 20-100 µm) which is surrounded by a tubular piezo actuator. The droplet volumes in flight are in the range of 20-500 pl corresponding to nozzle diameters of 20-100 µm.

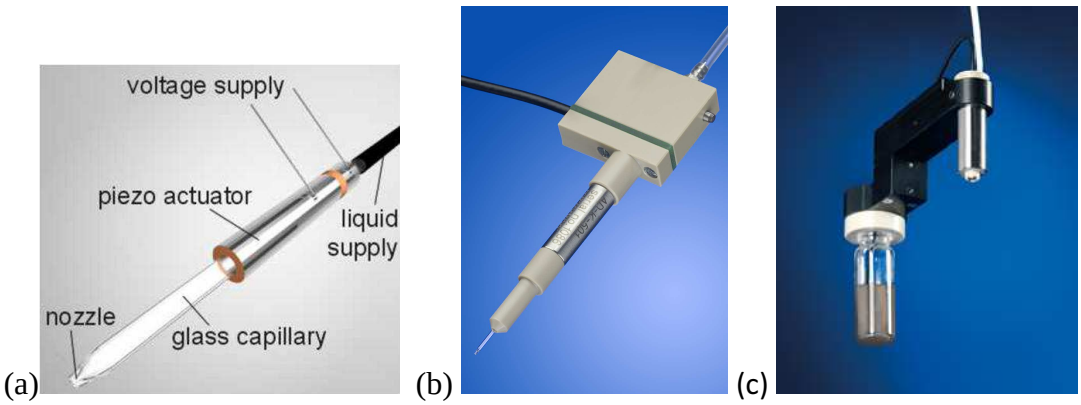

Figure 1.9 (a) Schematic illustration of a Microdrop piezo-acoustic inkjet printhead (b) picture of a AD-K-501 pipette; (c) picture of a MD-K-130 printhead with holder and reservoir.

Depending on the configuration, the system can be equipped with the pipette (Figure 1.9b) or the dispenser head (Figure 1.9c) system. In the first case, the fluid is directly aspirated through the nozzle tip into the glass capillary, while in the second case the material is stored in a reservoir connected with the printhead. The pipettes allow to print of all kinds of solvents and materials that could be incompatible with the silicon material that surrounds the printhead.

A rectangular voltage signal is sent to the piezoelectric actuator for the drop generation. Various signal parameters, like the pulse amplitude [30-255 V], the pulse length [8-255 μs] and the frequency [1-12500 Hz], can be adjusted in order to optimize the drop emission.

The printing system is equipped with a CCD (charge coupled device) camera and a stroboscopic LED (light emitting diode) placed on opposite side underneath the printer head outlet to visualize drops in flight at different time. Through a visual control, this system allows to determine the optimized piezo-voltage, pulse-duration and frequency parameters to provide a reliable droplet ejection and to avoid the satellite drops.

The entire vision system of the inkjet printing equipment used in this thesis work includes other two units in addition to the above mentioned drop vision system: a camera-assisted printing process system and a camera-assisted alignment system. The camera-assisted printing process is a horizontal camera that allows to follow the printhead during the printing process. The camera-assisted alignment system is a vertically installed camera equipped with a microscope. It allows the visualization of the drop impact point enabling, in particular, perfect alignment of the printed drops with pre-structures.

The inkjet head controller generates a high-voltage signal to actuate the piezoelectric inkjet printer head. In addition, this unit provides a pressure control system to regulate the pressure inside the reservoir and to supply the liquid in the reservoir to the glass capillary. A negative pressure respect to the ink outlet, in the range of mbar, must be applied for pump the liquid into the capillary and obtain stable drop emission. The same unit can be used to fill or empty the printer head for cleaning purposes.

The provided user interface allows the adjustment of the printing control parameters, namely the pulse amplitude, its duration and frequency.

The high precision motorized stage enables the positioning of the printhead on substrates with micron range accuracy and with high speed (range 0.1-500mm/s; standard working condition 1-5mm/s).

A CAD software is used to design the geometry of the printing material on the substrate.

The inkjet equipment used in this thesis work has been designed by Aurel S.p.A. for printing inks on both rigid and flexible substrates, in the form of reel or single sheet. The inkjet printer located at the ENEA Research Centre of Portici is shown in Figure 1.10.

Figure 1.10 Image of the inkjet printing equipment at ENEA Portici.

1.3 Fluid dynamic principles

In the inkjet printing technique, the liquid in the glass capillary must fit the physical and rheological requirements of fluid flow, in terms of viscosity and surface tension in order to be successfully ejected. For a fixed geometry and initial fluid characteristics, the analysis of the fluid mechanics problem in a dimensionless form is beneficial due to the reduction of the number of governing parameters. In order to quantify and compare liquid properties, both in-flight and upon impacting the substrate, the dimensionless Reynolds and Weber numbers can be introduced. The

Reynolds number (Re) highlights the importance of the inertia/kinematic forces with respect to the viscous resistance forces in a flow and it is defined as the ratio of the inertial forces versus the viscous stress within the droplet:

$$\mathrm{Re} = \frac{\rho d \upsilon}{\eta} \qquad \text{(eq.1.1)}$$

where ρ is the fluid density, d the nozzle diameter, v the velocity and η the viscosity of the in-flight droplet.

Another condition to be satisfied is that the kinetic energy must be higher than the surface tension of the drop. This is correlated with a dimensionless number, called Weber number [10], which represents the ratio of inertial forces versus the interfacial stress:

$$We = \frac{\rho d \upsilon^2}{\gamma} \qquad \text{(eq.1.2)}$$

where γ is the surface tension of the liquid.

Both dimensionless numbers have a large influence on the droplet impact and spreading [11–13]. Typically, for inkjet printing experiments, both the Reynolds and Weber numbers are relatively low and in the order of 1 – 100, since the velocity and the size of the droplets are relatively small. This properties controls and usually prevents splashing of the droplets upon impacting the surface.

Fromm's dimensionless *Z*-number is a particular combination of these two dimensionless numbers and it is related to the propagation of the pressure wave and its attenuation by viscous dissipation [14]:

$$Z = \frac{\sqrt{\rho d \gamma}}{\eta} = \frac{\mathrm{Re}}{\sqrt{We}} \qquad \text{(eq.1.3)}$$

As predicted by Fromm, the drop formation in DoD systems is only possible for $Z>2$. Later, Derby *et al.* [15] refined this prediction to $1 < Z < 10$, but this theoretical condition seems to be valid only for concentrated wax or paraffin suspensions. In practice, however, the lower limit is determined by the viscosity that dissipates the pressure pulse, whereas the upper limit is correlated to the formation of satellite

droplets [16]. It is important to classify satellites and satellite-drops. Satellite-drops are undesired drops generated besides the main drop. In a DOD inkjet printer, satellite-drops are usually generated when the kinetic energy is too high, so the ejected liquid column breaks up into more than one drop. In some cases satellite-drops have the same trajectory as the main drop and may collapse with it if their velocity is higher than the speed of the main drop. On the contrary, the trajectory of satellites is not well controlled.

1.4 Ink formulation

A crucial element for the inkjet printing technology is the ink formulation. The first and foremost consideration is the compatibility of the fluid with the materials of the printhead component parts. If the fluid chemically reacts with the elements of the printhead, the use of the pipette, where only the glass capillary goes in contact with the ink, is needed.

Moreover, specifically for DOD piezoelectric inkjet technique, the chemico-physical properties of the fluid that can be ejected by this printing system have very narrow variability ranges. This depends on the usually quite weak mechanical force generated by the piezoelectric crystal deformation on the fluid. As a result, the typical fluid must has sufficiently low viscosity to allow the ejection. By assuming that all the used fluids exhibit Newtonian properties, the viscosity μ is simply described as:

$$\mu = \frac{\tau}{\dot{\gamma}} \qquad \text{(eq.1.4)}$$

where τ is the shear stress, that is the required force per unit area to produce the fluid flow, and $\dot{\gamma}$ is the shear rate, that is the differential velocity of the fluid flow.

For the Microdrop printhead, the ideal fluid viscosity range is 0.5-40 cP. If the fluid viscosity exceeds this values, the fluid could not be ejected by the piezo actuation. On the other hand, if the fluid viscosity is too low, the fluid can be idle in or drip from the nozzle resulting, in this last case, in poor jetting quality with the

presence of filaments or satellites. The ink viscosity is usually adjustable by modifying the solvent or the material concentration in the fluid.

Although low viscous fluid are desirable for jetting purposes, the high viscosity guarantee the reduced droplet spreading when the fluid lands on the substrate. The control of this parameter is critical since the droplet condition strongly influences the film uniformity. The viscosity range for the printhead employed in this thesis work is around 20-70 mN/m.

Another important factor in the viability of ink ejection is the size of the particles in the fluid. Usually, particle diameter smaller than 1 μm in diameter is the right dimension desirable for eject nanodispersion when using DOD piezoelectric inkjet printhead. Moreover, the time-stability of the suspension is also a crucial parameter for the printability of the fluid because the particles in suspension should not agglomerate for all the time of the printing process.

In addition to the viscosity and time-stability properties, the surface tension is another important fluid characteristic that must be considered. In general, high surface tensions don't allow the fluid separation in forming single drops. On the other hands, high surface tensions prevent the droplet spread on the substrate so promoting a spherical shape of the dried printed droplet.

On the contrary, if the surface tension is too low, it is difficult to generate stable droplets and the fluid element emerging from the needle could show long continuous tails along the flight path. Moreover, from the wetting perspective, is undesirable to have very low surface tension because of the wider spreading on the target substrate that makes difficult the realization of a well defined structure.

Therefore, a good ejecting quality is usually characterised by:

- no wetting of nozzle plate during ejection,
- compatibility with the printhead and the delivery system,
- small ejecting drop volume variation among the generated droplets,
- uniform droplet velocity from droplet to droplet,
- absence of satellite droplets,
- straight droplet trajectory along the nozzle/substrate direction,
- long term ejecting stability, including during the on/off cycles.

The optimization of the drop quality is performed through a vision unit consisting of a stroboscopic system focused on the nozzle plate allowing the observation of drops in flight at different phases of generation. Some examples of images from stroboscopic camera showing various ejecting quality conditions are shown in Figure 1.11.

(a) 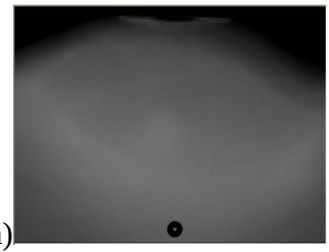 (b)  (c) 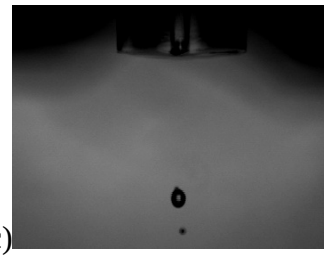

Figure 1.11 Drop images of a stable condition (a), formation of filament (b) and formation of satellite droplet (c).

1.5 Ink-substrate system

The non-contact nature of inkjet deposition makes it a very versatile process being applicable to a wide range of substrates. The interaction between the deposited fluid and the substrate surface is a crucial factor to optimize the deposition process. Another critical aspect of the inkjet printing technique for the quality of the printed material is related to drop drying process which is basically controlled by the so-known “coffee-stain” effect. During the process of solvent evaporation, a capillary flow takes place inside the sessile drop from its centre towards the edges, where the evaporation rate is higher, replenishing the evaporation losses. As consequence, at the end of the drying process the material results largely localized at the rim of the printed droplet. Possible approaches to reduce the ‘coffee-stain’ effect are based on the use of surface treatments (O_2, CF_4, silane, etc.) and mixtures of solvents with different boiling points and surface tensions (“Marangoni effect”) in order to modify the surface energy of the substrate and the surface tension of the liquid, respectively. In the following sections, more details on the wetting properties of the substrates and on the coffee-stain and Marangoni effects are provided.

1.5.1 Wetting of the substrate

In the printing processes, the main ruling factor in the spreading of the fluid droplet on the substrate is the surface tension (γ) of components. In general, the molecules in a fluid are subjected to the attraction of the surrounding molecules. Inside the fluid, the resultant of all the attraction forces is zero, while on the surface these forces are directed inwards. This effect of "compression" represents the tendency of every system to reach the minimum energy state. The increased surface of a liquid corresponds to an increased energy and, in this case, the equilibrium is reached when the liquid assume the minimum possible size (spherical shape).

The surface tension is defined as the energy to increase the surface area of a unit. Therefore, it quantifies the disruption of intermolecular bonds that occurs when a surface is created and its unit of measurement is energy for unit of area.

The wetting, which is the ability of a liquid to maintain contact with a solid surface, is determined not only by the liquid surface tension, but even by the surface energy of the solid and by the balance between adhesive (between molecules in the liquid and solid) and cohesive forces (between the molecules in the liquid) at the interface (interfacial tension). Greater adhesive force induces lower interfacial tension.

In the fluid-substrate interaction, it is more useful to treat the surface tensions as a system which consists of liquid, solid and vapour interfaces. This approach takes into account that, when a droplet forms on a surface, three interface tensions generate at the solid-vapour interface (γ_{sv}), solid-liquid interface (γ_{sl}) and liquid-vapour interface (γ_{lv}). The base of this concept is schematically illustrated in Figure 1.12.

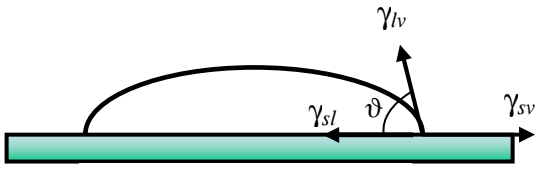

Figure 1.12 Schema of droplet wetting on a solid surface.

The contact angle θ is determined by a balance of the surface tensions at the interface in agreement with Young's equation [17]:

$$\gamma_{sv} = \gamma_{sl} + \gamma_{lv} \cos\theta \qquad \text{(eq.1.5)}$$

For contact angles smaller than 90° the wetting of the surface is strongly favourable and the fluid spreads over a large area of the surface. For contact angles greater than 90° the wetting of the surface is unfavourable and the fluid minimize the contact with the surface and forms a compact liquid droplet.

In order to modify the wetting, different surface treatments are applied. Typically, plasma and silane treatments are the commonly used processes to modify the surface energy of the substrate.

Concerning the plasma treatments, oxygen or fluorine gas are the most commonly employed reactive species. A plasma is composed of a partially ionized gas containing equal volume density of positive and negative charges (ions and electrons, respectively), and a different volume density of atoms in the ground state and excited-state. Inelastic collisions among electrons and gas molecules give rise to reactive species (excited atoms, free radicals, ions and electrons). Thus, the energy gain from the electric field is used to create highly reactive species without significantly raising the temperature. This process is performed under vacuum in order to create a plasma. The plasma treatment can be used for:

- inducing activation through the introduction of surface functional groups containing oxygen,
- etching in CF_4 / O_2,
- organic film deposition (plasma polymerization) or inorganic (SiO_2, Si_3N_4, etc.) one.

The electric field for generating the plasma can be modified by the working frequency (DC, AC, RF, MW), the configuration of the electrodes, inductive or capacitive coupling depending on the applications.

Silanes are chemical compounds consisting of a chain of Silicon atoms covalently bonded to each other and to hydrogen atoms. Their general formula is Si_nH_{2n+2} resulting analogue to the alkane hydrocarbon, where Silicon is replaced by Carbon

atoms. The silane treatment makes a surface hydrophobic by means of its organic substitution.

1.5.2 "Coffee-ring" effect

One of the crucial feature of the printing process is correlated to the droplet drying process that basically induces a final printed droplet which is characterized by the presence of high ridges at drop edge. This effect, called "coffee-stain effect", was first explained by Deegan et al. in 1997 [18]. This phenomenon describes the propensity of the solute to flow out towards the droplet edge through a capillary flow during drying. This occurs owing to the maximum of the evaporation rate and to the drop pinning at the three-phase contact line [18–21].

During the evaporation of solvents incorporated in a printed droplet, while solvent molecules evaporating at the center of the droplet are readily reabsorbed, solvent molecules from the edge can easily escape without any reabsorbing process. This phenomenon results in a larger evaporation rate around the edge. Such a fast evaporation at the contact line induces an outward diffusive flow to compensate for the liquid removed by evaporation and, in turn, transports the suspending solute to the edge region [22,23].

This effect is represented in figure 1.13.

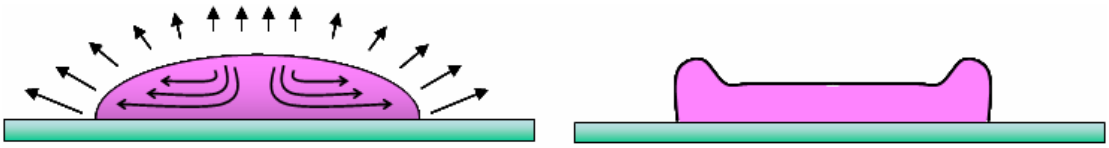

Figure 1.13 Illustration of "coffee-stain" effect. Evaporation rate (represented by upward arrows) is highest at the edges of a printed droplet resulting in an accumulation of the solute at the periphery at the end of the drying process.

For this reason, the coffee-stain effect causes a poor uniform distribution of the printed material which, in general, degrades the final device working.

1.5.3 Marangoni effect

A possible strategy to reduce the "coffee-stain" effect is based on the employment of mixtures of solvents with different boiling points and surface tensions. By mixing appropriately two solvents with different chemico-physical properties (surface tension, boiling point) along the sessile drop radius a concentration gradient of one solvent is generated opposite to the concentration gradient of the other solvent. The concentration gradients induce opposite solute capillary flows along the drop radius profile producing a distribution of the printed material whose final profile depends on the volume mixing ratio of the solvents suitably combined with their volatility and surface tension properties. This happens because the droplet drying process is controlled by Marangoni effect [24,25] in addition to the "coffee-stain effect". The Marangoni flow is related to the temperature gradient of the sessile drop and, hence, to the different surface tension at the droplet liquid-air interface. While the Marangoni effect is less dominant than the diffusive flow in a single-solvent system, the same becomes more significant in the case of dual-solvent system in the definition of the profile of printed droplet. This behaviour is schematically illustrated in Figure 1.14.

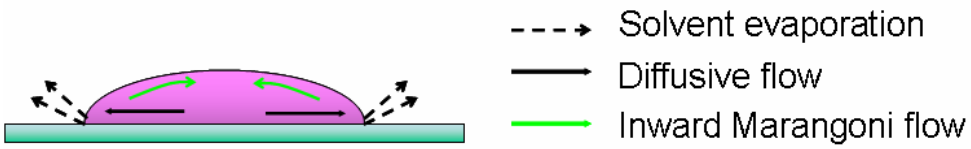

Figure 1.14 Illustration of "Marangoni effect". The diffusive flow ("coffee-stain" effect) is directed from the centre to the edge of the printed droplet. If mixture of high- and low- boiling point solvents is employed an inward Marangoni flow can be generate, inducing a balance of material at the centre of the dried droplet**.**

The physical process responsible of the Marangoni effect is the following. Since the solvent evaporation requires the consumption of latent heat and the thermal conduction path is longer at the top centre of the sessile droplet, the surface temperature is lower at the central region. Since the surface tension is a function of the temperature, the presence of a gradient of the surface tension along a fluid-fluid interface induces a Marangoni flow from regions with low surface tension (the film

edges) to regions with high surface tension (the film centre) [24]. In general, in a single-solvent system, the temperature-gradient-driven Marangoni flow is less important in the evaporating droplet than the convective flow. Conversely, when using a mixture of low- and high boiling-point solvents (dual-solvent system), the solvent composition at the contact line will shift towards more to higher-boiling-point solvent than that in the bulk due to the fast evaporation of the low-boiling-point solvent at the edge, creating a compositional-gradient-driven Marangoni flow [9,26,27]. If the high-boiling-point solvent has a higher surface tension than that of the low-boiling-point solvent, an outward Marangoni flow is induced from the centre to the edge. In the opposite case, where the high-boiling-point solvent has a lower surface tension than that of the low-boiling-point solvent, an inward flow is induced.

Therefore, in a dual-solvent system the Marangoni flow can balance the convective flow assuming a significant role in defining the shape of the printed droplet. In order to realize a uniform layer with a reduced “coffee-stain” effect, both the direction and magnitude of each flow should be well-designed, so an inward flow can be induced or, in the same way, an outward flow can be suppressed.

1.6 Organic electronics

Organic electronics is a branch of electronics dealing with carbon-based materials which are able to carry electric charges. These compounds can be in form of polymers (macro-molecules) or oligomers (small molecules).

The discovery in 1977 of Shirakawa, MacDiarmid and Heeger on the significant electrical conduction of doped polymer materials, such as polyacetylene or polyaniline, exhibited a, promoted a general interest in the study of these materials [28,29].

Nowadays, organic electronics includes organic conductors, semiconductors, dielectrics and light emitters. In general, since organic materials are lighter, more flexible and less expensive than inorganic ones, their use in electronics is making possible the introduction of new applications. In particular, one of the most interesting properties of organic materials resides in their solubility in a wide variety

of solvents, making them printable by low-temperature and low-cost techniques. This specific feature is opening the way to the realization of a broad range of products and represents a considerable boost to the development of the organic ("plastic") electronic technology based on the employment of innovative industrial techniques like inkjet printing.

In the last decades, most organic materials showing electrical conduction have been classified as semiconductors. In particular, semiconducting polymers have increased their potential application in low-cost electronic circuits which can be fabricated on any substrate type, also having with flexibility and/or transparency properties [30]. Semiconductor polymers were applied as active elements in a broad variety of devices including light-emitting diodes, solar cells, sensors, and field-effect transistors (FETs) [31].

Recent researches are focusing also on the possibility to dope polymers with conductive metal nanoparticles, in order to noticeably increase their basic conductivity up to values comparable to those of conventional inorganic metals. This possibility enhances the perspective to fabricate, highly-performing fully-organic electronic devices in the next future.

In the following, after an introduction to the basic mechanisms which rule the charge transport phenomena in organic semiconductors, some specific technological applications, relying on the employment of these materials and which are the subject of the experimental work reported in this thesis, will be discussed.

1.6.1 Charge transport in organic semiconductors

According to the band theory of solids, there are three categories of the materials: conductors, semiconductors and insulators.

The continuum distribution of the energy levels in a solid material is called energy band. The highest energy band that contains electrons is called the 'valence band'. The lowest band in which there are unoccupied states is called 'conduction band'. The energy gap between these two bands is called 'band gap'(E_g) [32].

In insulators, the electrons in the valence band are separated by a large gap (E_g >2eV) from the conduction band. In conductors like metals, instead, the valence band overlaps the conduction band and electrons can easily move in response to an external electrical field due to the presence of accessible energy states. In semiconductors, there is a small gap (E_g ~1-2 eV) between the valence and conduction bands, in such a way that thermal or other energy excitations can bridge the gap (Figure 1.15). Furthermore, in presence of such a small gap, the presence of low percentages of a doping material can drastically increase the conductivity.

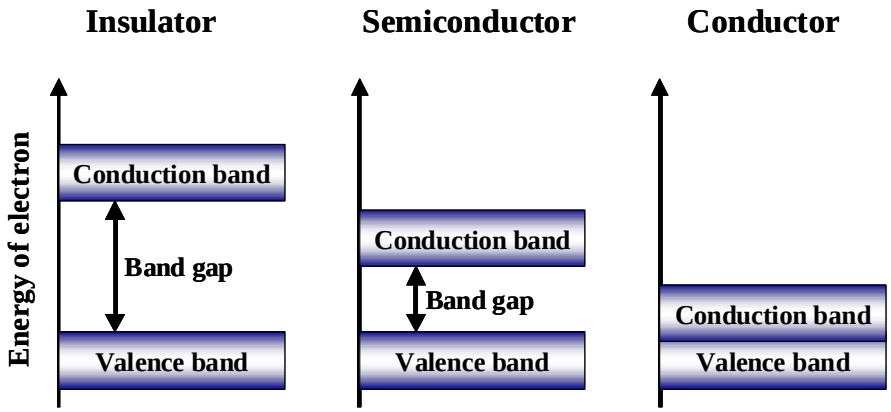

Figure 1.15 Schematic representation of Energy bands for insulators, semiconductors and conductors.

Organic semiconductors, being based on Carbon chemistry, present fundamental differences with the inorganic ones.

The electronic ground state of carbon (atomic number = 6) is $1s^2\ 2s^2\ 2p^2$ as schematically reported in Figure 1.16.

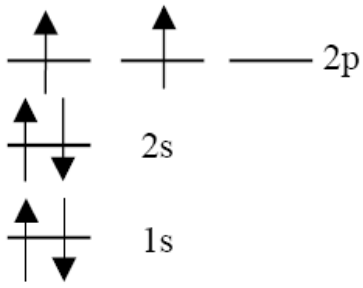

Figure 1.16 Electronic structure of carbon in its ground state.

Carbon, is one of the most versatile elements on the periodic table in terms of the number of compounds it may form. From the ground state electron configuration, the carbon has four valence electrons, two in the 2s shell and two in the 2p shell. This minimum energy condition requires the saturation of bonds which can occur in three different configurations.

In the first configuration, carbon will form an excited state by promoting one of its 2s electrons into its empty 2p orbital and hybridize. By forming this excited state, carbon will be able to form four bonds with other atoms. The excited state configuration is shown in Figure 1.7 and is called sp^3 hybridization.

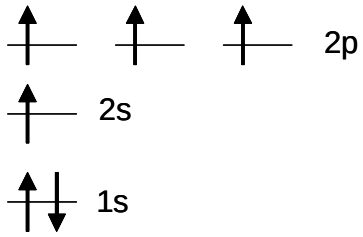

Figure 1.17 Electronic structure of the sp^3 hybridization.

The second carbon configuration is the sp hybridization (Figure 1.18). In it the s orbital and one of the p orbitals from carbon's second energy level are combined together to make two hybrid orbitals. Those hybrid orbitals arrange themselves in three dimensional space to get as far apart as possible. They are exactly opposite one another from the center of the carbon atom. Because this type of sp hybridization only uses one of the p orbitals, there are still two p orbitals which the carbon can use. This kind of hybridization occurs when a carbon atom is bonded to two other atoms.

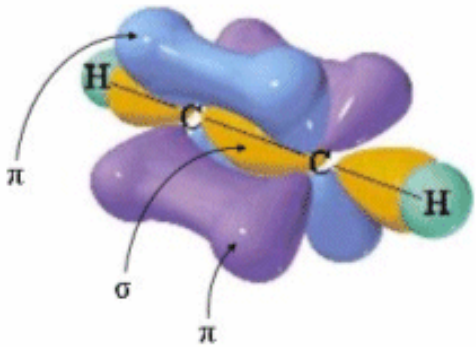

Figure 1.18 Molecular orbitals of sp hybridization.

The last configuration is the sp^2 hybridization, where three of the valence electrons form the so-called sp^2-hybridized orbitals, which are at an angle of 120° with each other and stay on the plane (xy). The fourth electron, instead, resides in a so-called p_z orbital which is orthogonal to the xy plane (Figure 1.19a).

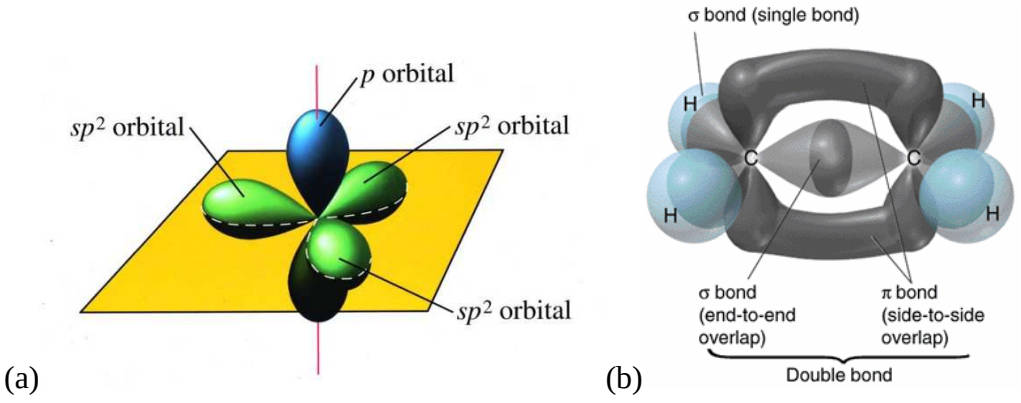

Figure 1.19 (a) sp^2-hybridized orbital of a carbon atom; (b) molecular orbitals of two double bonded carbon atom forming π bonds and σ bonds.

Two of the sp^2-hybridized orbitals form σ-type single bonds with two adjacent atoms. The remaining sp^2 hybridized orbital and the p_z orbital form a σ bond and a π-bond with another carbon atom. (Figure 1.19b). Hence, systems of interacting p_z orbitals are called 'π-conjugated' systems and characterize the semiconductor polymer structure. The sp^2 configuration is associated with a highly localized electron density in the plane of the molecule which is the backbone of the conduction mechanism in the organic semiconductor. The overlap of p_z electrons provide conjugated polymers with desirable electronic properties allowing the transport of charges.

There are two major classes of organic semiconductors: low molecular weight materials and polymers. An important difference between the two classes of materials lies in the way how they are processed to form thin films. Whereas the small molecules are usually deposited from the gas phase by sublimation or evaporation, the conjugated polymers can only be processed from solution like by spin-coating or printing techniques.

In general, the mechanisms ruling the charge transport in organic semiconductors are basically different from those operating in the conventional inorganic materials.

For the small molecules, due to the weak van der Waals bonding, many electronic properties of these materials, like the energy gap between the highest occupied and lowest unoccupied molecular orbitals (HOMO and LUMO) are determined by the structure of an isolated molecule [33–35]. The weak intermolecular overlap of electronic orbitals results in narrow electronic bands (a typical bandwidth, $E_g \sim 0.1$ eV, is one order of magnitude smaller than the Silicon one), a low mobility of carriers and strong electron-lattice coupling. Moreover, this weak intermolecular bonding gives consequences also in mechanical and thermodynamic properties inducing a reduced hardness and a lower melting point. Furthermore, in the polymer case the charge transport is somewhat different since the morphology of polymer chains can lead to improved mechanical properties. Nevertheless, the electronic interaction between adjacent chains is usually also quite weak in this class of materials.

Depending on the degree of order, the charge carrier transport mechanism in organic semiconductors can fall between two extreme cases: band or hopping transport [36].

Band transport is typically observed in molecular crystals (small molecules) at not too high temperatures. However, since electronic delocalization is weak the bandwidth is small as compared to inorganic semiconductors (typically few eV at room temperature). Therefore, room temperature mobilities in molecular crystals reach values in the range 1 - 10 cm^2/Vs. As a typical feature of band transport the temperature dependence follows a power law behaviour:

$$\mu \propto T^{-n} \quad \text{with n= 1…3} \qquad \text{(eq. 1.6)}$$

upon going to lower temperature. However, in presence of traps significant deviations from such a behaviour are observed.

In the case of polymeric materials, the transport is characterized by hopping mechanism where the charge carriers, free to move along a polymer, are responsible of the conduction of charge in the polymer films. On the other hand, the disorder in the film together with polymer defects should however stop or reduce the conductivity, if it wasn’t for the assistance from phonons (lattice vibration). This

phonon-assisted conduction is described by Mott's Variable Range Hopping Theory (VRH) [37,38]. Here interchain conduction is carried out by processes where a charge can 'jump' (tunnel) to a nearby site where its energy can be higher, thanks to the help of phonons. The charge can then 'jump' on further to another chain or travel along the present polymer chain. Phonons thus enable charges to travel from one side of a polymer film to the other and at higher temperatures, the more phonons are available to provide electrons with the extra energy, and, hence higher conductivity and mobility are achieved increasing in temperature [39]. The mobilities are much lower then in the single crystal case (around 10^{-3} cm^2/Vs) and are correlated to the temperature and the applied filed (F) as follows:

$$\mu(F,T) \propto e^{-\frac{\Delta E}{kT}} e^{\frac{\beta\sqrt{F}}{kT}} \qquad \text{(eq. 1.7)}$$

The solubility of the conjugated materials allows the development of organic inks which can be processed with different printing methods like inkjet, screen, offset and gravure printing. In particular, the organic materials differ from conventional electronics in terms of structure, operation and functionality, which influence device, circuit design and optimization.

1.7 Organic electronic applications

Currently, the printing technologies and, specifically, the inkjet printing technique are very attractive for several applications of organic electronics. Studying some organic devices fabricated by means IJP allows to understand how the control of the working parameters of this innovative deposition method can differently affect the performances of the devices themselves. The present thesis focuses on the following inkjet printed organic devices: VOC sensors, optical components, OFET and OPV.

1.7.1 Conductive polymer materials for sensing applications

Chemical sensors are devices sensitive to changes in the environment and are able to convert the changes into signals, giving a qualitative or a quantitative feedback.

The increased attention to pollution, health and safety have enhanced the need and desire of monitoring the ambient conditions by means of these devices.

Specifically, for the vapour sensing many types of sensors can be employed [40]. These include metal oxide sensors, optical sensors, electrochemical sensors, acoustic wave sensors, intrinsically conducting polymer chemiresistors and polymer composite chemiresistors. In particular, for this last class of sensors the possibility to mix together two materials having complementary behaviours have attracted much attention for gas sensing applications.

Polymer composite sensors made from composites of conductive carbon black nanoparticles dispersed in thermoplastic polymers have been developed and studied extensively in literature. However, so far, they have been fabricated by using traditional techniques like dip coating or spin casting [40–42].

The possibility of having stable and well dispersed suspensions allows the employment of the inkjet printing as innovative technique for the fabrication of sensor devices. This new typology of deposition method is aimed to industrialize the final products opening new perspectives in application fields like food, fragrances, environmental monitoring, medical diagnostics and chemical processing.

1.7.2 Optical grade polymers for optical structures

In the field of optical applications, the development of optical grade polymer based inks allows the use of the inkjet printing technology for manufacturing optical structures. The patterning capability and the possibility to use a single step process makes this technique interesting for the realization of microlenses and polymer microstructuring useful for different optoelectronic applications.

An increasingly used technique is inkjet etching, where solvent or solvent mixture droplets are deposited on soluble polymer surfaces through an inkjet nozzle [43]. At the end of the drying process, a concave- or convex-shaped surface topology can be generated. The shape of the microstructure is basically controlled by the surface tension properties of the droplet acting at the three-phase contact line. The ability to fabricate small cavities onto solid surfaces is interesting for the development of chemical, electrical or optical microdevices. These structures can be used for the fabrication of micro- and nano-pillars [44], microlenses [45], microholes [46], or for removing interference effects in an optical cavity [47].

The additive deposition of solutions of optical grade polymers allows the realization of optical components, such as refractive microlenses, which can be incorporated in many systems and commercial products. They are used, for example, for focusing in detector arrays, fibre optics and sensors, for illumination in flat panel displays, computers and for imaging in photocopiers and lithography [48].

Refractive microlenses are fabricated with different processes like photolithographic [49,50], electroforming [50], melting process [51] and inkjet printing process [52–54]. In particular, the inkjet printing technique is suitable for producing single lenses and large arrays of high optical property refractive microlenses using a very simple and flexible deposition method.

1.7.3 Organic semiconductor for transistor applications

In the field of the organic electronics, the development of organic semiconductors which are air stable and soluble in common solvents allows the fabrication of organic field effect transistors (OFETs) by printing techniques.

Organic field-effect transistors (OFETs) are 3-terminal devices in which the charge carrier density in the channel between source and drain contacts can be controlled by the applied gate voltage across a thin dielectric (Figure 1.20). In the organic semiconductor the charge transport takes place mainly at the interface between organic semiconductor and a gate dielectric with respect to the bulk.

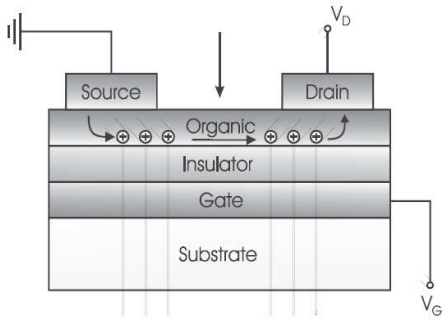

Figure 1.20 Schema of organic field effect transistor.

Recent developments of OFETs are aimed at different applications as organic displays [55], complementary circuits [56] and all-polymer integrated circuits [57].

In particular, the solution processing of organic materials for OFET applications is suited for low-cost fabrication, roll to roll deposition and easy patterning of the electronic structures.

In Figure 1.21 some examples of the most commonly used organic semiconductors (polymers or small molecules) are reported. For both n-type (electron transporting) and p-type (hole transporting) semiconductors it is possible to observe the presence of aromatic rings, corresponding to π-bonds of atoms which are alternately single- and double-bonded to another one.

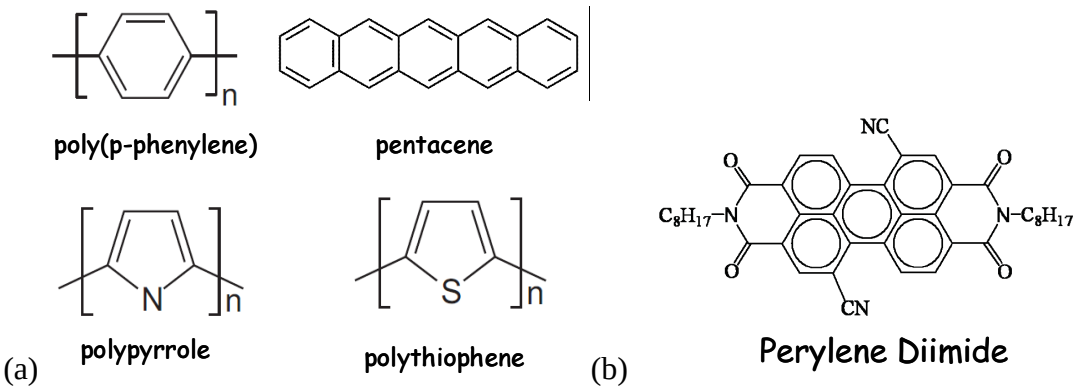

Figure 1.21 Examples of chemical structure of (a) p-type and (b) n-type conjugated polymer semiconductors.

1.6.5 Polymer blend for solar cell applications

An emerging application field of the organic electronics is represented by the organic photovoltaic (OPV), a possible answer to the need of clean and renewable energy.

Despite the expanding use of inorganic semiconductors, the organic semiconductors enable the fabrication of solar modules with several potential advantages, including light-weight, flexibility, low-cost manufacturing and possibility of creating large-area devices. While organic low-molecular-weigh semiconductors are generally deposited by evaporation process, the conjugated polymers are usually deposited from solution by using wet processing techniques like dip-coating, spin-coating, inkjet printing, doctor blading and others. These techniques represent an interesting way for producing OPV cells because they can be performed under ambient conditions (temperature and pressure) and scaled up to large area with minimized loss of material.

At present bulk heterojunction structures, based on blends of polymer donors and highly soluble fullerene-derivative acceptors, are currently the most efficient architecture for polymer solar cells.

Bibliography

[1] Hue P. Le, Progress and Trends in Ink-jet Printing Technology, Journal of Imaging Science and Technology. 42 (1998) 42-62.
[2] Eric R . Lee, Microdrop Generation, 2003.
[3] J.-U. Park, M. Hardy, S.J. Kang, K. Barton, K. Adair, D. kishore Mukhopadhyay, et al., High-resolution electrohydrodynamic jet printing, Nat Mater. 6 (2007) 782-789.
[4] P. Calvert, Inkjet Printing for Materials and Devices, Chemistry of Materials. 13 (2001) 3299-3305.
[5] E. Tekin, H. Wijlaars, E. Holder, D.A.M. Egbe, U.S. Schubert, Film thickness dependency of the emission colors of PPE?PPVs in inkjet printed libraries, J. Mater. Chem. 16 (2006) 4294.
[6] T.H.J. van Osch, J. Perelaer, A.W.M. de Laat, U.S. Schubert, Inkjet Printing of Narrow Conductive Tracks on Untreated Polymeric Substrates, Advanced Materials. 20 (2008) 343-345.
[7] A.M.J. van den Berg, A.W.M. de Laat, P.J. Smith, J. Perelaer, U.S. Schubert, Geometric control of inkjet printed features using a gelating polymer, J. Mater. Chem. 17 (2007) 677.
[8] B. Derby, Bioprinting: inkjet printing proteins and hybrid cell-containing materials and structures, J. Mater. Chem. 18 (2008) 5717.
[9] B.-J. de Gans, U.S. Schubert, Inkjet Printing of Well-Defined Polymer Dots and Arrays, Langmuir. 20 (2004) 7789-7793.
[10] G.O. Thomas, The aerodynamic breakup of ligaments, Atomiz Spr. 13 (2003) 117-129.
[11] J. Fukai, Z. Zhao, D. Poulikakos, C.M. Megaridis, O. Miyatake, Modeling of the deformation of a liquid droplet impinging upon a flat surface, Phys. Fluids A. 5 (1993) 2588.
[12] S. Sikalo, M. Marengo, C. Tropea, E.N. Ganic, Analysis of impact of droplets on horizontal surfaces, Experimental Thermal and Fluid Science. 25 (2002) 503-510.
[13] T. Mao, D.C.S. Kuhn, H. Tran, Spread and rebound of liquid droplets upon impact on flat surfaces, AIChE J. 43 (1997) 2169-2179.
[14] Numerical Calculation of the Fluid Dynamics of Drop-on-Demand Jets, (2001).
[15] N. Reis, C. Ainsley, B. Derby, Ink-jet delivery of particle suspensions by piezoelectric droplet ejectors, J. Appl. Phys. 97 (2005) 094903.
[16] K.A.M. Seerden, N. Reis, J.R.G. Evans, P.S. Grant, J.W. Halloran, B. Derby, Ink Jet Printing of Wax Based Alumina Suspensions, Journal of the American Ceramic Society. 84 (2001) 2514-2520.
[17] P.-G. de Gennes, F. Brochard-Wyart, D. Quere, Capillarity and Wetting Phenomena: Drops, Bubbles, Pearls, Waves, 1st ed., Springer, 2003.
[18] R.D. Deegan, O. Bakajin, T.F. Dupont, G. Huber, S.R. Nagel, T.A. Witten, Capillary flow as the cause of ring stains from dried liquid drops, Nature. 389 (1997) 827-829.

[19] R.D. Deegan, Stress hysteresis as the cause of persistent holes in particulate suspensions, Phys. Rev. E. 81 (2010) 036319.
[20] R.D. Deegan, O. Bakajin, T.F. Dupont, G. Huber, S.R. Nagel, T.A. Witten, Contact line deposits in an evaporating drop, Phys. Rev. E. 62 (2000) 756.
[21] B.-J. de Gans, S. Hoeppener, U.S. Schubert, Polymer relief microstructures by inkjet etching, J. Mater. Chem. 17 (2007) 3045.
[22] T. Kawase, H. Sirringhaus, R.H. Friend, T. Shimoda, Inkjet Printed Via Hole Interconnections and Resistors for All Polymer Transistor Circuits, Advanced Materials. 13 (2001) 1601-1605.
[23] E. Bonaccurso, H.-J. Butt, B. Hankeln, B. Niesenhaus, K. Graf, Fabrication of microvessels and microlenses from polymers by solvent droplets, Appl. Phys. Lett. 86 (2005) 124101.
[24] H. Hu, R.G. Larson, Marangoni Effect Reverses Coffee-Ring Depositions, The Journal of Physical Chemistry B. 110 (2006) 7090-7094.
[25] S. Jeong, D. Kim, J. Moon, Ink-Jet-Printed Organic−Inorganic Hybrid Dielectrics for Organic Thin-Film Transistors, The Journal of Physical Chemistry C. 112 (2008) 5245-5249.
[26] J. Park, J. Moon, Control of Colloidal Particle Deposit Patterns within Picoliter Droplets Ejected by Ink-Jet Printing, Langmuir. 22 (2006) 3506-3513.
[27] P. Takhistov, H.-C. Chang, Complex Stain Morphologies, Industrial & Engineering Chemistry Research. 41 (2002) 6256-6269.
[28] H. Shirakawa, E.J. Louis, A.G. MacDiarmid, C.K. Chiang, A.J. Heeger, Synthesis of electrically conducting organic polymers: halogen derivatives of polyacetylene, (CH)x, Journal of the Chemical Society, Chemical Communications. (1977) 578.
[29] C.K. Chiang, C.R. Fincher, Y.W. Park, A.J. Heeger, H. Shirakawa, E.J. Louis, et al., Electrical Conductivity in Doped Polyacetylene, Phys. Rev. Lett. 39 (1977) 1098.
[30] R. Farchioni, G. Grosso, Organic Electronic Materials: Conjugated Polymers and Low Molecular Weight Organic Solids, 1st ed., Springer, 2001.
[31] H.S. Nalwa, Handbook of Organic Conductive Molecules and Polymers, Conductive Polymers: Transport, Photophysics and Applications (Handbook of Organic Conductive Molecules & Polymers), 1st ed., Wiley, 1997.
[32] P. Chandrasekhar, Conducting Polymers, Fundamentals and Applications: A Practical Approach, 1st ed., Springer, 1999.
[33] E.A. Silinsh, V. Capek, Organic Molecular Crystals: Interacton Localization, and Transport Phenomena, 1st ed., American Institute of Physics, 1997.
[34] M. Pope, C.E. Swenberg, Electronic Processes in Organic Crystals and Polymers, 2nd ed., Oxford University Press, 1999.
[35] K.-C. Kao, Electrical transport in solids: with particular reference to organic semiconductors, 1st ed., Pergamon Press, Oxford;;New York, 1981.
[36] W. Bruetting, Physics of Organic Semiconductors, 1st ed., Wiley-VCH, 2005.
[37] N.F. Mott, On the transition to metallic conduction in semiconductors, Can. J. Phys. 34 (1956) 1356-1368.
[38] E.M. Conwell, Impurity Band Conduction in Germanium and Silicon, Phys. Rev. 103 (1956) 51.

[39] P.W.M. Blom, M.C.J.M. Vissenberg, Charge transport in poly(p-phenylene vinylene) light-emitting diodes, Materials Science and Engineering: R: Reports. 27 (2000) 53-94.
[40] K.J. Albert, N.S. Lewis, C.L. Schauer, G.A. Sotzing, S.E. Stitzel, T.P. Vaid, et al., Cross-reactive chemical sensor arrays, Chem. Rev. 100 (2000) 2595-2626.
[41] B.J. Doleman, R.D. Sanner, E.J. Severin, R.H. Grubbs, N.S. Lewis, Use of compatible polymer blends to fabricate arrays of carbon black-polymer composite vapor detectors., Analytical Chemistry. 70 (1998) 2560-2564.
[42] M.C. Lonergan, E.J. Severin, B.J. Doleman, S.A. Beaber, R.H. Grubbs, N.S. Lewis, Array-Based Vapor Sensing Using Chemically Sensitive, Carbon Black−Polymer Resistors, Chem. Mater. 8 (2011) 2298-2312.
[43] R. Pericet-Camara, E. Bonaccurso, K. Graf, Microstructuring of Polystyrene Surfaces with Nonsolvent Sessile Droplets, ChemPhysChem. 9 (2008) 1738-1746.
[44] C.H. Liu, J.A. Zapien, Y. Yao, X.M. Meng, C.S. Lee, S.S. Fan, et al., High□Density, Ordered Ultraviolet Light-Emitting ZnO Nanowire Arrays, Advanced Materials. 15 (2003) 838-841.
[45] S. Karabasheva, S. Baluschev, K. Graf, Microstructures on soluble polymer surfaces via drop deposition of solvent mixtures, Applied Physics Letters. 89 (2006) 031110.
[46] T. Kawase, H. Sirringhaus, R.H. Friend, T. Shimoda, Inkjet Printed Via Hole Interconnections and Resistors for All Polymer Transistor Circuits, Advanced Materials. 13 (2001) 1601-1605.
[47] F. Villani, I.A. Grimaldi, G. Nenna, A.D.G. Del Mauro, F. Loffredo, C. Minarini, Study of the interference effects in an optical cavity for organic light-emitting diode applications, Opt. Lett. 35 (2010) 3333-3335.
[48] N.M. Presby, C.R. Giles, Asymmetric fiber microlenses for efficient coupling to elliptical laser beams, IEEE Photonics Technology Letters. 5 (1993) 184-186.
[49] D. Daly, R.F. Stevens, M.C. Hutley, N. Davies, The manufacture of microlenses by melting photoresist, Measurement Science and Technology. 1 (1990) 759-766.
[50] K.-H. Brenner, M. Kufner, S. Kufner, J. Moisel, A. Moller, S. Sinzinger, et al., Application of three-dimensional micro-optical components formed by lithography, electroforming, and plastic molding, Appl. Opt. 32 (1993) 6464-6469.
[51] Hutley M. C, Optical Techniques for the Generation of Microlens Arrays, (1990).
[52] R. Danzebrink, M.. Aegerter, Deposition of optical microlens arrays by ink-jet processes, Thin Solid Films. 392 (2001) 223-225.
[53] Refractive microlens fabrication by ink-jet process, (S.d.).
[54] R. Danzebrink, M.. Aegerter, Deposition of micropatterned coating using an ink-jet technique, Thin Solid Films. 351 (1999) 115-118.
[55] A. Dodabalapur, Z. Bao, A. Makhija, J.G. Laquindanum, V.R. Raju, Y. Feng, et al., Organic smart pixels, Applied Physics Letters. 73 (1998) 142.

[56] Y.-Y. Lin, A. Dodabalapur, R. Sarpeshkar, Z. Bao, W. Li, K. Baldwin, et al., Organic complementary ring oscillators, Applied Physics Letters. 74 (1999) 2714.

[57] C.J. Drury, C.M.J. Mutsaers, C.M. Hart, M. Matters, D.M. de Leeuw, Low-cost all-polymer integrated circuits, Applied Physics Letters. 73 (1998) 108.

CHAPTER 2
SENSORS

Chemical sensor research represents a rich field of study utilizing a wide array of technologies and materials to accomplish the difficult task of converting sensory information into quantifiable chemical, optical or electrical signals. The need to extract increasing amounts of sensory information from our environment fuels the development of sensors that are easier to manufacture, capable of miniaturization, and more sensitive to vapours that excite greater interest. Recently, polymer nanocomposites, whose two component materials have synergic or complementary behaviours, have attracted much attention in different of device applications, such as gas sensors. The possibility to obtain stable and well dispersed suspensions allows the employment of inkjet printing technique for the realization of the sensor devices in a very cheap way. Moreover, this class of vapour-phase sensors has the advantage of using a non-destructive and non-invasive detection method, suitable for green and food applications.

The present chapter is focused on the fabrication and related characterization of chemical sensors by printing a specific polymer nanocomposite based on polystyrene (PS) polymer and Carbon Black (CB) as conductive filler. A study on the sensing properties of this material to volatile organic compounds (VOCs) and on the influence of the printing parameters and the geometrical patterning on the sensing performances is carried out. Moreover, a study aimed to the optimization of the ink deposition on different flexible and non-flexible substrates is also performed.

2.1 Conductive polymer nanocomposites

In recent years, volatile organic compounds (VOCs) chemical sensors are increasingly relying on the use of polymer nanocomposites (PNCs) as sensing materials. Nanosized conductive inorganic fillers dispersed in insulating polymeric matrices belong to the broader category of the PNCs. The conductivity and mechanical-stability properties of nanoparticles combined with the simple processability of polymers, the low cost of both production and materials, the possibility of easy and cheap manufacture of large area devices and the possibility of varying the polymer composition and, hence, the properties of the organic materials, make the resultant hybrid system attractive in a wide range of polymer-based devices such as light emitting diodes [1-3], photodiodes [4], solar cells [5], magnetic storage materials [6] and gas sensors [7].

Conductive sensing films from composites of conductive Carbon Black (CB) nanoparticles dispersed in thermoplastic polymers have been developed and studied extensively by Lewis [8-11], Ho [12-14] and others [15-18].

2.1.1 Swelling mechanism

The working mechanism of these sensors is based on the properties of absorption of the polymer matrix upon exposure to vapour molecules. This mechanism produces an increase of the polymer matrix volume, also known “swelling process”. The presence of conductive fillers dispersed in the polymer generates the transduction mechanism, based on the change of the electrical conductivity. Indeed, an increase of the polymer volume corresponds to a reduction of the conductive filler volumetric fraction determining a disruption of the conductive paths and a change in electrophysical characteristics of the composite [19-28]. Upon organic vapors exposure this class of sensors undergoes a reversible change in electrical resistance.

The physical mechanism is schematically illustrated in Figure 2.1.

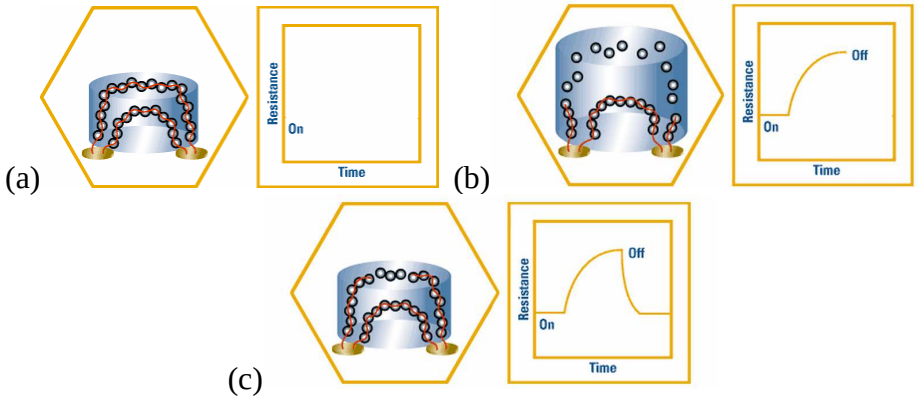

Figure 2.1 Analyte detection: (a) the electrical current flows across the conductive film; (b) the absorption of VOCs into the polymer causes the swelling and the breaking of conductive pathways, so increasing the electrical resistance (c) the analyte is removed and the resistance returns to initial value through a reversible process.

2.2 Geometry role in the sensor performances

Recently, the ink jet printing technology (IJP) was proven to be an useful technique in the deposition of PNCs films up to now prepared by techniques such as spin-coating or drop-casting [29-32], spray [33]. The advantages of the IJP over the aforementioned techniques lie in its potential for printing on both nonflexible and flexible substrates, the efficient use of materials, the reduced waste products, low cost of the process, low processing temperature and its patterning capability. As for this last item, the IJP technology assumes a key role in the feasibility of modifying the sensitive material geometry in controlled and extremely easy manner in order to optimize the sensor response. A deep study of the sensor properties, such as sensitivity, response time and limit of detection, as function of the geometrical configuration and of the printed layer number is useful for the optimization of the gas sensor device performances.

2.2.1 Sensing film: ink formulation and characterizations

The sensing material chosen for the thesis activity is a polystyrene (PS)/carbon black (CB) composite. The atactic polystyrene (Sigma-Aldrich, weight average molecular mass Mw = 25000) was chosen for its sensing property to different organic chemical compounds (acetone, ethanol, toluene, benzene, …). The Carbon

Black (CB), used as conductive filler in preparation of composites, was Carbon Black Pearls 2000 (Cabot Co.). This is a furnace carbon black material with 1500 m^2/g specific surface area, 12 nm average particle size and with 150 g/L density. The PS matrix (80 mg) was dissolved in n-Methyl-2-pyrrolidone (NMP) and the CB nanoparticles (20 mg) were dispersed in the polymeric solution (0.5 wt. %) by means of ultrasonic bath for 90 minutes at room temperature. The PS/CB suspension was finally filtered using a 0.2 μm filter (PTFE) in order to remove bigger agglomerates.

The schematic ink preparation is reported in Figure 2.2.

Figure 2.2 Ink preparation: the polystyrene was dissolved in NMP and the Carbon Black was dispersed in the polymeric solution.

The employed substrates (5x5 mm^2) were made of alumina (Euroacciai S.R.L) with which interdigitated Au electrodes which were previously e-beam evaporated and subjected to a standard lift-off photolithographic process. The interdigitated electrodes are characterized by the following geometrical parameters: the finger length (L_{finger}) is equal to 700 μm, the finger width (W_{finger}) is 100 μm, the gap distance between two adjacent fingers (I_{gap}) is 100 μm and the number of fingers (N_{finger}) is 10. The alumina substrate was chosen for its porous and sliver-shaped surface promoting a good adhesion of the ink on the substrate so assuring a wide sensitive surface.

The functional PS/CB ink was characterized throug Dynamic Laser Scattering (DLS) analysis using a HPPS 3.1 (Malvern Instruments) to determine the average particle size and size distribution of filler in suspension and the dispersion stability in the solutions. Therefore, the inks were characterized by DLS at different aging times. In Figure 2.3 are reported the results of DLS analysis. A typical distribution curve of

the CB particle size in the dispersion presents a peak centered at about 200 nm (Figure 2.3a) and polydispersity index values (PDI) range between 0.12 and 0.18 (Figure 2.3a). These results confirmed the good quality of dispersion process. These parameters resulted roughly constant for an observation time of about 2 years indicating a good time stability for the dispersion (Figure 2.3b). The results of this analysis, combined with the viscosity (2.42 mPa×s) and surface tension (46 mN/m) properties of the suspension, indicated that the dispersion can be employed as ink [34]. Indeed, crucial elements of a dispersion to be dispensed by an inkjet printhead are both the time-stability and the particle size in suspension, which must be less than 1/100 of the nozzle diameter, to prevent clogging and blockage of the nozzle itself and the entire capillary. Therefore, these parameters indicate that the prepared PS/CB suspension can be suitably processed by the inkjet printing system.

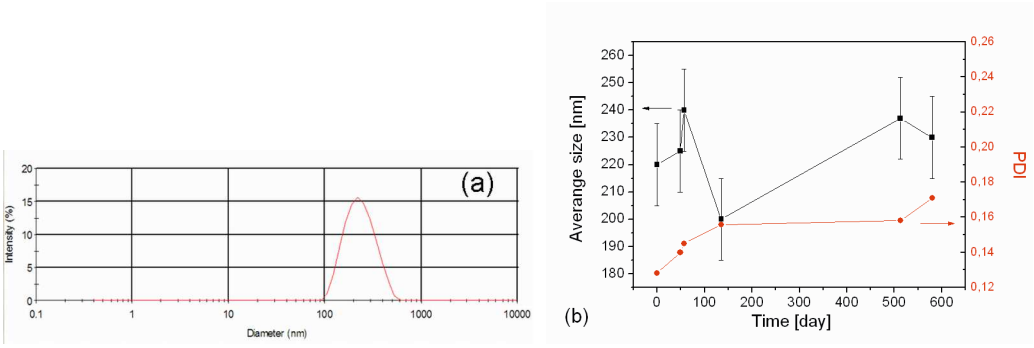

Figure 2.3 (a) Distribution curve of the CB particles size for PS/CB dispersion; (b) nanoparticles average size (square) and PDI (circle) measured in the aging time from 0 to 600 days by DLS analysis.

2.2.2 Sensor device assembly

The processed dispersion was used as ink and printed onto 50 °C heated electrodes/substrate system. The inkjet equipment employed for the device realization was already described in Chapter 1. The Microdrop printhead has a 70 µm opening nozzle corresponding to ~268 pL droplet volume. The driving parameters are the following: pulse width = 75 µs and a driver voltage = 46V. The sensing material geometries consist of one or more lines, created by overlapped droplet sequences (50 % overlap degree, 0.5 Hz drop emission frequency, 0.05 mm/s printhead speed), differently orientated with respect to the transducer fingers.

The layers were deposited by IJ printing the sensing material in five different geometries. Each geometry consists of one or more lines parallel or transverse to the fingers of the interdigitated electrodes; the fifth geometry is a cross. Moreover, two different configurations were fabricated with three- and penta-overlapped layers for each pattern with the aim of investigating the thickness effect on the sensor performances. The optical micrographs (Polyvar MET Reichert-Jung) of the samples with different geometries are shown in Figure 2.4. The gold electrodes are represented by the most bright part of the images.

Before investigating the sensor device working, the morphological analysis of the printed layers was carried out in order to get useful information on the sensor behaviour. In Figure 2.5 the SEM (SEM, LEO 1530) image of a three-layer sample is shown as comparison with the simple substrate used as reference. The printed PS/CB distribution on the alumina substrate (Figure 2.5a) is characterized by wide uncovered areas and by a clearly porous structure of the printed ink which permit a good interaction between the gas and the polymer nanocomposite material. The SEM image of the substrate surface is reported as reference in Figure 2.5b. This analysis showed that multiple layers are necessary to cover the porous structure of the substrate and to obtain a conductive continuous film.

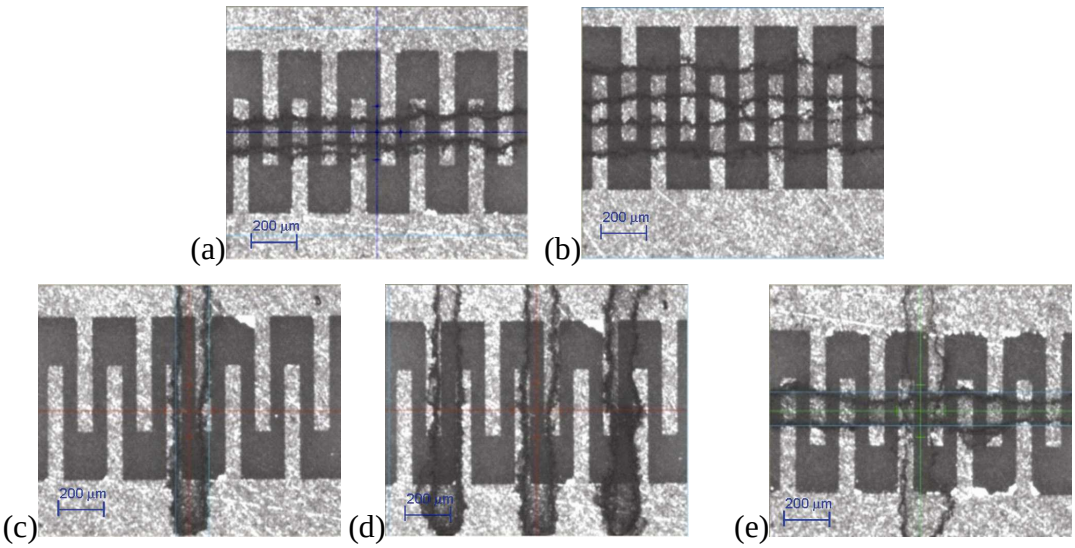

Figure 2.4 Optical micrographs of printed devices with different geometries: (a) transverse single-line, (b) transverse double-lines, (c) parallel single-line, (d) parallel three-lines, (e) cross.

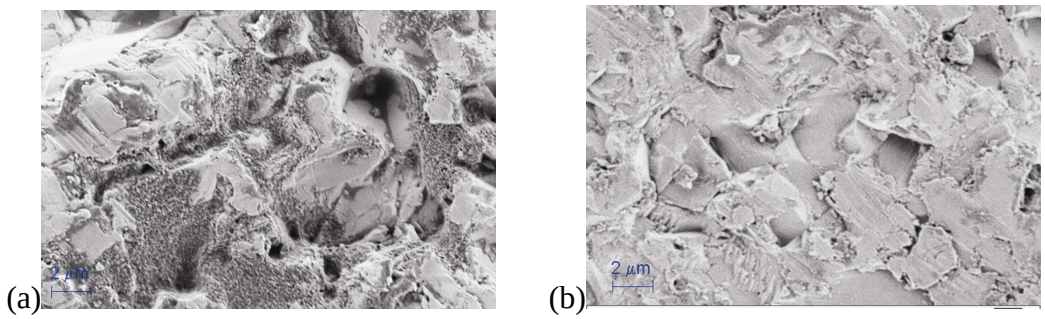

Figure 2.5 SEM images of (a) PS/CB printed on alumina substrate, (b) alumina.

The SEM analysis is further supported by the AFM investigations (Veeco, Dimension Digital Instruments Nanoscope IV) performed on the same samples. In particular, in Figure 2.6 the AFM phase images obtained by scanning 1x1 μm^2 surfaces of a three-layers sample in different zones are reported. The images acquired at the printed line centre are in agreement with the SEM analysis results concerning the non-uniformity of the deposited nanocomposite. Indeed, the printed material distributes differently on the substrate as pointed out by pictures related to three typical configurations characterized by low (Figure 2.6a), partial (Figure 2.6b), and complete (Figure 2.6c) covering of the substrate by the nanocomposite.

However, if on the one hand the high roughness of the alumina substrate (average roughness about 800 nm) and its sliver-shaped structure induce a not uniform distribution of the printed material, on the other hand it assures a good adhesion of the inkjet printed ink.

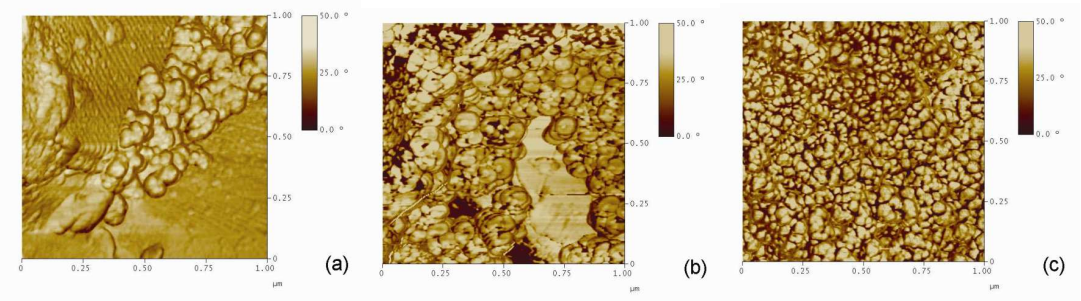

Figure 2.6 AFM phase images of printed PS/CB sample in different zones of the substrate with (a) low (b) partial and (c) complete covering by the nanocomposite.

2.2.3 Electrical characterization under analyte vapours

A volt-amperometric technique, at constant bias, was employed for sensor dc electrical characterization. The sensor response was measured upon exposure to acetone vapours at different concentrations (600, 1250, 2500, and 5000 ppm) in a Gas Sensor Characterization System (Kenosistec equipment) that allows to monitor and control pressure, flow rate, actual gas composition, humidity and environment temperature. The test chamber at ENEA Portici is showed in Figure 2.7.

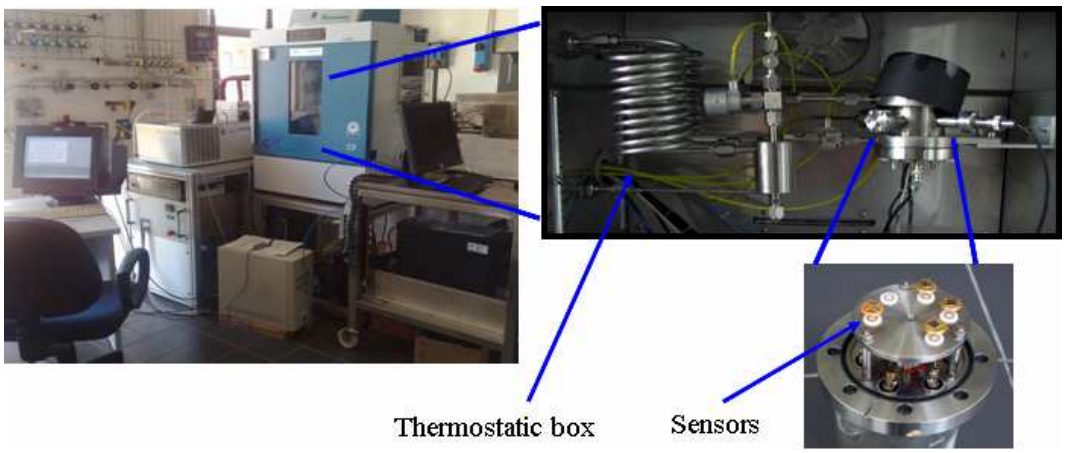

Figure 2.7 Gas sensor characterization system for electrical analysis under different organic vapours.

In such a system the device was placed in a stainless steel test chamber placed in a thermostatic box at controlled temperature (20 °C) and humidity (30%). A constant flow rate (500 cm^3/min) of the gas carrier (nitrogen) crosses the test chamber. The carrier can be properly humidified through a water bubbler placed in a thermostatic bath.

In this environment, characterized by controlled temperature and humidity, the resistance value of the device in its equilibrium state is firstly measured (baseline); after that, an intentional disruption of the equilibrium state is produced by introducing a controlled amount of VOC analyte and by mixing it with the gas carrier for a time step of 3000 s. To validate and monitor the gas mixture, a thermo Antaris IGS FTIR analyzer is placed at the gas output in order to measure the chemical compounds concentration in the test chamber with a resolution of ppm.

Hardware and software, implemented on a work station, allow to control and record environmental parameters, device bias and output signal, making possible to perform customizable automated tests on devices for the measurement of sensor parameters such as sensitivity, response time, noise and limit-of-detection (LoD). In detail, the sensitivity is expressed in terms of the relative differential response $\frac{R-R_O}{R_O}$, where R_O is the sensor baseline resistance and R is the sensor resistance upon exposure to solvent vapours. Moreover, the LoD is defined as the analyte concentration at which a sensor response corresponds to signal-to-noise ratio (S/N) equal to 3, in according with the conventional definition by IUPAC [32]. The response time is defined as the time required for the signal to change from 10 % to 90 %.

The electrical sensor response upon exposure to 600, 1250, 2500, and 5000 ppm of acetone vapours for three-layers and penta-layers devices are reported in Figure 2.8a and Figure 2.8b, respectively.

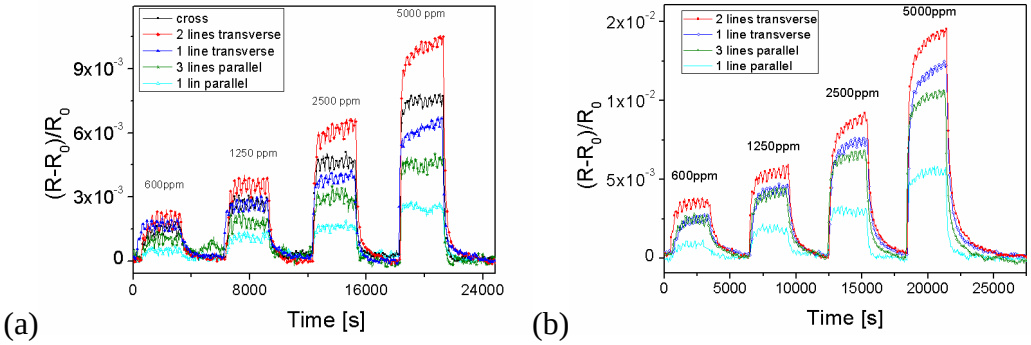

(a) (b)

Figure 2.8 (a) Three-layers and (b) penta-layers sensors electrical responses to acetone vapours.

The parameters that characterized the three-layers sensor performances are summarized in

Table 2.1, while the ones for the penta-layers are reported in Table 2.2.

Morphology	Resistance [KOhm]	Sensitivity [1/ppm]	Limit-of-Detection [ppm]	Noise	Response time [s]
Cross	13.3	1.34*E-6	100	0.94*E-4	100
2 lines transverse	38.5	1.83*E-6	150	0.88*E-4	100
Single line transverse	57.6	1.07*E-6	180	1.2*E-4	100
3 lines parallel	95.7	0.81*E-6	560	2.1*E-4	100
Single line parallel	1000	4.43*E-7	560	3.5*E-4	100

Table 2.1 Resistance, sensitivity, limit of detection and response time of 3-layers sensors to acetone vapours.

Morphology	Resistance [KOhm]	Sensitivity [1/ppm]	Limit-of-Detection [ppm]	Noise	Response time [s]
2 lines transverse	8,6	2,43*E-6	60	1.0*E-4	>3000
Single line transverse	8,9	2.18*E-6	75	1.3*E-4	>3000
3 lines parallel	50	1.74*E-6	200	1.4*E-4	>3000
Single line parallel	175	1.05*E-6	300	1.5*E-4	>3000

Table 2.2 Resistance, sensitivity, limit of detection and response time of 5-layers sensors to acetone vapours.

The results indicated that, for whatever investigated geometry, the three-layers sensors were all faster than penta-layers devices. Indeed, the response time for the three-layers devices was equal to 100 s, one order of magnitude lower than the one of penta-layers devices (>3000 s). In this last case, the real time response value couldn't be estimated because the sensor response didn't reach the saturation level in the investigated exposure time for each analyte concentration. This behaviour can be attributed to the physisorption mechanism of the gas molecules in the polymer matrix. At the nanoscale, the solvent molecules can very quickly enter in the free volumes of the amorphous phase and modify the CB/matrix interaction by adsorption. The inability of the penta-layer sensors to achieve the saturation condition can be attributed to the reduced surface/volume ratios with respect to the three-layer configuration because of the higher material quantity. Moreover, for all the investigated samples, when the analyte is removed, the resistance drop back to the initial values, revealing the complete desorption of the solvent molecules from the polymer matrix and full reversibility of the devices.

The correlation between the base resistance and sensitivity is confirmed in the case of penta-layers devices (see Table 2.2), which are characterized by a lower base resistance than the three-layers ones. Indeed, a higher number of layers of sensing

material increases the amount of the sensing material inducing the highest relative differential responses.

However, generally the dynamic responses of sensors with different geometries are strongly influenced by the base resistance R0. In fact, by comparing the different geometries of the three-layers configuration, the performances of the devices with ‘transverse’ geometry are better than the ones of the ‘parallel’ geometry devices in terms of the sensitivity, noise and the limit-of-detection (LoD) (see

Table 2.1). Both the increase of VOC sensitivity and the decrease of LoD and noise indicate an improvement of the performances corresponding to a lower base resistance of the devices. This behaviour can be easily explained by comparing the single-line geometries. Indeed, since the equivalent circuit of the ‘transverse’ geometry is composed by multiple resistors placed in parallel, the device transduction effect in this geometry is enhanced with respect to the ‘parallel’ geometry. The multiple-lines geometries are ruled by the same mechanism, even if in a more complex manner.

The different geometries were realized taking into account the transducer geometry and the minimum dimension of the printed sensing material line width. In particular, the cross geometry was projected in order to increase the sensing surface with respect to the ‘transverse’ single-line. The dynamic response of the cross device effectively showed an improvement with respect to the ‘transverse’ single-line in terms of both sensitivity and LoD, but in a less significant manner if compared with the ‘transverse’ two-lines geometry. This behaviour is easily explained since the printed material along the ‘parallel’ direction and not comprised between two contiguous fingers weakly influences the electrical response (second order effects). This statement is confirmed by the dynamic responses of the ‘parallel’ geometries (single- and three-lines) which showed the worst performances.

In Figure 2.9 the calibration curves of both the three-layers configurations (Figure 2.9a) and penta-layers (Figure 2.9b) are reported. The reported data for all the geometries are interpolated by linear fits. The calibration curves analysis allows to determine both the sensitivity (the angular coefficient of the calibration curve) and LoD parameters. The results indicated that the electrical response varies linearly as

the analyte concentration increases for all the manufactured chemical sensors in all the investigated concentration range (600, 1250, 2500, and 5000 ppm).

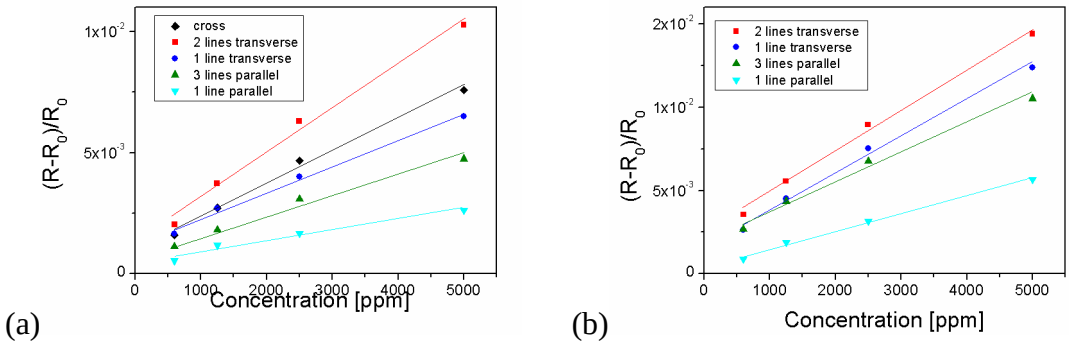

Figure 2.9 Calibration curves of the (a) three-layers and (b) penta-layers sensors for all the different geometries.

2.3 Flexible substrates for sensor device fabrication

The study reported in the previous paragraph indicates that the geometry with printed line 'transverse' to interdigitated contacts gives the best sensor performances in terms of sensitivity and limit of detection. Moreover, the three-lines configuration is preferred thanks to its faster response with respect to the penta-layers. These sensors were fabricated on alumina substrates which can be replaced with flexible ones. The feasibility of processing material solutions on flexible substrates replacing the rigid ones is a key role of the emerging inkjet printing technique.

The interaction ink/substrate system has fundamental role in the device performances since it induces different morphologies of the printed material. In this thesis activity, glass, PET (polyethylene terephthalate) and glossy paper (Epson) were employed as substrates for the inkjet printing deposition. The effect of the substrate morphology on the printed film quality and, hence, on the device performances upon exposure to acetone and ethanol vapours were investigated. Furthermore, a comparison with the alumina substrate was performed.

The sensible material (PS/CB) was printed with the optimized geometry on alumina substrate such as with lines 'transverse' to the interdigitated contacts in the configuration of overlapped 3-layers. It was necessary to optimize the deposition for PET and glass substrates by means of chemico-physical surface treatments such as

oxygen plasma (O_2) or carbon tetrafluoromethane plasma (CF_4). These treatments allow to modify the wetting of the ink/substrate system and the surface roughness of the substrate in order to obtain continuous printed lines.

2.3.1 Printing optimization by surface treatments

Overlapped drops of nanocomposite based ink were IJ-printed on patterned PET, glass and glossy paper substrates. For glass and PET substrates the spreading of the sensing material resulted not optimized for the presence of empty regions in the printed material in the case of PET substrate (Figure 2.10a) and for a not uniform and not controllable deposition in the case of glass substrate (Figure 2.10b). For the glossy paper substrate, thanks to its surface characteristic, the ink deposition was optimized without the application of any chemico-physical treatment (Figure 2.10c).

For PET and glass substrates, surface treatments were required to modify the wetting of the ink/substrate system. Oxygen plasma (O_2) and fluorine plasma (CF_4) treatments were employed to modify the surface energy of the substrates. A contact angle instrument (OCA20, Dataphysics) was used in order to evaluate the hydrophobicity and hydrofilicity of the surfaces by extiming the disperse and polar components of the surface energy. The measurements were made by dispensing on the substrates drops of water, as polar solvent, and dichloromethane, as apolar solvent, and by fitting the results with the Owen, Wendt, Rabel and Kaelble (OWRK) method [35].

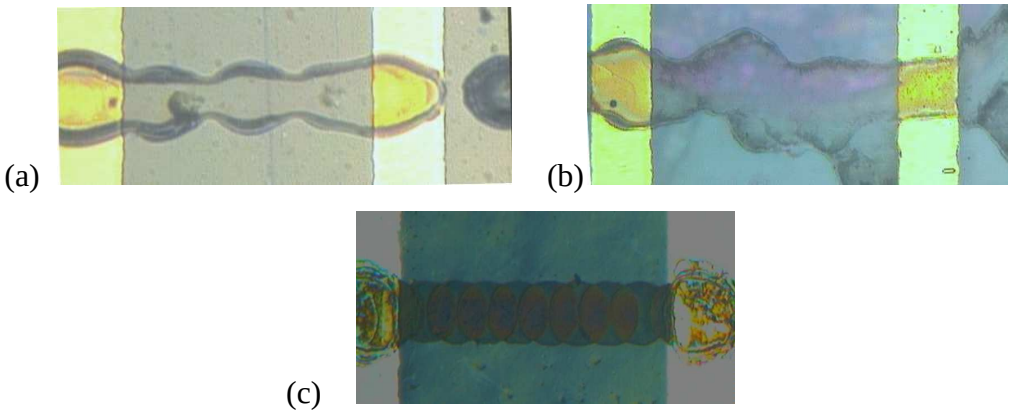

Figure 2.10 Optical images of the printed line on PET (a), glass (b) and glossy paper (c) substrates.

This measurement gives indication on the wetting of the ink/substrate system considering the measured value of the surface tension of the PS/CB equal to γ = 56 mN/m.

In Figure 2.11 are reported the 1 μL water droplets dispensed with the contact angle instrument on untreated and CF_4- and O_2-plasma treated PET and glass substrates.

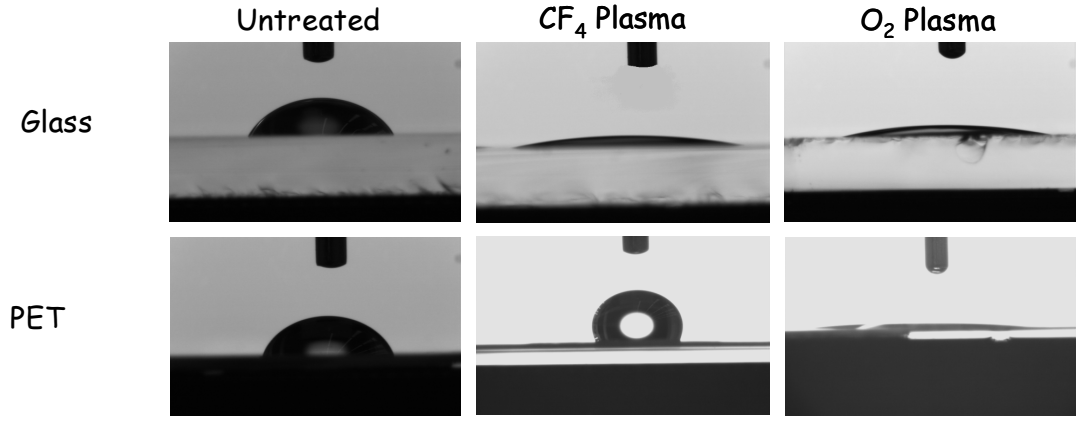

Figure 2.11 Water droplets on untreated and CF_4 and O_2 plasma treated glass and PET substrates

For PET substrate, CF_4 plasma treatment makes the substrate more hydrophobic (contact angle greater than 90°) while O_2 treatment makes it more hydrophilic (contact angle lower than 90°). Concerning the glass substrate, both CF_4- and O_2-plasmas make the substrate hydrophilic. Therefore, in the case of polymer substrate, the CF_4 plasma treatment results in the formation of a thin fluorinated layer making the substrate surface hydrophobic, while for the glass substrate this kind of treatment performs a double action, cleaning and etching, increasing the substrate surface energy making it more hydrophilic [36]. The analysis of the results of the contact angle measurements are summarized in Table 2.3.

Morphology	**Substrates**	**Rq [nm]**	**θpol [°]**	**θdisp [°]**	**Surface Energy [mN/m]**
Untreated	Glass	0.6	28.5	14.6	43.1
	PET	2.4	5.6	38.5	44.1
CF_4 plasma	Glass	0.7	24.7	35.8	60.5
	PET	4.3	0.4	13.5	13.9
O_2 plasma	Glass	0.7	32.2	44.9	77.1
	PET	2.5	30.7	50.0	80.7

Table 2.3 Summary of the substrate characteristics before and after plasma treatments: means roughness (Rq), polar component (θpol) and disperse component (θdisp) of the surface energy.

In detail, for glass substrate the plasma treatments don't modify the surface roughness but considerably increase the surface energy. Taking into account that a good wetting condition is obtained when the substrate surface energy is grater than the ink surface tension, the action of O_2 plasma on the glass surface consists in increasing its surface energy up tu 77 mN/m, consequently inducing the splashing of the ink on the target substrate. On the contrary, the CF_4 plasma allows to reach an intermediate surface energy value (SE = 60.5 mN/m) corresponds to an optimal deposition condition.

For PET substrate the CF_4 plasma treatment involves an increase of the surface roughness and a more significant decrease of the polar component of the surface energy than the apolar one, so making the substrate more hydrophobic. Despite the surface energy is lower than the surface tension, the higher roughness guarantees the formation of a continuous line by pinning the printed droplets. On the contrary, after the O_2 treatment, the higher surface energy of the substrate doesn't allow the formation of a continuous line and produce a not uniform condition with a splashing and not controllable deposition.

2.3.2 Sensor device fabrication

As showed in the previous paragraph the surface treatments can modify the roughness and the surface energy of the substrates. In particular, the CF_4 plasma optimizes the ink deposition for both glass and PET substrates. In Figure 2.12 are reported the printed line transverse to interdigitated contacts with a continuous and a well defined profile, as expected.

(a)  (b) 

Figure 2.12 Optical images of the printed line on PET substrate (a) and glass substrate (b) after CF_4 plasma treatment.

For the glossy paper substrate no treatment is needed for reaching a uniform and controllable printing. Indeed, this kind of substrate, specifically designed for the production of photographs, has a polyethylene layer buffer covering on one side of the paper because an even porosity is required to counteract the spreading of the ink.

The realized sensors on glass, PET and glossy paper substrates are illustrated in Figure 2.13.

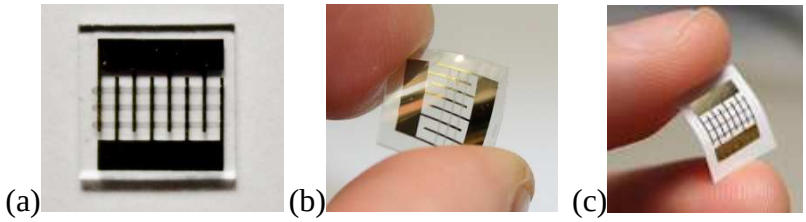

Figure 2.13 Picture of sensor devices on (a) glass, (b) PET and (c) glossy paper.

The morphology of the PS/CB printed on the different substrates was deeply investigated by means of Scanning Electron Microscopy (SEM) in order to correlate the sensitive material distribution with the devices performances.

The SEM images for glass, PET and glossy paper substrates are reported in Figure 2.14.

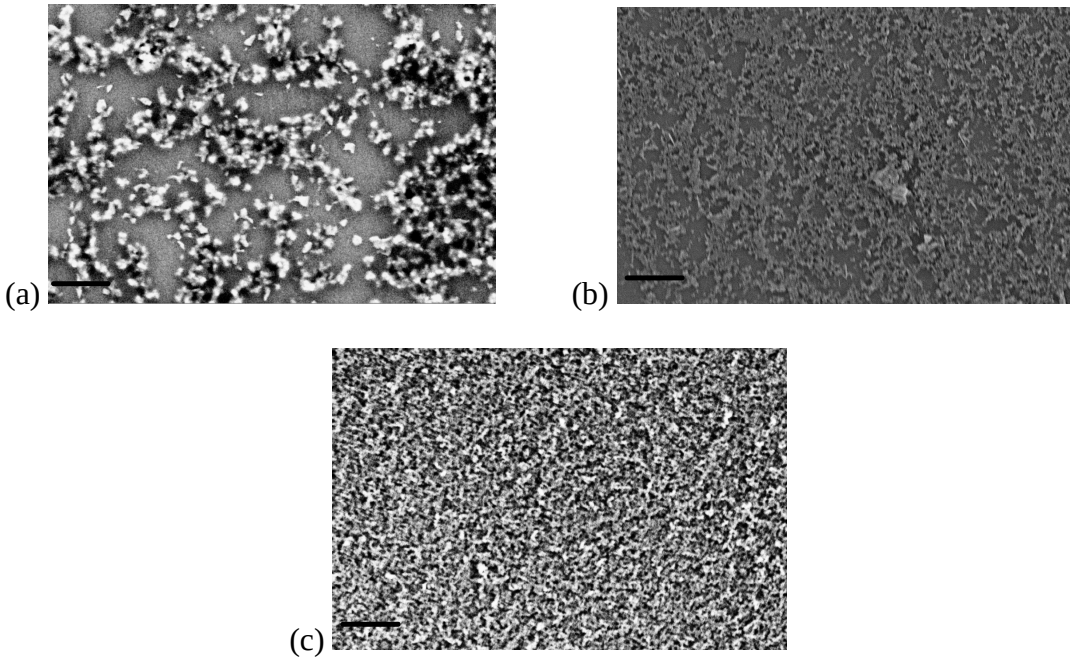

Figure 2.14 SEM images of PS/CB nanocomposite based ink printed on (a) glass, (b) PET and (c) glossy paper substrates. The reference bar is equal to 2 μm.

The SEM analysis shows the presence of percolative paths of the conductive filler in the polymer matrix for all the substrates. Moreover, for PET and, in particular, for glossy paper (Figure 2.14b,c) the CB distribution is more uniform than the glass substrate (Figure 2.14a), where empty regions alternated to a more concentrated areas are present. The morphology of the PS/CB printed on all the substrates is completely different from that observed on the alumina one (Figure 2.5). The last one, which is the most commonly employed in literature for its sensor performances, have a characteristic sliver morphology that increases the adhesion and the surface active area of the sensitive material. The different morphology observed on glass, PET and glossy paper can affect the adsorption of the organic vapours and, hence, the sensing performance of the devices.

2.3.3 Electrical characterization to acetone vapours

The devices electrical responses of the three layers devices to acetone vapors are shown in Figure 2.15 (a),(b),(c) for glass, PET and glossy paper substrates, respectively.

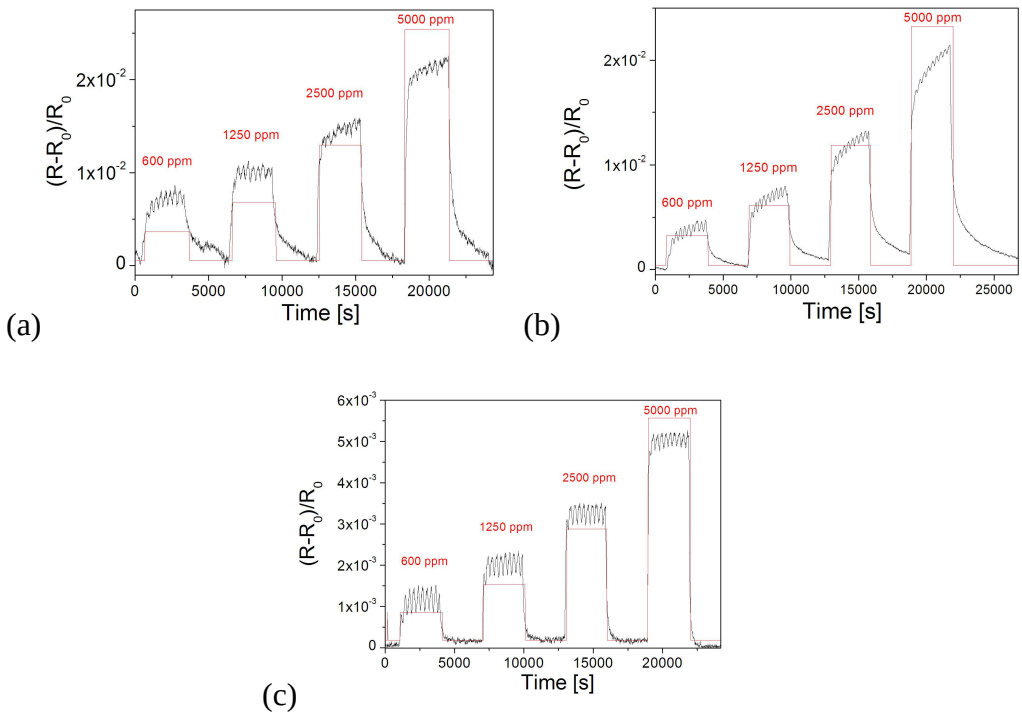

Figure 2.15 Electrical responses of 3-layers sensors on glass (a), PET (b) and glossy paper (c) in presence of acetone vapours.

The parameters that characterize the sensor performances, such as base resistance, sensitivity, limit of detection (LoD) and response time, are summarized in Table 2.4 for each substrate.

Substrate	Resistance [KOhm]	Sensitivity [1/ppm]	Limit-of-Detection [ppm]	Noise	Response time [s]
Glass	300	3.13 e-6	350	5.2 e-4	200
PET	135	3.67 e-6	50	1.1 e-4	>3000
Glossy paper	8,8	8.50 e-7	30	1.0 e-4	100

Table 2.4 Base resistance, sensitivity, limit of detection and response time of 3-layers sensors printed on glass, PET and glossy paper substrates to acetone vapours.

As showed in the dynamic response, the devices obtained on glass and PET substrates don't reach the saturation condition for all the analyte concentration. This effect could be due to the presence of printed edge where the large amount of sensitive material makes the adsorption of the solvent more difficult. On the contrary, the device on glossy paper showed the best sensor performances in terms of both response time and limit of detection, with respect to the other substrates and also alumina one thanks to the better ink-substrate interaction that indices to a better distribution of the CB filler in the polymer matrix printed on this substrate.

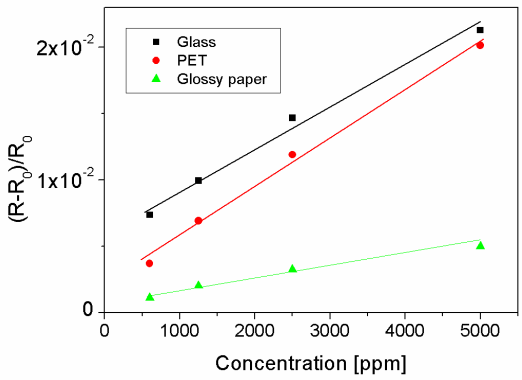

Figure 2.16 Calibration curves of the three-layers sensors exposed to acetone vapours fabricated on glass (square), PET (circle) and glossy paper (triangle).

In Figure 2.16 the calibration curves for the sensors fabricated on glass, PET and glossy paper are reported. The data reported in order to compare all the devices are interpolated by linear fits. For each substrate, the electrical response varies linearly as the analyte concentration increases from 600 to 5000 ppm.

2.3.4 Electrical characterization to ethanol vapours

All the fabricated sensors on the different substrates were characterized also under ethanol vapours. The exposition to this vapours was made in order to study the selectivity of the sensing material to different analytes.

The electrical responses to 600, 1250, 2500 and 5000 ppm of ethanol for the sensor realized on glass, PET and glossy paper substrates are reported in Figure 2.17.

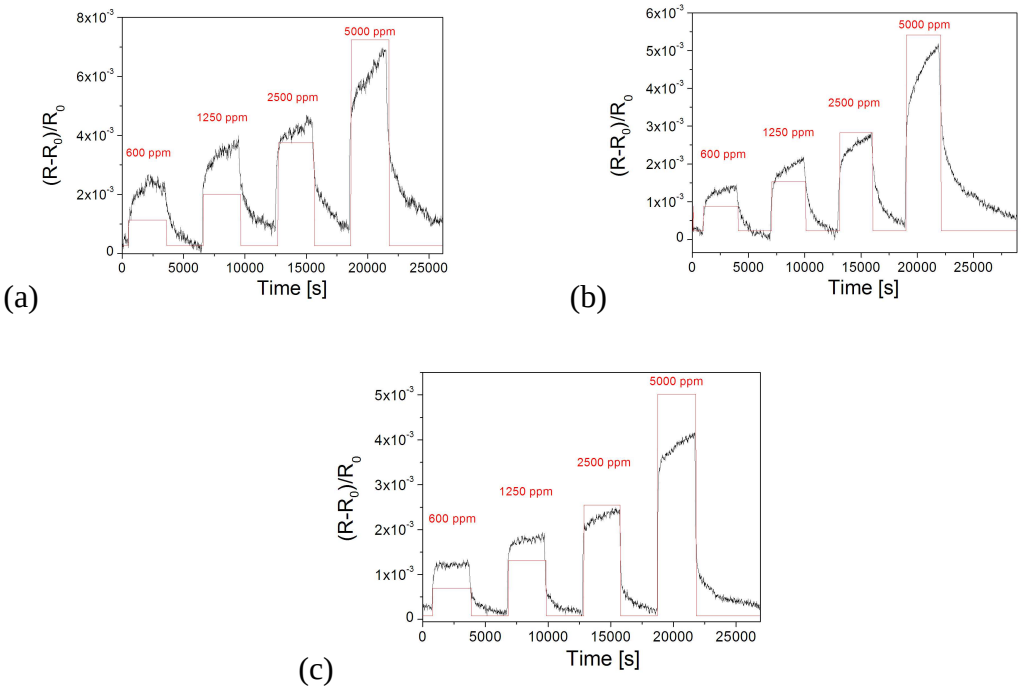

Figure 2.17 Electrical responses of 3-layers sensors on glass (a), PET (b) and glossy paper (c) to ethanol vapours.

In Table 2.5 the parameters that characterize the three sensors under ethanol vapours are summarized.

Substrate	Resistance [KOhm]	Sensitivity [1/ppm]	Limit-of-Detection [ppm]	Noise	Response time [s]
Glass	300	8,6 e-7	400	3.1 e-4	500
PET	135	7,8 e-7	150	1.9 e-4	>3000
Glossy paper	8,8	6,0 e-7	100	1.0 e-4	100

Table 2.5 Base resistance, sensitivity, limit of detection and response time of 3-layers sensors printed on glass, PET and glossy paper substrates to ethanol vapours.

As highlighted in the electrical responses, both glass and PET substrates don't reach the saturation condition neither at lower concentrations. On the contrary, the

sensor realized on glossy paper shows the best limit-of-detection and response time characteristics and reaches the saturation condition up to 2500 ppm in about 100 s.

In Figure 2.18, the calibration curves of the sensor devices in presence of ethanol vapours are reported. Even if the device on glass substrate shows the best sensitivity, the sensor on glossy paper has the lowest LoD, noise and response time thanks to the morphology induced by the suitable ink/substrate interaction which is confirmed by a very low base resistance.

In any case, the electrical response of all the sensors to ethanol vapours are worst of about one order of magnitude with respect to acetone. The worst performances could be explained considering that the ethanol is more polar than the acetone one. Because the polystyrene molecule, for its intrinsic chemical structure, has higher affinity to non-polar molecules, its sensitivity to ethanol vapour is lower than to acetone.

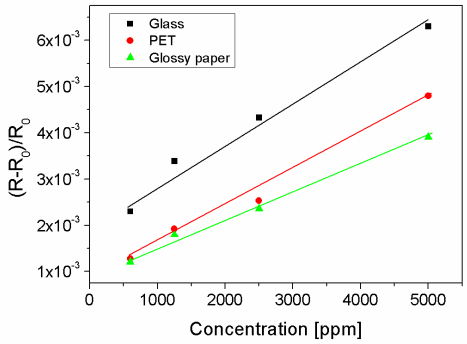

Figura 2.18 Calibration curves of the three-layers sensors on glass, PET and glossy paper exposed to ethanol vapours.

2.4 Summary

The second chapter of the thesis activity involved the manufacture and characterization of nanocomposite based chemical sensors on different, flexible and not flexible, substrates and investigated how their performances are related to printed film quality induced by the ink-substrate system interactions. The sensing material was deposited by means of ink-jet printing technique on alumina, glass, PET and glossy paper substrates. The sensing material morphology was characterized by means of SEM and AFM analysis. The sensor responses were measured upon

exposure to organic vapours (acetone, ethanol) and analyzed in terms of base resistance, limit of detection, sensitivity and response time.

Concerning the alumina substrate, the relation between the device performances and the sensing material geometry and thickness was investigated. Different geometries, with one or more lines differently orientated with respect to the transducer fingers, were realized. To this aim, the inkjet printing technology was employed to deposit the sensing material selectively taking advantage by the patterning capability of this deposition method and different geometries were realized in extremely easy and controlled manner. Moreover for each geometry, the effect of thickness on sensor performances was investigated by fabricating sensing film with different thickness of the sensing film by overlapping three- and penta-layers.

The results pointed out that the sensing material realized with less number of layers improves the device performances in terms of response time thanks to a suitable surface/volume ratio. Moreover, the PNCs based chemical sensors fabricated by IJ printing lines ‘transverse’ to the fingers of the interdigitated electrodes showed the best sensitivity and limit-of-detection. Hence, this optimized configuration was used for the sensors realized on glass, PET and glossy paper substrates.

For glass and PET substrates surface treatments were employed in order to optimize the wetting of each ink-substrate system. In particular, CF_4 plasma treatment allows to obtain a continuous and more uniform printing condition of the PS/CB ink on both the substrates. The glossy paper substrate doesn’t require any surface treatment because the deposition is already optimized.

All the sensors realized showed good electrical performances to acetone and ethanol vapours. The inkjet printed sensors on glossy paper showed the best performances to the different analytes in terms of response time and limit of detection.

The employment of the glossy paper as substrate for sensing applications opens new perspectives in organic electronics being this material environmentally friendly and particularly adapt to application fields like food distribution, electronics and textile industry.

Bibliography

[1] M.V.M. Rao, Y.K. Su, T.-S. Huang, M.-L. Tu, S.-S. Wu, C.-Y. Huang, Enhanced Performance of Polymer Light Emitting Devices Using Zinc Oxide Nanoparticle with Poly(vinylcarbazole), J. Electrochem. Soc. 157 (2010) H832-H836.

[2] V.L. Colvin, M.C. Schlamp, A.P. Alivisatos, Light-emitting diodes made from cadmium selenide nanocrystals and a semiconducting polymer, Nature. 370 (1994) 354-357.

[3] M.C. Schlamp, X. Peng, A.P. Alivisatos, Improved efficiencies in light emitting diodes made with CdSe(CdS) core/shell type nanocrystals and a semiconducting polymer, J. Appl. Phys. 82 (1997) 5837.

[4] T. Nyberg, Macromolecular nanoelectronics, Current Applied Physics. 2 (2002) 27-31.

[5] Z. Liu, D. He, Y. Wang, H. Wu, J. Wang, Solution-processable functionalized graphene in donor/acceptor-type organic photovoltaic cells, Solar Energy Materials and Solar Cells. 94 (2010) 1196-1200.

[6] S. Douadi-Masrouki, B. Frka-Petesic, M. Save, B. Charleux, V. Cabuil, O. Sandre, Incorporation of magnetic nanoparticles into lamellar polystyrene-b-poly(n-butyl methacrylate) diblock copolymer films: Influence of the chain end-groups on nanostructuration, Polymer. 51 (2010) 4673-4685.

[7] Y.S. Kim, Fabrication of carbon black-polymer composite sensors using a position-selective and thickness-controlled electrospray method, Sensors and Actuators B: Chemical. 147 (2010) 137-144.

[8] K.J. Albert, N.S. Lewis, C.L. Schauer, G.A. Sotzing, S.E. Stitzel, T.P. Vaid, et al., Cross-Reactive Chemical Sensor Arrays, Chemical Reviews. 100 (2000) 2595-2626.

[9] R.D.S. B J Doleman, Use of compatible polymer blends to fabricate arrays of carbon black-polymer composite vapor detectors., Analytical chemistry. 70 (1998) 2560-4.

[10] M.C. Lonergan, E.J. Severin, B.J. Doleman, S.A. Beaber, R.H. Grubbs, N.S. Lewis, Array-Based Vapor Sensing Using Chemically Sensitive, Carbon Black−Polymer Resistors, Chemistry of Materials. 8 (1996) 2298-2312.

[11] M.E. Koscho, R.H. Grubbs, N.S. Lewis, Properties of Vapor Detector Arrays Formed through Plasticization of Carbon Black−Organic Polymer Composites, Analytical Chemistry. 74 (2002) 1307-1315.

[12] C.K. Ho, E.R. Lindgren, K.S. Rawlinson, L.K. McGrath, J.L. Wright, Development of a Surface Acoustic Wave Sensor for In-Situ Monitoring of Volatile Organic Compounds, Sensors. 3 (2003) 236-247.

[13] C.K. Ho, R.C. Hughes, In-Situ Chemiresistor Sensor Package for Real-Time Detection of Volatile Organic Compounds in Soil and Groundwater, Sensors. 2 (2002) 23-34.

[14] H. Lei, W.G. Pitt, L.K. McGrath, C.K. Ho, Modeling carbon black/polymer composite sensors, Sensors and Actuators B: Chemical. 125 (2007) 396-407.

[15] W.P. Carey, B.R. Kowalski, Chemical piezoelectric sensor and sensor array characterization, Analytical Chemistry. 58 (1986) 3077-3084.
[16] F. Zee, J.W. Judy, Micromachined polymer-based chemical gas sensor array, Sensors and Actuators B: Chemical. 72 (2001) 120-128.
[17] M.P. Eastman, R.C. Hughes, G. Yelton, A.J. Ricco, S.V. Patel, M.W. Jenkins, Application of the Solubility Parameter Concept to the Design of Chemiresistor Arrays, J. Electrochem. Soc. 146 (1999) 3907-3913.
[18] A. Marquez, J. Uribe, R. Cruz, Conductivity variation induced by solvent swelling of an elastomer–carbon black–graphite composite, Journal of Applied Polymer Science. 66 (1997) 2221-2232.
[19] D. Goustouridis, K. Manoli, S. Chatzandroulis, M. Sanopoulou, I. Raptis, Characterization of polymer layers for silicon micromachined bilayer chemical sensors using white light interferometry, Sensors and Actuators B: Chemical. 111-112 (2005) 549-554.
[20] S. Chatzandroulis, D. Goustouridis, I. Raptis, Characterization of polymer films for use in bimorph chemical sensors, J. Phys.: Conf. Ser. 10 (2005) 297-300.
[21] A. Convertino, G. Leo, M. Tamborra, C. Sciancalepore, M. Striccoli, M.L. Curri, et al., TiO2 colloidal nanocrystals functionalization of PMMA: A tailoring of optical properties and chemical adsorption, Sensors and Actuators B: Chemical. 126 (2007) 138-143.
[22] A. Carrillo, I.R. Martín-Domínguez, A. Márquez-Lucero, Modeling and experimental testing of the effect of solvent absorption on the electric properties of styrene butadiene rubber/carbon black chemical sensors, Sensors and Actuators B: Chemical. 113 (2006) 477-486.
[23] A. De Girolamo Del Mauro, A.I. Grimaldi, V. La Ferrara, E. Massera, M.L. Miglietta, T. Polichetti, et al., A Simple Optical Model for the Swelling Evaluation in Polymer Nanocomposites, Journal of Sensors. 2009 (2009) 1-6.
[24] S. Shang, L. Li, X. Yang, Y. Wei, Polymethylmethacrylate-carbon nanotubes composites prepared by microemulsion polymerization for gas sensor, Composites Science and Technology. 69 (2009) 1156-1159.
[25] J. Lu, B.J. Park, B. Kumar, M. Castro, H.J. Choi, J.-F. Feller, Polyaniline nanoparticle–carbon nanotube hybrid network vapour sensors with switchable chemo-electrical polarity, Nanotechnology. 21 (2010) 255501.
[26] F. Cakar, M.R. Moroglu, H. Cankurtaran, F. Karaman, Conducting poly(ether imide)-graphite composite for some solvent vapors sensing application, Sensors and Actuators B: Chemical. 145 (2010) 126-132.
[27] M.C. Lonergan, E.J. Severin, B.J. Doleman, S.A. Beaber, R.H. Grubbs, N.S. Lewis, Array-Based Vapor Sensing Using Chemically Sensitive, Carbon Black−Polymer Resistors, Chemistry of Materials. 8 (1996) 2298-2312.
[28] Briglin S.M., Freund M.S., Tokumaru P., Lewis N.S., Exploitation of spatiotemporal information and geometric optimization of signal/noise performance using arrays of carbon black-polymer composite vapor detectors, Sensors and Actuators B: Chemical. 82 (2002) 54-74.
[29] B. Ballarin, A. Fraleoni-Morgera, D. Frascaro, S. Marazzita, C. Piana, L. Setti, Thermal inkjet microdeposition of PEDOT:PSS on ITO-coated glass and characterization of the obtained film, Synthetic Metals. 146 (2004) 201-205.

[30] Y. Yoshioka, G.E. Jabbour, Desktop inkjet printer as a tool to print conducting polymers, Synthetic Metals. 156 (2006) 779-783.
[31] F. Loffredo, G. Burrasca, L. Quercia, D.D. Sala, Gas Sensor Devices Obtained by Ink-jet Printing of Polyaniline Suspensions, Macromolecular Symposia. 247 (2007) 357-363.
[32] F. Loffredo, A.D.G.D. Mauro, G. Burrasca, V. La Ferrara, L. Quercia, E. Massera, et al., Ink-jet printing technique in polymer/carbon black sensing device fabrication, Sensors and Actuators B: Chemical. 143 (2009) 421-429.
[33] J. Lu, B. Kumar, M. Castro, J.-F. Feller, Vapour sensing with conductive polymer nanocomposites (CPC): Polycarbonate-carbon nanotubes transducers with hierarchical structure processed by spray layer by layer, Sensors and Actuators B: Chemical. 140 (2009) 451-460.
[34] P. Atkins, Atkins' Physical Chemistry, 7th ed., Oxford Higher Education, 2001.
[35] D.K. Owens, R.C. Wendt, Estimation of the surface free energy of polymers, Journal of Applied Polymer Science. 13 (1969) 1741-1747.
[36] C. Sele, T. von Werne, R. Friend, H. Sirringhaus, Lithography-Free, Self-Aligned Inkjet Printing with Sub-Hundred-Nanometer Resolution, Advanced Materials. 17 (2005) 997-1001.

CHAPTER 3
OPTICAL STRUCTURES

Photonics is one of the six key enabling technologies (Kets) identified by the European Commission as essential to realize the great challenges of the future in a competitive way. Within the world of photonics, the Solid State Lighting (SSL) has held great interest especially thanks to the many applications arising from the possible use of the inkjet printing technology.

In recent years, the inkjet printing technique is attracting more and more interest in the framework of optical structures fabrication, overcoming the drawbacks of the traditional techniques which usually require multiple complex processing steps making the fabrication costly.

Inkjet printing technique is generally used as tool for positioning small quantities of a liquid material on a target substrate. For this reason it can be used as a direct method for the fabrication of high-quality and high-precision optical microstructures (i.e. microlenses, microholes, polymer texturing…) with the great advantage to be extremely versatile in definition of the patterns of microstructures and in the employed polymer materials.

An interesting application of the inkjet printing is the so called ‘inkjet etching’ (IJE) that consists in depositing drops of solvent or solvent mixtures onto a soluble polymer layer. This technique allows to structure the polymer film with the profile that can have concave or convex shape by varying the mixing ratio of the solvents.

In this chapter, the structuring of some polymeric layers (polyimide and polystyrene) by solvents (N-Methyl-2-pyrrolidone (NMP), toluene (TOL)) and solvent mixture (TOL:NMP) at different volume mixing ratios were studied and the effect of the printing parameters on the microstructure profile was investigated.

Moreover, optical microstructures were also fabricated by inkjet additive deposition of Poly(methyl methacrylate) (PMMA) solutions dissolved in different solvents (NMP, TOL) and the effects of the printing parameters on the shape and the geometry and, hence, on the optical characteristics of the microstructures were studied.

3.1 Introduction to polymer microstructuring

The structuring of materials is employed for different applications such as realization of biochips and micropatterned cell arrays [1,2], patterning for building 'bank' structures [3], fabrication of microlens array [4,5] and texturing of surfaces [6] in order to improve the efficiency of OLED (organic light-emitting diode) and photovoltaic devices [7,8]. Several methods are proposed for polymer microstructuring and normally they use costly and multiple process steps. One of the most innovative method is the inkjet etching (IJE), an application of the inkjet printing (IJP) technology. The IJE, a single-process technique, consists in depositing pure solvent or mixture of solvents onto a soluble polymer layer, creating microstructures whose shape is function of the mixing ratio.

In general, when a single-solvent drop is printed, a crater-shaped microstructure is created on the polymer surface. Indeed, when the solvent drop hits the polymer layer, the polymer is locally dissolved, carried from the sessile drop centre to the edges and deposited there. This phenomenon occurs owing to the maximum of the evaporation rate and to the drop pinning at the three-phase contact line [9-13]. The motion of this convective flow inside the drop and directed towards its rim leads to a not uniform solute deposition with an accumulation of material at the edges, at the end of the drying process [14,15]. This phenomenon is known as "coffee-stain effect" [9,13,16].

Additionally, the redistribution of the polymer dissolved by a single-solvent drop also depends on the contribution of the Marangoni flow but in less significant way than the diffusive flow. The Marangoni flow is related to the temperature gradient of the sessile drop, and, hence, to the different surface tensions at the droplet liquid-air interface, and generates a solute motion from droplet rim to the centre [17]. The contribution of the Marangoni flow becomes more important in the definition of the final profile of the polymer when a dual-solvent system formed by solvents with different evaporation rates is employed. By using a mixture of high- and low-boiling point solvents, a concentration gradient of one solvent opposite to the concentration gradient of the other solvent is generated along the sessile drop radius. In this case, the solvent volatility and the surface tension properties combined with the mixing

ratio allow to control the capillary flows inside the droplet and to vary the microstructure shape from concave to convex.

Moreover, by changing the number of the drops of the pure solvent or the solvent mixture, the morphological properties and the geometry of the structures also change [13].

3.2 Inkjet etching of polymer surface

The polymer substrates employed for the IJE process were polyimide (PI) and poly(styrene) (PS), chosen for their good optical transmission properties in the spectral range and thermo-mechanical properties.

Commercial glass substrates purchased from Schott were cleaned by sonication with deionised water, acetone and isopropanol, dried with nitrogen and finally placed in oven at 130 °C for 1 hour.

After cleaning process, the PI and PS polymeric films were deposited on glass substrates by means of a Brewer Science Model 100 spin coater. The PI film, 1 μm thick, was spun at 5000 rpm for 30 s employing a 2 mL volume of the commercial solution (PI 2556) purchased from HD Microsystems. The PS sample was deposited by employing 2 mL of a solution of the commercial PS (Aldrich, average Mw ~ 350,000) dissolved in chlorobenzene at 90 °C for 30 min with a concentration of 15 % (w/w). The PS film thickness was 5.3 μm by spin-coating at 500 rpm for 20 s.

All the polymeric samples were placed on a hot plate at 100 °C for 15 min in order to completely remove the solvent.

N-methyl-2-pyrrolidon (NMP) and Toluene (TOL) were chosen as solvents because they dissolve the investigated polymers and have good chemico-physical properties for the inkjet printing process. Drops of NMP and TOL were inkjet printed onto the PI and PS layers, respectively. Moreover, the structuring of the PS film was performed also by printing TOL:NMP mixtures at different mixing ratios (1:1, 1.5:1, 1.8:1, 2:1, 2.3:1, 3:1). NMP was chosen for the PI structuring because the precursor monomers of the purchased PI are dissolved in it. As for the PS structuring, the choice of using TOL as single-solvent system and TOL and NMP as mixture

components arises from the fact that both dissolve the PS layer and are miscible together. Furthermore, these solvents have different volatility and surface tension properties (TOL: T_b = 110.6 °C, γ = 28.53 mN/m; NMP: T_b = 202 °C, γ = 40 mN/m) and their evaporation rates are suitable for inkjet printing processing.

The droplet depositions were performed by means of the inkjet equipment already described in the chapter 1 of this thesis, employing printhead with 50 or 70 μm opening nozzle corresponding to 90 or 180 pL droplet volume.

For the PS layer, sequences of TOL and TOL:NMP droplets were printed by means of the 50 μm opening nozzle printhead at the 6.7 Hz drop emission frequency and 1 mm/s printhead speed with a spacing between the droplets of 160 μm so creating a square array of microstructures on the polymer layer.

Similarly, for the PI layer, sequences of NMP droplets were printed by means of the 70 μm opening nozzle printhead at the 5 Hz drop emission frequency and 2 mm/s printhead speed with a spacing between the droplets of 400 μm.

After the structuring, only PI samples were thermally treated with a curing process at 200 °C for 30 min in air and at 300 °C for 1 hour in nitrogen atmosphere.

3.2.1 PI structured by NMP

The inkjet etching process using a single solvent system was employed onto PI film. By inkjet printing NMP drops on the polymer layer, crater-shaped microstructures form on polymer surface at the end of the solvent evaporation. The typical 2-dimensional profile of the microstructure has a central spherically shaped cavity and two lateral humps as shown in Figure 3.1.

In Figure 3.1 the structural parameters that characterize the microcrater profile are also reported: W_c is the width at cavity bottom (W_c = 0 in the case represented in Figure 3.1), W_o the internal diameter, W_e the diameter at the cavity top, W_{tot} the external diameter, H_{ec} the total depth of the cavity, and, finally, H_e and H_c are the edge height and the cavity depth with reference to the unstructured external polymer surface, respectively. These geometrical parameters are pointed in order to quantitatively monitor as the microstructure profile changes by varying the printing

conditions. The profilometric analysis employed to determine the profile and its structural parameters was also used to investigate the root-mean-square roughness inside the cavity which resulted of about 10-15 nm. Moreover, this investigation showed that no cracks are on the microstructured polymer surface indicating that, combined with the roughness information, the structured polymer can be used in good quality optical applications.

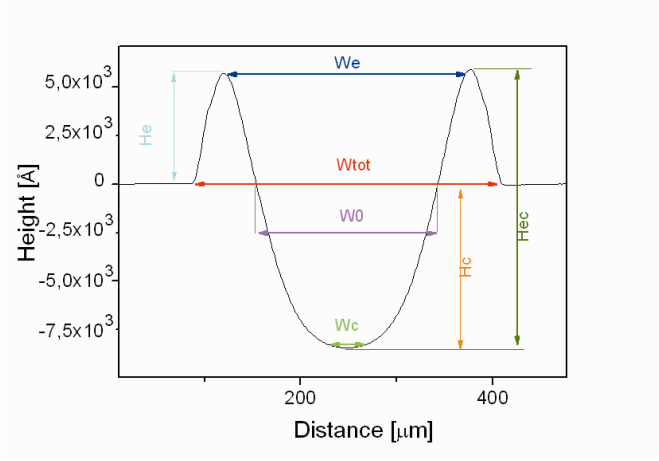

Figure 3.1 Profile of microcavity manufactured by printing a NMP drop on PI film and its geometrical parameters.

Furthermore, the profile reported in Figure 3.1 also shows that the depth of the microcavity realized by printing the single drop is by far less than the thickness of the PI film (1 μm).

In order to investigate the effect of the number of the printed drops (N_D) on the microstructure geometry, single and multiple drops were deposited on the polymer layer. The profiles of the manufactured microstructure by printing one, two and three NMP drops on the PI film are reported in Figure 3.2a. As the number of the inkjet printed droplets increases, the microcavity geometrical parameters also increase. The Figure 3.2b and Figure 3.2c report the values of the microstructure parameters as function of N_D. It can be observed that the external diameter increases less significantly than the total depth as N_D increases. This can be explained as follows. With the exception of the first inkjet printed droplet that hits a uniform polymer surface, the next droplets, deposited with the same volume and in the same place of the first one after a certain delay, meet the cavity-shaped polymer surface and converge towards its bottom. Thus, the multiple droplets remove the polymer mainly from the cavity bottom rather than from its edges appreciably modifying the total

depth (47 % percentage variation) and leaving the external diameter almost invariable (9 % percentage variation).

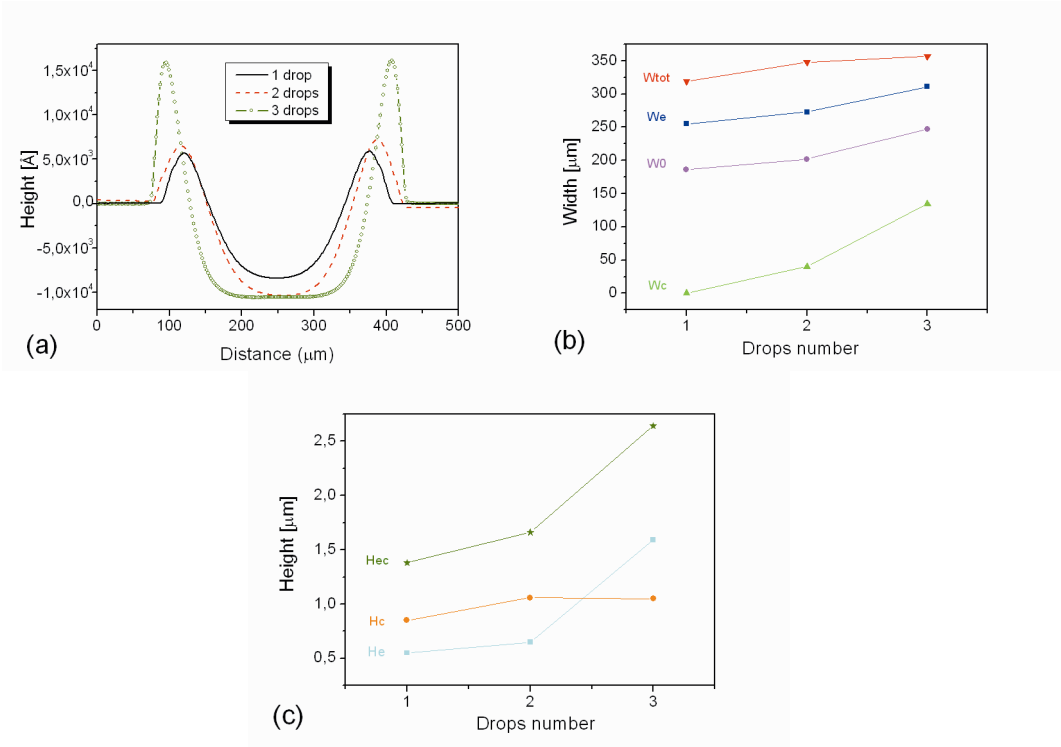

Figure 3.2 (a) Profiles of the PI microstructures manufactured by printing 1, 2 and 3 drops of NMP. Geometrical parameters of each cavity, (b) diameter and (c) depth, as functions of the number of drops.

The flat bottom of the microcavity manufactured by inkjet printing three NMP drops indicates that the volume amount of the deposited solvent is enough for dissolving and completely removing the polymer along all the thickness, so reaching the substrate.

The effect of the substrate temperature on the microstructure profile was also investigated. In Figure 3.3 is reported the profile of the PI microstructure fabricated by printing the single NMP droplet on the polymer layer and keeping the substrate at 50 °C as comparison with the microstructure manufactured at ambient temperature. Moreover, the profiles of samples manufactured in the same temperature conditions and depositing two NMP droplets were also characterized and the geometrical parameter values are shown in Figure 3.4. The results of Figure 3.3 and Figure 3.4 indicate that the higher temperature induces a cavity diameter decrease and a depth increase due to the fact that it makes the polymer softer and, in addition, the deposited droplet, evaporating more quickly, wets a smaller polymer surface. It is

important to highlight that T = 50 °C is lower than the requested temperature for inducing the PI curing process. The effect of the multiple drops on the geometrical parameters at higher temperature is the same as observed at T_{amb}. Furthermore, the polymer film temperature appears as the printing parameter that influences the microstructure profile in more significant manner.

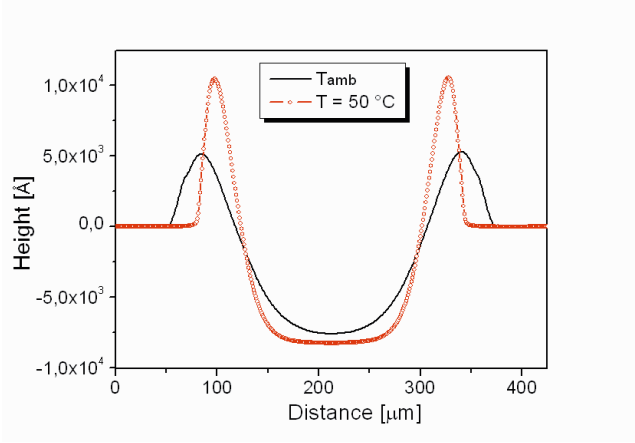

Figure 3.3 Profiles of the PI microstructures manufactured by printing NMP single drop with the substrate at ambient temperature (T_{amb}) and heated at T = 50 °C.

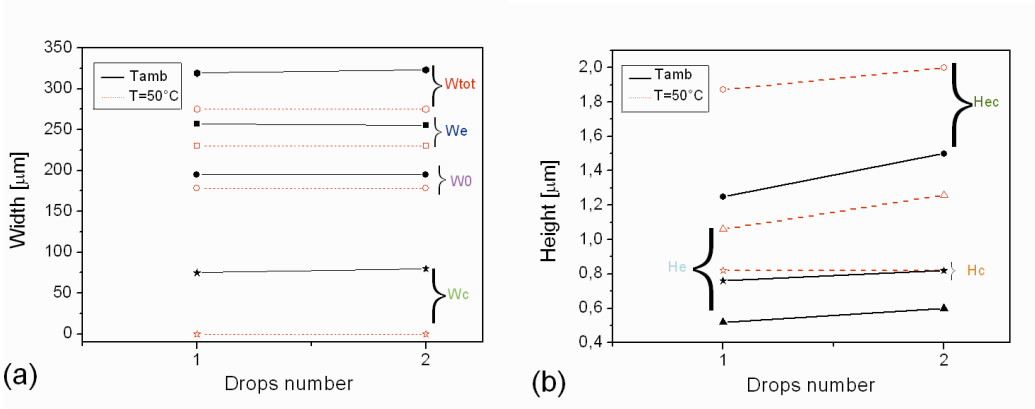

Figure 3.4 Geometrical parameters (diameter (a) and depth (b)) of the cavities fabricated at T_{amb} and T = 50 °C as functions of the number of the printed NMP drops.

After structuring, the PI film was thermally cured so turning completely insoluble to NMP solvent. Indeed, the cure heating cycle (at 200 °C for 30 min in air and at 300 °C for 1 hour in nitrogen atmosphere) converts the precursor film (polyamic acid) to insoluble polyimide and dries out the residual solvent. The heat treatment of the precursor film causes a drastic change in the backbone structures toward stiffer and more planar chain structures inducing dramatic changes in the mechanical properties. In confirmation, tests of printing of NMP drops on the treated polymer

film demonstrated that no polymer surface structuring can be performed and so no microstructure can be created further on.

3.2.2 PS structured by TOL

Preliminary printing tests were performed by depositing several solvents (toluene, N-Methyl-2-pyrrolidone, n-Butyl acetate, tetrahydrofuran, benzene) on the PS polymer film in order to define the process parameters useful to create repeatable structures. For whatever solvent, it was observed that 50 °C substrate temperature was the necessary condition for the repeatability of the microstructuring process. Since the solvent droplet deposited on heated polymer layer evaporates more rapidly, the drying process and the polymer redistribution are so fast that fewer variables are involved in the structuring process allowing a better control of the microstructure profiles. Therefore, all the prints on the PS layer, described in the following, were carried out with the heated substrate (50 °C).

The microstructure profile obtained by printing the single TOL drop on the PS layer, shown in Figure 3.5, is crater-shaped, very similar to that performed on the PI film structured by NMP. The influence of the number of the printed droplets on the microcavity geometrical parameters was analyzed for this solvent-polymer system, too. As in the study of PI structured by NMP it was demonstrated that the effect of the multiple droplets is more dominant on the cavity depth rather than on the diameter, same behaviour was registered with the TOL-PS system. By focusing the attention on the depth parameters, namely the cavity depth and the edge height in reference to the unstructured external polymer surface (Y1 and Y2 in Figure 3.5, respectively), they linearly increase as function of N_D as shown in Figure 3.6.

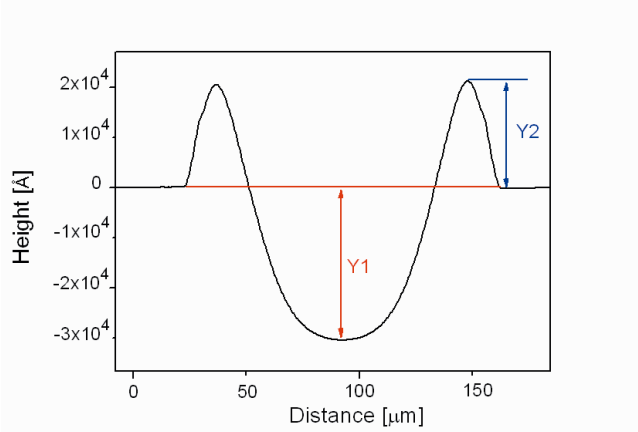

Figure 3.5 Profile of microcavity manufactured by printing a TOL drop on the PS film and its geometrical parameters.

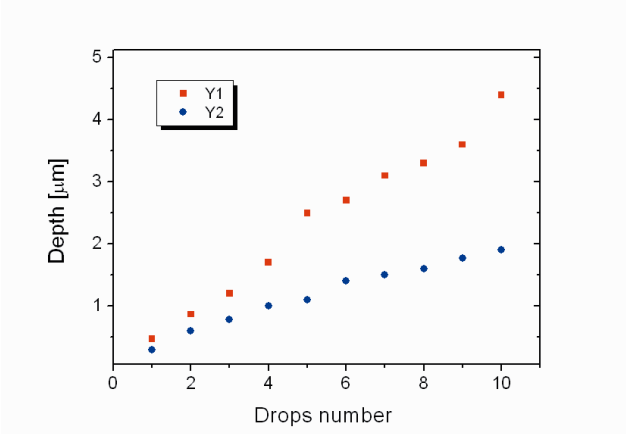

Figure 3.6 PS microcavity geometrical parameters (Y1, cavity depth, and Y2, edge height) as function of the number of TOL drops.

3.2.3 PS structured by TOL:NMP

Successively, PS structuring was carried out by employing a dual-solvent system. The profiles of the manufactured structures on the PS layer by depositing single drops of mixtures of TOL and NMP at different volume ratios and keeping the heated substrate (50 °C) are shown in Figure 3.7. The co-presence of different solvents in the droplet induces a polymer redistribution, after its dissolution, that basically depends on the chemico-physical properties of each solvent and also on volume ratio in the mixture. In detail, after the mixture drop deposition, the fast evaporation at the sessile drop rim leaves there a higher concentration of the less volatile component (NMP) that, in this case, has the higher surface tension promoting a Marangoni flow from the centre to the edge. By increasing the more

volatile component content (TOL), most of the dissolved polymer piles up in the centre as it is clear in Figure 3.7 for the TOL:NMP mixing ratios ranged from 1.8:1 to 2.3:1. Further increasing of the TOL content in the mixture (TOL:NMP 3:1) modifies the microstructure generating a complex shape with a crater on the pile top. This is the consequence of the created compositional gradient which generates an additional flow from the outer to the centre, already visible in the profile related to the 1:1 mixing ratio shown in Figure 3.7. Indeed, the rim of this profile is characterized by two humps on the same side, more evident if compared to the profile of the microstructure realized by the pure solvent drop (Figure 3.5), and the internal one, in particular, is just due to the flow directed towards the inside.

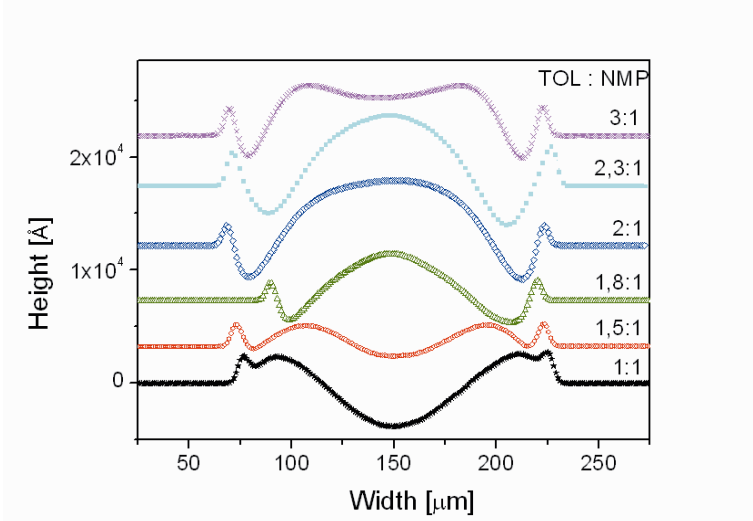

Figure 3.7 PS microstructure profiles realized by printing TOL and NMP mixture drops at different mixing ratios.

Moreover, by printing multiple drops onto the polymer layer the microstructure profile was also varied. In Figure 3.8 are shown the profiles obtained by depositing one, three and five droplets for 1:1, 1.5:1, 2.3:1 and 3:1 mixing ratio. The reported profiles are shifted along the height axis for clarity in the reading. It appears that a higher number of drops modifies mainly the depth and height with respect to the diameter leaving the shape almost unchanged. In particular, the diameter varies in less significant manner with respect to the height of the microstructure. This behaviour is understandable because, with the exception of the first printed droplet which meets the flat polymer surface, the next droplets hit a structured surface that holds them limiting the further spreading. As a result, the dissolved polymer was mainly removed from the bottom of the cavity as for TOL:NMP mixing ratios of 1:1

and 1.5:1, otherwise it largely piled up in the centre as for TOL:NMP mixing ratios of 2.3:1 and 3:1. In these last cases, the polymer microstructures can be used as microlenses in optical structures.

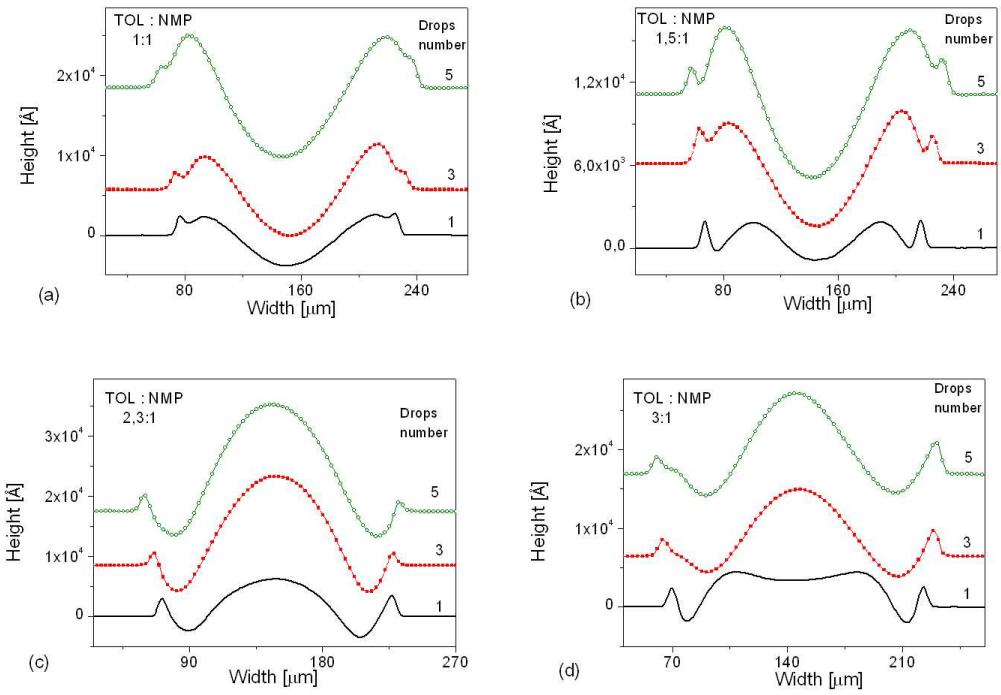

Figure 3.8 Profiles of the PS microstructures manufactured by printing 1, 3 and 5 drops of TOL:NMP mixtures at volume mixing ratios (a) 1:1, (b) 1.5:1, (c) 2.3:1, and (d) 3:1.

3.2.3.1 Optical characterization via Mach-Zehnder interferometer

The convex-shaped microstructures were optically investigated by means of a Mach-Zehnder system in confocal configuration. A Mach–Zehnder interferometer is employed because this system introduces a small measurement error being a single-path interferometer [18]. Indeed, in general the single-path interferometer is preferable to that double-path one (for example, Twyman–Green system) to analyze optical components that have to be utilized in transmission mode and to reduce the measurement errors in evaluating the microlens aberrations.

The Mach-Zehnder interferometer is schematically shown in Figure 3.9 and described in the following. The unpolarized light coming from a He-Ne laser (534

nm) passes through a beam-expander; the emerged beam, after reflecting by a mirror (M1), is divided in amplitude by a polarized beam splitter (PBS1) where the p-polarized component is transmitted into the test path and the s-polarized component is reflected into the reference path. The reference wave, deflected by a mirror driven by a piezoelectric stage, passes through a half-wave plate (HWP1) to rotate its polarized state, then through a neutral density filter and, finally, is recombined with the test wave at a beam splitter (BS2). The test beam passes through a neutral density to adapt the intensities of the test wave and the reference wave in order to optimize the interferogram contrast. The test wave is focused on the under-test microstructure by a microscope objective (MO1) in confocal position. The emerging wave is expanded by a microscope objective (MO2), placed itself in a confocal position with a lens (L1) and recombined with the reference wave at BS2. Finally, the light emerging from the interferometer is collected by a further lens (L2) and sent into the camera.

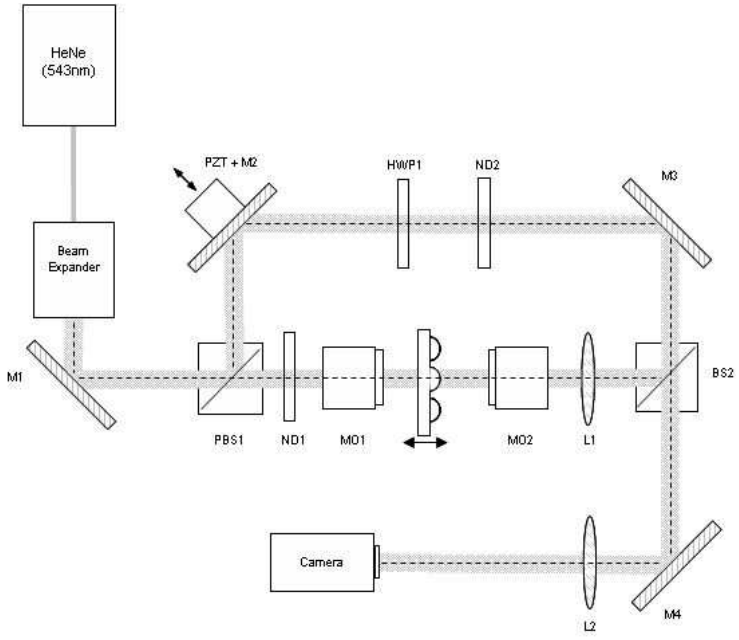

Figure 3.9 Scheme of the Mach-Zehnder interferometer system.

Since, as reported in the previous paragraph, the structure generated by five drops of the 2.3:1 TOL:NMP mixture had the highest value of the ratio between the central peak height and its diameter at the bottom, the interferometric analysis relative to this specific microstructure is reported as example.

In Figure 3.10 is reported the three-dimensional profile of the microlens obtained printing five drops of the 2.3:1 TOL:NMP mixture. The measurements of the geometrical parameters by the profilometric analysis allowed to estimate the focal length by using the following equation:

$$f = \frac{R}{n-1} \qquad \text{(eq.3.1)}$$

where n is the refractive index of the material and R is the radius of curvature and is defined as:

$$R = \frac{h_L}{2} + \frac{r^2}{2h_L} \qquad \text{(eq.3.2)}$$

where h_L is the height and r is the radius of the microlens.

For the microlenses obtained by printing five drops of the 2.3:1 TOL:NMP mixture the focal property was equal to 1.76 mm resulting in agreement with the value subsequently measured with the interferometric system [19].

In order to have a clear interpretation of optical test results, it is usually convenient to express wavefront data in polynomial form. Zernike polynomials are often used for this purpose since this component terms have the same form as the types of aberrations usually observed in optical tests. In Figure 3.11 are shown the tilted interferometric fringes image and the wavefront error analysis in terms of the Zernike polynomial without the first four terms of the polynomial series for this structure under investigation. The root-mean-square (RMS) wavefront error, which gives information on the area over which the wavefront error is occurring, and the peak-to-valley (P-V) wavefront aberration, namely the maximum departure of the actual wavefront from the desired wavefront in both positive and negative directions, were estimated equal to 1/5.08 waves and to 1/1.27 waves, respectively. These results indicate that the central region of the analyzed structure has spherical symmetry with low aberrations. Moreover, the lateral region of the structure having toroidal shape also contributes to the light focusing effect but in less significant way with respect to the central structure. Therefore, the interferometric analysis indicated that the manufactured convex-shaped structures can be employed as good optical quality microlenses with negligible defects.

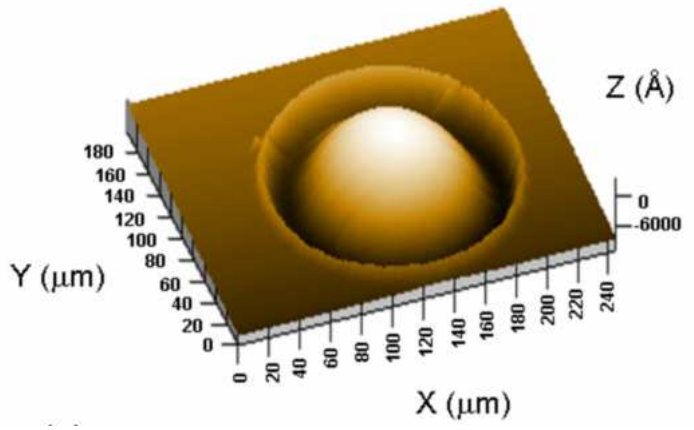

Figure 3.10 3-D profile of the microlens obtained printing five drops of the 2.3:1 TOL:NMP mixture.

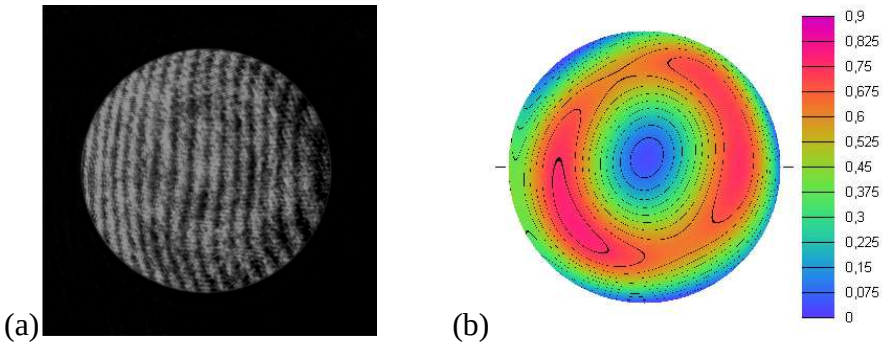

Figure 3.11 (a) tilted interferometric fringes image and (b) wavefront error (@ λ= 550 nm) of the microlens obtained printing five drops of the 2.3:1 TOL:NMP mixture.

3.3 Applications of polymer microstructures to optoelectronic devices

The concave- and convex-shaped microstructures were manufactured and characterized for different optical applications, mainly focused on the improvement of the OLED device efficiency. The application for each realized microstructure will be detailed in the following paragraphs.

3.3.1 PI structured by NMP in mould applications

The structured PI layer was employed as a template for another polymer which models itself acquiring a complementary shape. The employed polymer solution was commercial Sylgard 184 Silicone Elastomer (Dow Corning, USA) mixed with a curing agent and, after being placed into vacuum chamber for removing the bubbles, spin-coated on the microstructured PI layer at 5000 rpm for 60 sec performing a thickness of about 1 μm. Successively, after a curing process at 100 °C for 45 min, the elastomeric silicone polymer was removed from the PI mould resulting with a convex-shaped structuring on top of its surface, that is the complementary form with respect to the profile of Figure 3.1.

3.3.2 PS structured by TOL as textured substrates in OLED applications

The PS structuring with the profile shown in Figure 3.5 was employed as texturing of the substrate of an OLED (organic light-emitting diodes) device. A detailed study was developed demonstrating that this kind of structuring performed on a polymeric underlayer of a bottom-emitting OLED device allows to destroy the interference effects generated by OLED resonator cavity [20]. In the following paragraph a brief introduction on OLEDs and on the interference effects generated in the emission spectrum was performed.

3.3.2.1 OLEDs: introduction and improvements

OLEDs are attractive for fabricating high quality, electroluminescent large area displays and because of the potential low cost [21]. The conventional OLED structures can differ by the architectures opportunely developed to enhance optoelectronic device performances, lowering the electrical and optical threshold voltages, improving the device efficiency and increasing the lifetime [22]. For

whatever architecture, OLEDs can be classified in two categories, bottom emitting (BE) and top emitting (TE) [23], and in both these devices the light generated in the emissive layer propagates through the device layers, and is emitted outside. Anyway, more than half of the generated light is trapped and finally wasted inside the stack due to the total internal reflections at the interfaces between layers with different refractive-index [24]. Since the thickness of some layers of the device can be of the same order of magnitude of the wavelength of optical radiation, interference phenomena take place. These phenomena that produce an alteration of the emission spectrum can be attributed to microcavity effects generated by the device that acts as optical cavity [23,25]. In some encapsulated structures, the interference effects occur due to the air gap between the device and the cover glass [26].

Another crucial factor that compromises OLED luminance efficiency is the surface roughness of anode contact, leading to the formation of dark spots, degradation, and hence to failure of the device working. Many efforts have been made to improve OLED performances modifying the anodic layer surface through chemical and physical treatments [27], or introducing a polymer layer directly under the electrode [28]. As concerning this last approach, the right choice of the polymer material to realize the under-layer allows of optimizing the visible light transmittance, matching the refractive indices of adjacent layers, and enhancing the device stability [28,29].

In this thesis work, BE OLED devices fabricated onto a polymer layer spin-coated on glass substrate. The polymer film smoothes the anode surface reducing its roughness. Anyway, as the polymer under-layer is thin, interference effects take place modifying the OLED emission spectrum. In order to eliminate this phenomenon a method based on the structuring of polymer under-layer surface by means of the inkjet printing technology is proposed.

3.3.2.2 OLED device fabrication

The PS layer is introduced in OLED devices as under-layer in order to improve the roughness of the anodic electrode so enhancing the electroluminescence performances.

ZnO (zinc oxide) films were sputtered onto PS/glass system and, as comparison, directly on glass. The morphology of the conductive films were analyzed by an atomic force microscopy (AFM) (Veeco, Dimension Digital Instruments Nanoscope IV) and reported in Figure 3.12. The 3D-topography images and the related mean roughness values indicated that the polymer reduces the roughness degree of the oxide film deposited on it. Hence, the insertion of the PS layer improves the ZnO electrode morphological properties for OLED applications.

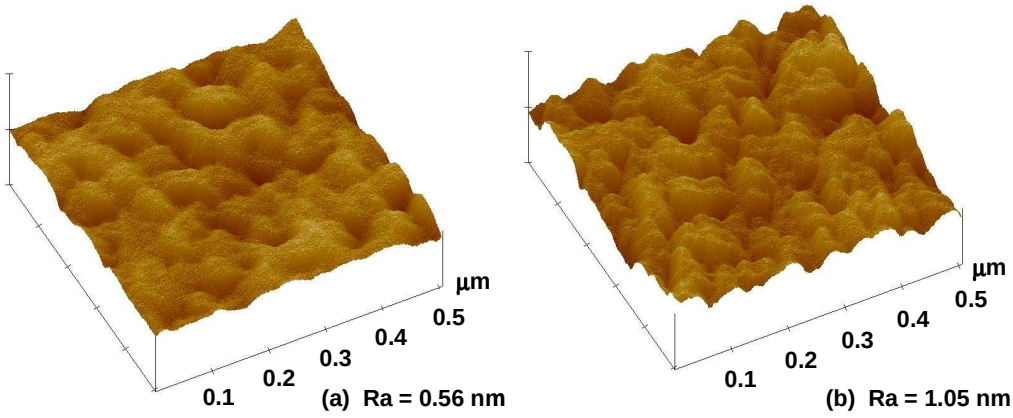

Figure 3.12 AFM images (scan size 0.5x0.5 µm2, z scale 10 nm) of ZnO films sputtered on PS/glass (a) and directly on glass (b). Ra is the average roughness value.

Successively, the double-layer OLED device with ZnO/NPD (N,N-Di-[(1-naphthalenyl)-N,N-diphenyl]-1,1-biphenyl-4,4-diamine)/Alq_3 (tris 8-hydroxyquinoline aluminium salt)/Al (aluminium) structure was manufactured on PS film. The ZnO anodic contact (240 nm, 26.9 Ω/square, n_{ZnO} = 1.89 @ λ = 500 nm) was deposited in a MRC643 system (4 mTorr, 2.2 W/cm^2) by RF sputtering (13.56 MHz) from a Al_2O_3 doped ZnO target in Ar-plasma atmosphere. NPD and Alq_3, 40 nm and 60 nm thick, respectively, were deposited by thermal evaporation without breaking vacuum conditions (10^{-7} mbar base pressure). The aluminium cathode (200 nm) was evaporated as a final layer. The active device area was 0.56 mm^2.

In Figure 3.13 is reported a schematic image of the device stack.

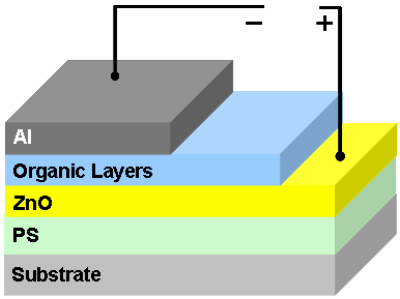

Figure 3.13 Schematic section of OLED stack manufactured on a polymeric under-layer.

3.3.2.3 Interference effects in an optical cavity

The electroluminescence (EL) spectra emitted by the realized OLED devices was detected employing a CCD-telescope to collect and send the light to a spectroradiometer through optical fibre (Optronics Laboratories OL770 system). These measurements were performed also at different angles by holding the OLED device on a goniometric system and placing it in front of the CCD. OLED emission spectra detected at different angles are shown in Figure 3.14.

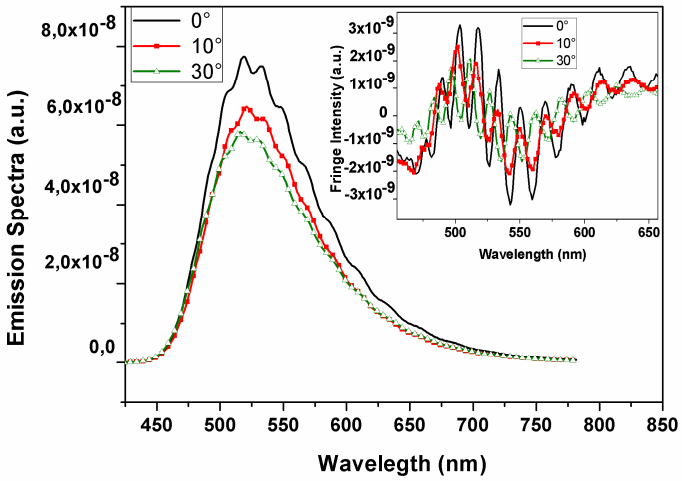

Figure 3.14 Emission spectra of OLED on the unstructured PS under-layer at different view angles. The inset curves are obtained subtracting the spectra interpolation to detected EL profiles.

Interference effects occur at different wavelengths for each investigated angle and can give many information about the PS layer and the properties of the light source.

This phenomenon is due to the thickness of PS layer that in this case can be considered as a Fabry-Pérot cavity. Indeed, from the interference minima or maxima positions detected in the emission spectrum it is possible to infer the layer thickness through the following relation [26,30]:

$$d = \frac{\lambda_1 \lambda_2}{2 n_{PS} (\lambda_2 - \lambda_1)} \qquad \text{(eq.3.3)}$$

where λ_1 and λ_2 are the shorter and longer wavelengths corresponded to two contiguous maxima or minima of the interference spectrum and n_{PS} = 1.58 is PS refractive index. The calculated thickness value was 5.5 ± 0.3 μm, comparable to the measured value of 5.3 μm.

As the spectral profile of OLED source is approximately Gaussian with FWHM (full width at half maximum) of about 100 nm, the observed interference effects have been analyzed in the space-frequency domain according to the following law [30]

$$S(\upsilon) \propto S_0(\nu)\left[1 + |\mu| \cos(\beta \Delta r)\right] \qquad \text{(eq.3.4)}$$

where $S_0(\nu)$ is the source emission spectrum. The second term of the equation 3.2 is the interference contribution to the spectral profile where $|\mu|$ is the modulus of the spectral degree of coherence and represents the interference efficiency of the spectral interference. Moreover, $0 \leq |\mu| \leq 1$, also known as visibility of spectral interference, is related to the coherence length and to the optical path difference (OPD) of the waves that interfere. Finally,

$$\beta \Delta r = \frac{\nu \Delta r}{L_c \Delta \nu} \qquad \text{(eq.3.5)}$$

where $\Delta r = 2 n_{PS} d \cos\theta_{\text{int}\,ernal}$ represents OPD of a Fabry-Pérot cavity, $\theta_{internal}$ is related to experimental view angle through Snell's law, and

$$L_c = \frac{2\ln 2\bar{\lambda}^2}{\pi n_{ps}\Delta\lambda} \qquad \text{(eq.3.6)}$$

is the coherence length of a light source. In the examined case, the emission peak wavelength ($\bar{\lambda}$) is centered at 525 nm with $\Delta\lambda = 100nm$ and L_c results equal to 0.77 μm. By using the parameters that characterizes the realized Fabry-Pérot cavity, the theoretical calculations give $|\mu|$ ~ 0.1. This low value of $|\mu|$ explains the reduced visibility of the interference effect in spectral profile of the OLED source.

The interference effect was more evident in the configuration with the device placed in front of the detector with respect to the other angular positions as pointed out by the emission profiles showed in the inset of Figure 3.14 and obtained subtracting the interpolation of EL profile to the detected spectrum for each view angle. As the detection angle increases, OPD decreases and the fringes broaden and their intensity reduces.

Anyhow, the interference effect still visible at 30° was observed also at higher angles depending on the particular realized Fabry-Perot cavity, and, hence, on the structure geometry and on the materials optical properties.

All the reported results show that the PS under-layer has good optical properties in visible range, reduces the roughness degree of the anodic electrode deposited on it, nevertheless introduces an interference phenomenon, modifying the OLED emission spectrum. A structuring of PS was used in order to solve this phenomenon.

For this reason, a square array of microcavities was fabricated by printing TOL multiple drops on the PS film and than the OLED device was fabricated on the top of structured PS layer. The related schematic section and optical micrograph are reported in Figure 3.15.

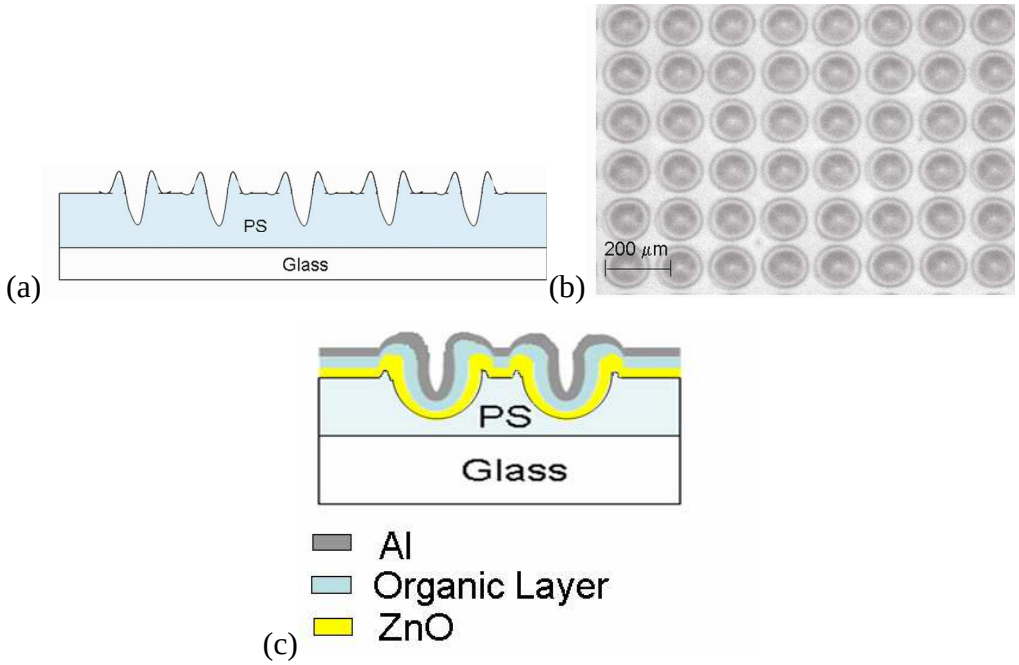

Figure 3.15 (a) Schematic section and (b) optical micrograph of a PS microcavities array. (c) Schematic section of OLED stack manufactured on structured polymer underlayer

The structured OLED emission spectra at different view angles are shown in Figure 3.16.

The emission profile clearly exhibits a strongly reduced, almost absent interference effect upon the under-layer structuring. This can be attributed to the locally reduced thickness of the textured polymer layer and to the interface shape that randomizes the lightpath. The inset of Figure 3.16 points out that only a slight interference effect is still visible in the structured OLED EL profile due to the presence of untextured areas of PS layer. Indeed, the distance between two contiguous cavities of the array is about 10 μm.

The polymer structuring allows to ensure the morphological benefits of the anodic contact that retains a local low roughness and, at the same time, to assure that the emitted spectrum is only function of the emitting source and is not affected by the presence of the polymer under-layer.

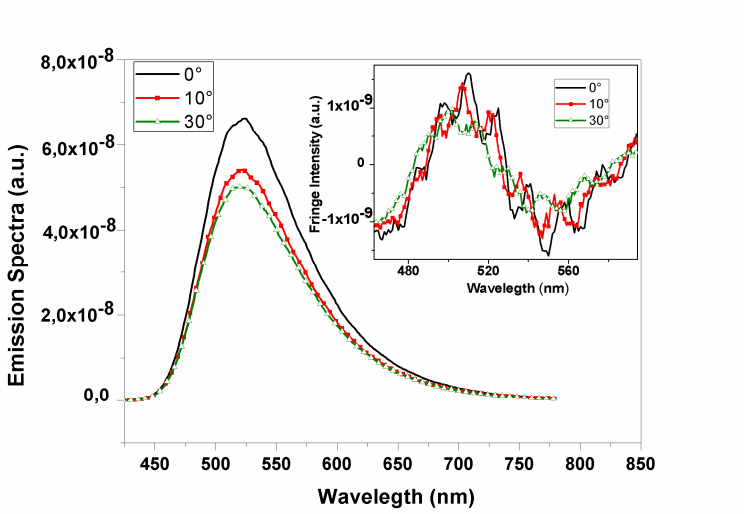

Figure 3.16 Structured OLED emission spectra for different detection angles. The measured EL profile minus the spectrum interpolation is detailed in the inset for each angle.

3.3.3 PS structured by TOL:NMP as microlenses OLED applications

The convex-shaped microstructures manufactured with the TOL:NMP-PS system can be used as microlenses in order to reduce the electroluminescence (EL) radiation losses due to the total internal reflection in an OLED device.

To cover the entire area of the OLED device, a square array of microlenses was fabricated with a 5x5 mm^2 surface by printing one, three and five drops of the 2.3:1 TOL:NMP on the PS layer. In Figure 3.17 the schematic section and the optical micrograph of the PS microlens array are illustrated.

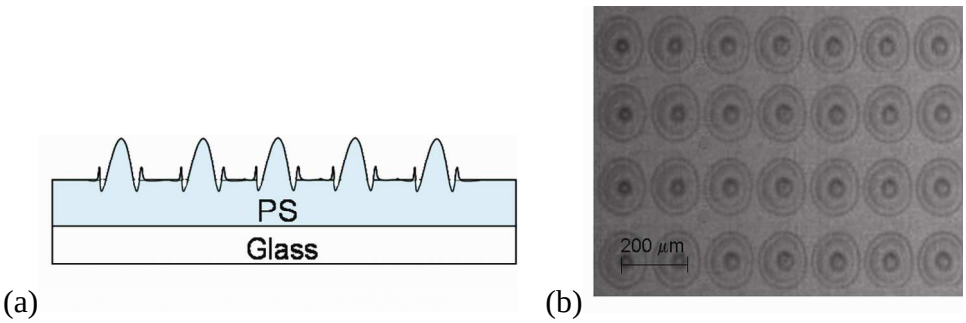

(a) (b)

Figure 3.17 Schematic section (a) and optical micrograph (b) of a PS microlens array.

In Figure 3.18a is illustrated the schematic section of the OLED stack coupled to the microlens array which was fabricated on the opposite side of the substrate. The current-tension characteristic illustrated in Figure 3.18b was the typical electrical response measured for all the manufactured devices, both coupled and not coupled to microlenses. The OLEDs showed good electrical performances (V_{ON} ~ 3 V) and good detected reproducibility which was crucial to study the functioning of the microlenses and to compare the efficiencies of the different arrays. To this end, in Figure 3.19 are reported the curves of the photodiode current as function of the electrical current for the OLEDs coupled to different microlens arrays and, as comparison, for the unlensed OLED, namely the device manufactured with the same stack and with an unstructured PS layer on the opposite side of the substrate. The results pointed out that the OLED electroluminescence efficiency was enhanced by applying the microlenses. In detail, by tuning the number of drops the curvature radius of the microlenses was controlled and so also their focal length. By coupling these lens systems to the OLED, the device efficiency was improved by a factor ranging from 2.2 % to 5 %. The lenses manufactured by five drops provided the highest EL efficiency, nevertheless this enhance was weak with respect to the efficiency detected for the device without lenses due to the lens geometry, i.e. the ratio between the microstructure height and its diameter as low as 1.62 %, that means long focal length. However, although the maximum obtained electroluminescence efficiency enhance was not significantly high, it is worth noting the trend of the increase of the EL efficiency as the ratio between the height (of the central peak) and the diameter (at the bottom) increases.

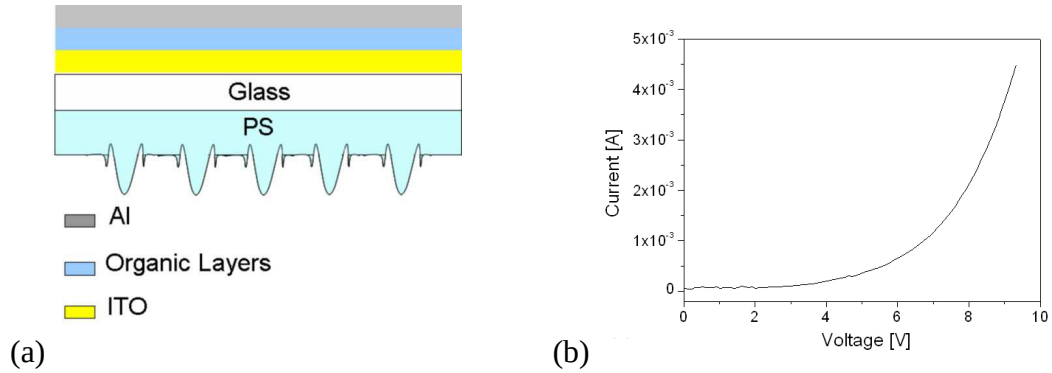

Figure 3.18 (a) Schematic section of the OLED stack coupled to the microlens array and (b) typical I-V curve of all the manufactured devices.

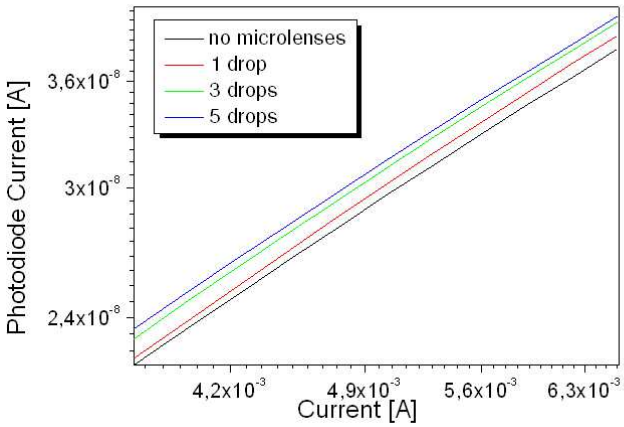

Figure 3.19 Photodiode current vs. electrical current for OLEDs coupled to arrays of microlenses manufactured by printing 1, 3 and 5 drops of the 2.3:1 TOL:NMP mixture and, as comparison, for the unlensed OLED.

In addition, the normalized EL intensity of 5-drops lensed device driven at I = 1 mA at different viewing angles was measured and compared to that one of the unlensed device. As depicted in Figure 3.20, the measured emission from the unlensed device matched very well with the calculated Lambertian pattern. The angular-dependent EL intensity of the device with the microlens array showed a similar behaviour with an enhanced luminance at low viewing angles.

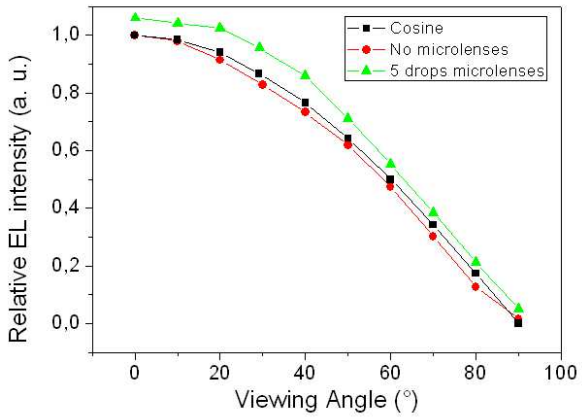

Figure 3.20 Relative EL intensities at different viewing angles for lensed and unlensed devices and, as comparison, calculated Lambertian pattern curve.

3.4 Microlens fabrication via additive method

The previously described technique (IJE) provide a method for fabricating polymer microstructures that were employed as microlenses in OLED devices. Anyway, this technique doesn't allow to significantly vary the ratio between the height and the diameter of the microstructures. Therefore, another approach based on the additive deposition of optical grade polymer materials was followed in order to realize refractive microlenses which can be more efficiently applied in several application fields such as communications, display systems, imaging sensors, photodetectors. Therefore, many methods have been developed to fabricate these optical components. Traditional fabrication techniques use photolithography [31], resist processing [32], reactive ion etching [33], laser irradiation [34] while other, more recent techniques are based on microjet printing [35], direct laser [36] or e-beam writing [37], laser ablation [38], photopolymerization [39]. All these methods produce optical quality microlenses, namely characterized by low aberration and good uniformity of the focal length. However, only some of these techniques are suitable for rapid prototyping of microlenses with variable focal length, generally those ones that don't need to employ masks, resulting less complex and short time-consuming processes which, hence, allow to reduce the production costs.

The inkjet printing is one of the techniques that satisfy these requirements; moreover, it offers also other advantages such as the versatility in definition of the patterns and in the employable substrates and the potentiality to be introduced in roll-to-roll processes. The employment of the IJP technology to fabricate optical elements was essentially promoted by the development of optical grade polymers with suitable thermal and mechanical properties [19,40]. On the other hand, the right combination of using these materials with a low-cost technology was further supported for manufacturing less expensive and more lightweight components.

Among the most commonly used polymers for the fabrication of optical components, poly(methyl methacrylate) (PMMA) is an optical grade polymer with good mechanical and thermal properties. In particular, this polymer was employed to manufacture microlenses through printing methods [41,42], nevertheless no systematic study is reported about the effects of the chemico-physical properties of

the PMMA based ink on the shape of the inkjet printed microlens and so on its optical and physical properties.

Microlenses by inkjet printing PMMA solutions prepared with different solvents (toluene -TOL-, N-Methyl-2-pyrrolidone -NMP-, chlorobenzene -CB-, ortho-dichlorobenzene -o-DCB-) and with different solvent mixtures (NMP:TOL, CB:NMP, CB:o-DCB, o-DCB:TOL, NMP:o-DCB) on glass substrates covered by a transparent, hydrophobic tetraethylorthosilicate/1H,1H,2H,2H-Perfluorodecyltriethoxysilane (TEOS/PFTEOS) film were fabricated. The effects of both the solvent mixing ratios and the polymer concentration on the profile and the geometry of the microstructures were investigated through profilometric and interferometric analyses by means of a Mach-Zehnder system in confocal configuration evaluating the wave aberrations as already described in the previous paragraphs [18,43].

3.4.1 Microlens fabrication

Commercial glass purchased from Schott was employed as substrate and cleaned with a standard procedure applying in sequence the sonication with deionised water, acetone and isopropanol, drying with nitrogen flow and finally in oven at 130 °C for 1 h.

In order to prepare a hydrophobic surface on which the microstructures will be successively fabricated, a TEOS/PFTEOS film was deposited on glass substrate. A sol-gel solution was prepared by mixing TEOS, PFTEOS, ethanol, deionized water and concentrated hydrochloric acid (HCl). Before the deposition, the solution was diluted with fluoropropanol and then filtered. The fluoropropanol was added to enhance the wetting of the solution-substrate system so improving the adhesion.

The prepared solution was spin-coated (1000 rpm for 30 s) by means of a Brewer Science Model 100 spin coater, followed by 30 min hot-plate bake at 100 °C to remove the residual solvent and gradually heated from 110 °C to 150 °C for the thermal curing. The film was kept at 150 °C for one night and the thickness was 280 nm.

Successively, the polymeric inks were prepared by dissolving 5 mg/mL of PMMA in different solvents, such as TOL, NMP, CB and DCB, and in different solvent mixtures, such as NMP:TOL, CB:NMP, CB:DCB, DCB:TOL and NMP:DCB. All the solvent mixture systems were investigated at volume mixing ratios of 20:80 and 80:20. Additionally, solutions of PMMA (40 mg/mL) in pure NMP and NMP:TOL mixture (80:20) were also investigated. All the chosen solvents are suitable to dissolve the polymer and have right volatility and surface tension properties for inkjet printing processing (TOL: T_b = 110.6 °C, γ = 28.53 mN/m; NMP: T_b = 202 °C, γ = 40 mN/m; CB: T_b = 132 °C, γ = 33.6 mN/m; DCB: T_b = 180 °C, γ = 26.84 mN/m).

Polymeric microstructures were fabricated by printing single drops of the PMMA based inks on the hydrophobic surface of the TEOS/PFTEOS film in order to freeze the drop on the substrate so minimizing the spreading.

The droplet depositions were performed by using Microdrop printhead with 30 μm opening nozzle corresponding to 20 pL droplet volume. During the printing process, the substrate temperature was kept at 17 °C by means of a Peltier cell and monitored by a thermocouple. The prints were carried out at 110 Hz drop emission frequency and 10 mm/s printhead speed.

After printing, the PMMA microstructures were left at 17 °C for 30 min for completing the polymer drying.

A surface profilometer (KLA Tencor P-10 Surface Profiler) was used to detect the profile and the geometry of the manufactured microstructures while a Mach-Zehnder interferometer was employed to evaluate the wave aberrations [44].

3.4.2 Microlens characterization

The profiles of the PMMA microstructures realized by employing five different solvent mixtures, each one with two mixing ratios (20:80 and 80:20), are shown in Figure 3.21 and compared with those obtained by the pure component solvents.

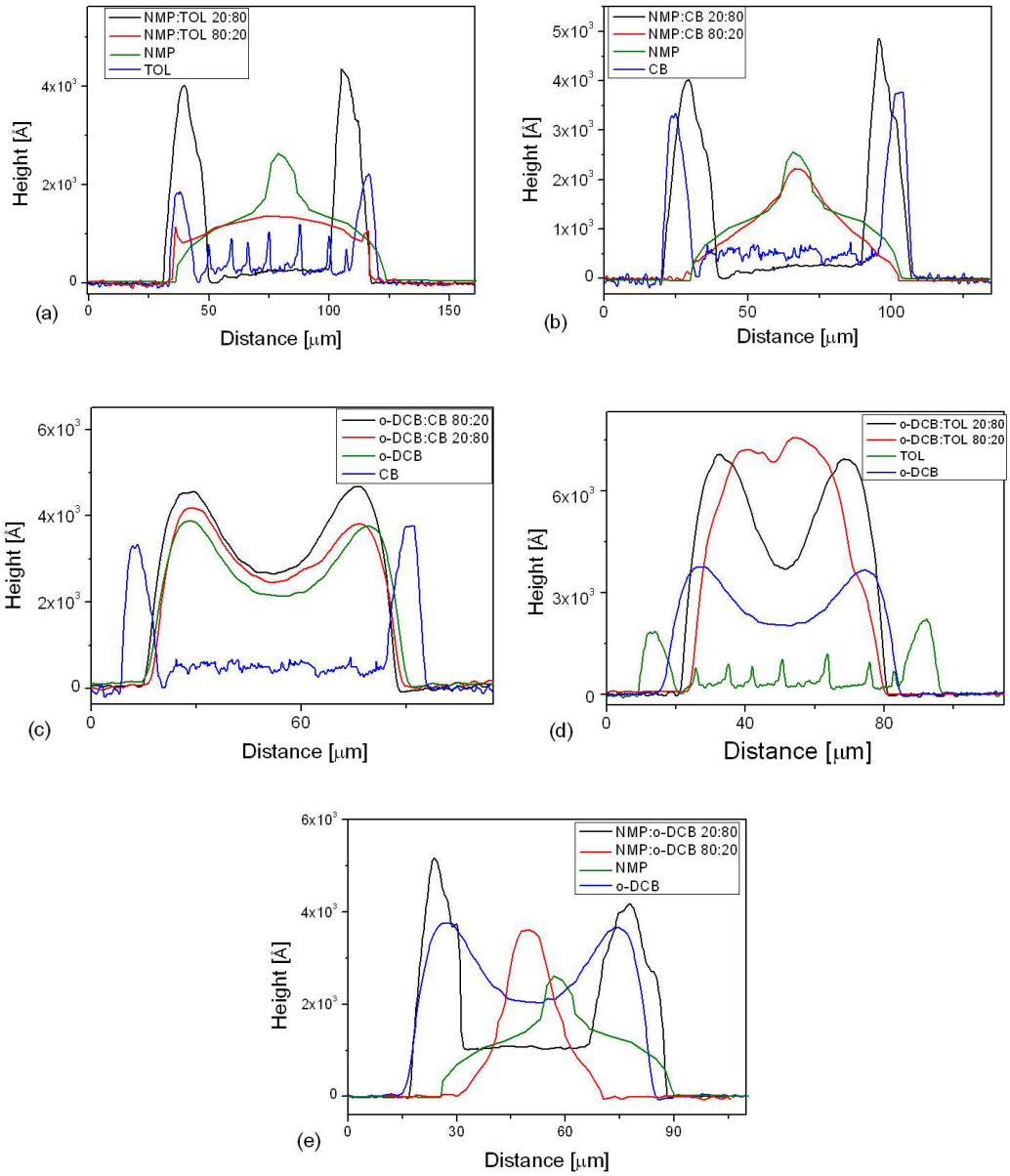

Figure 3.21 Two-dimensional profiles of the PMMA microstructures employing different mixtures (volume mixing ratios 20:80 and 80:20) in comparison with those obtained by the pure component solvents: (a) NMP:TOL, (b) NMP:CB, (c) o-DCB:CB, (d) o-DCB:TOL and (e) NMP:o-DCB (5 mg/mL concentration).

The profilometric analysis of the structures obtained by the different inks shows that the chemico-physical ink parameters, such as boiling point and surface tension, have a key role in the definition of the microstructure shape. For the ink dissolved in NMP, high-boiling point solvent with high surface tension, the Marangoni flow from the edge towards the center of the sessile drop is dominant so inducing a solute pile in the center (Figure 3.21a,b,e). Indeed, the slow evaporation of the solvent is useful

so that the Marangoni flow diffuses from regions with low surface tension to regions with high surface tension, these last ones located around the top center of the droplet. For all the other investigated solvents with lower boiling point and lower surface tension lower than those ones of NMP, the drying process is mainly ruled by the flow of the “coffee-stain effect” and the final profiles are characterized by a flat central portion and two lateral humps. In particular, DCB, higher-boiling point solvent than TOL and CB, induces a partial inward flow. Indeed, for DCB the ratio between the lateral hump height and the flat central portion height is lower if compared with those of TOL and CB.

By employing the solvent mixtures, at the end of the drying process the PMMA microstructure profile is similar to that induced by the component solvent which is present in the mixture with higher concentration. By examining case by case, the DCB:CB mixture in both the volume mixing ratios 80:20 and 20:80 (Figure 3.21c) doesn’t modify the profile obtained by DCB in significant manner being the chemico-physical properties of the component solvents almost similar. For the DCB:TOL mixture with 80:20 mixing ratio (Figure 3.21d), the microstructure profile shows a larger accumulation at the centre with respect the profiles by pure DCB and pure TOL. This behaviour is expected since the component solvent with higher boiling-point (o-DCB) with respect to the solvent with lower boiling-point (TOL) has also got a lower surface tension than the other one, so inducing an inward flow. Finally, by analyzing the NMP:TOL, NMP:CB and NMP:o-DCB mixtures at 80:20 mixing ratio (Figure 3.21a,b,e), the presence of the solvent with lower boiling point in comparison NMP lightly enhances the outward flow due to “coffee-stain effect” making the central pile, which is evident in the profile generated by NMP, less pronounced.

This analysis showed that the solvent in which the polymer is dissolved allows to control the microstructure profile. In particular, among all the investigated solvent systems both the pure NMP solvent and the NMP:TOL mixture (80:20) are the most suitable to perform convex-shaped microstructures to be employed as optical components.

In order to investigate if it is possible to improve the spherical symmetry of the structures, the effect of the ink viscosity on the microstructure shape was studied.

The attention was focused on the solutions obtained dissolving PMMA in pure NMP and in NMP:TOL mixture (80:20) and prepared the inks by increasing the polymer concentration from 5 mg/mL to 40 mg/mL. The 2-dimensional profiles of the microstructures obtained by printing the single drop for both these inks are shown in Figure 3.22. By comparing these results with the profiles of the same inks prepared at lower PMMA concentration (Figure 3.21b,c), it appears that the higher concentration improves the spherical shape of the microstructures for both the investigated systems. Moreover, the effect of the ink viscosity on the microstructure profile is more significant than the volume mixing ratio so resulting a fundamental parameter to manufacture structures that have to be employed as microlenses.

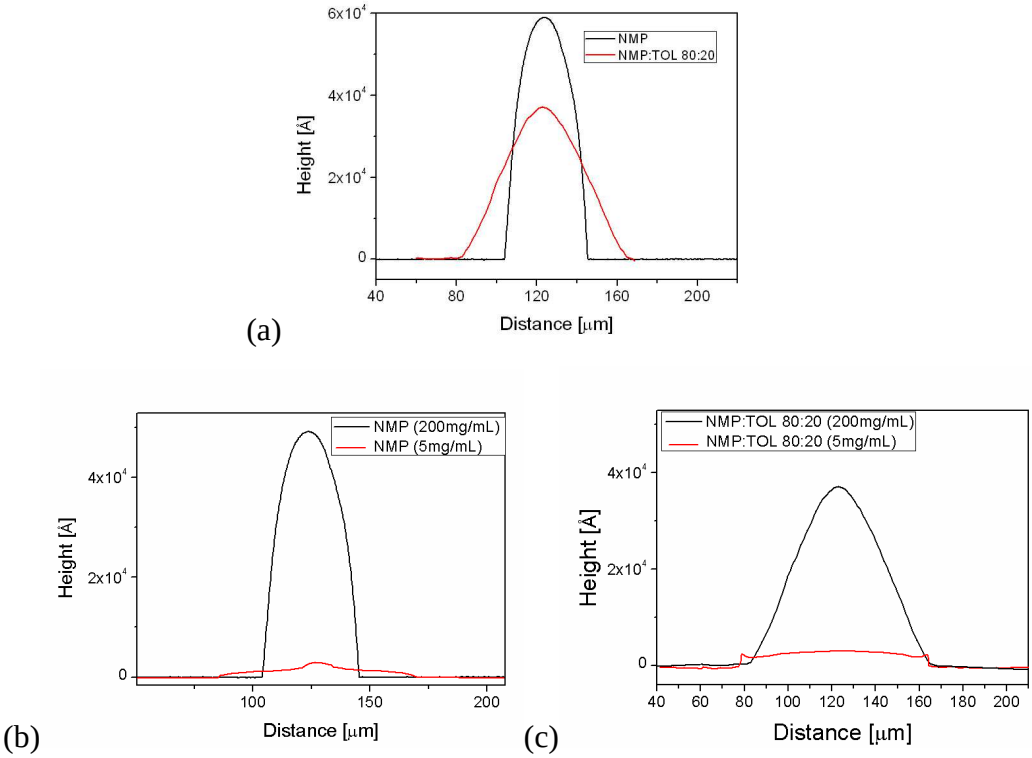

Figure 3.22 Two-dimensional profiles obtained by printing PMMA dissolved in pure NMP and NMP:TOL mixture (80:20) (40 mg/mL concentration) (a), pure NMP at 50 and 200mg/mL (b) and NMP:TOL 80:20 at 50 and 200 mg/mL(c).

By profilometric analysis of the microlenses manufactured at higher concentration, the geometrical parameters, namely diameter and height were evaluated, and the focal length was calculated[19]. The focal lengths were extimated equal to 82 μm and 442 μm for pure NMP and NMP:TOL mixture, respectively.

These microstructures were also analyzed by means of a Mach-Zehnder system in confocal configuration as described in 3.2.3.1 section. The results of the interferometric analysis are reported in Figure 3.23 for pure NMP and in Figure 3.24 for NMP:TOL mixture.

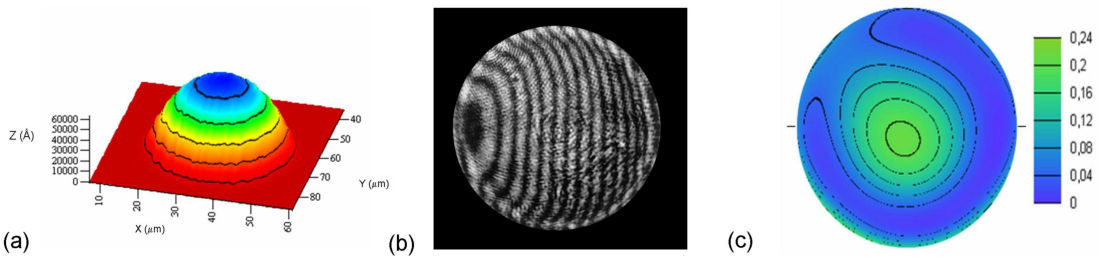

Figure 3.23 (a) 3-D image, (b) tilted interferometric fringes image and (c) wavefront error of the microlens by printing PMMA dissolved in pure NMP (40 mg/mL concentration).

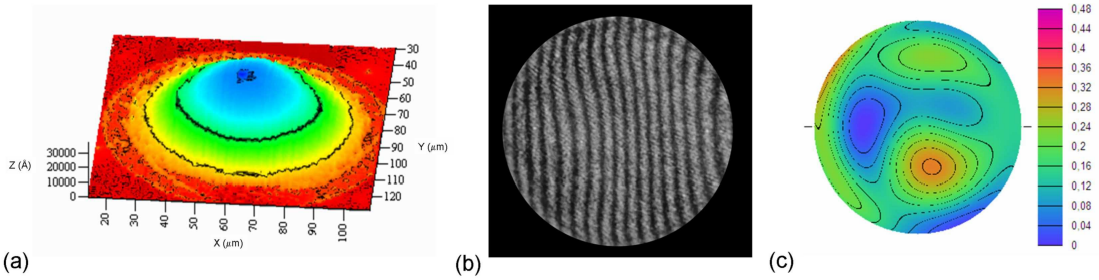

Figure 3.24 (a) 3-D image, (b) tilted interferometric fringes image and (c) wavefront error of the microlens by printing PMMA dissolved in NMP:TOL mixture (80:20) (40 mg/mL concentration).

These figures illustrate the 3-D profiles (Figure 3.23a, Figure 3.24a), tilted interferometric fringes images (Figure 3.23b, Figure 3.24b) and the wavefront error analysis in terms of the Zernike polynomial without the first four terms of the polynomial series (Figure 3.23c, Figure 3.24c). As previously explained, Zernike polynomials are used to describe the aberrations of lenses with respect to an ideal spherical shape in terms of RMS wavefront error and peak-to-valley (P-V) wavefront aberration [44]. For microlens by pure NMP, the RMS wavefront error was 1/5.18 waves and peak-to-valley (P-V) wavefront aberration resulted 1/4.55 waves. For microlens by NMP:TOL mixture (80:20), the RMS wavefront error was 1/15.1 waves and peak-to-valley (P-V) wavefront aberration was 1/3.011 waves. These results obtained for the microstructure by pure NMP show high optical quality.

Finally, the focal lengths measured through the interferometric system are in agreement with the estimated ones by the profilometric analysis.

3.5 Summary

In the chapter of this thesis the feasibility to employ the inkjet etching to perform polymer microstructures and the additive printing for the realization of microlenses was investigated.

Concerning the polymer microstructuring, concave and convex profiles can be obtained by using pure solvent and solvents mixtures with suitable mixing ratios, respectively. The geometrical parameters of the structures can also be modified by changing the substrate temperature and/or the number of the printed droplets. Profilometric and interferometric analyses were performed on these structures evaluating the geometrical and optical parameters.

Moreover, some applications of these polymer microstructures by IJE were described.

As example, the structured PI layer was employed as mould for another polymer which models itself acquiring a complementary shape.

A cavity-shaped microstructure array realized by printing pure solvent (TOL) on a PS layer was used to drastically reduce the interference effects in the electroluminescent spectrum profile in a bottom emitting OLED. This devices were fabricated onto a polymer layer which smoothes the anode surface so reducing its roughness. Anyway, as the polymer under-layer is thin, it acts like Fabry-Pérot cavity producing interference effects. The microcavities array manufactured on the polymer surface modifies the incidence angle of the light radiation at anode/polymer interface locally changing the polymer thickness so destroying the resonator effect of the optical cavity.

By printing single and multiple droplets of the TOL:NMP mixture at an optimized volume mixing ratio on the PS layer, convex-shaped structures with spherical symmetry were realized. Through the interferometric analysis the aberrations of these structures with respect to an ideal spherical shape were evaluated proving that the manufactured microstructures can work as refractive optical components. Additionally, by coupling an array of these microstructures to an OLED device, their

functioning as microlenses was specifically investigated. It was observed an increase of the electroluminescence efficiency of the lensed devices as the focal length decreased, up to a maximum of 5 % with respect to the unlensed device. Moreover, the analysis of the angular-dependent EL intensity showed that the devices with and without lenses had a Lambertian behavior with an increased light focalizing effect by the lensed device at low viewing angles.

The last part of this chapter was focused on the realization and characterization of microlenses obtained by means additive printing of PMMA droplet on a hydrophobic substrate. The microstructure profile was controlled by employing pure solvents and solvent mixtures with different mixing ratios. The influence of the chemico-physical parameters of the ink, such as boiling point and surface tension, on the structure shape was investigated as responsible parameters of more or less significant “coffee-stain effect” with respect to the Marangoni effect. Moreover, the effect of the polymer viscosity on the microstructure profile was studied: the results showed that the ink prepared with higher concentration of the polymer improves the spherical shape of the microstructures for both the pure solvent and solvent mixture systems. Additionally, the interferometric analysis allowed to evaluate the aberrations of the realized microlenses with respect to an ideal spherical shape and the results demonstrated that the right choice of the solvent and the polymer concentration in preparing the ink lead to high optical quality microlenses.

Bibliography

[1] S. Bouaidat, C. Berendsen, P. Thomsen, S.G. Petersen, A. Wolff, J. Jonsmann, Micro patterning of cell and protein non-adhesive plasma polymerized coatings for biochip applications, Lab Chip. 4 (2004) 632.

[2] J. Hyun, H. Ma, Z. Zhang, T.P. Beebe Jr., A. Chilkoti, Universal Route to Cell Micropatterning Using an Amphiphilic Comb Polymer, Advanced Materials. 15 (2003) 576-579.

[3] Y. Xia, R.H. Friend, Nonlithographic patterning through inkjet printing via holes, Appl. Phys. Lett. 90 (2007) 253513.

[4] C.Y. Chang, S.Y. Yang, J.L. Sheh, A roller embossing process for rapid fabrication of microlens arrays on glass substrates, Microsyst Technol. 12 (2006) 754-759.

[5] R. Pericet-Camara, A. Best, S.K. Nett, J.S. Gutmann, E. Bonaccurso, Arrays of microlenses with variable focal lengths fabricated by restructuring polymer surfaces with an ink-jet device, Opt Express. 15 (2007) 9877-9882.

[6] R. Kapur, B.J. Spargo, M. Chen, J.M. Calvert, A.S. Rudolph, Fabrication and selective surface modification of 3□dimensionally textured biomedical polymers from etched silicon substrates, Journal of Biomedical Materials Research. 33 (1996) 205-216.

[7] W.-K. Huang, W.-S. Wang, H.-C. Kan, F.-C. Chen, Enhanced Light Out-Coupling Efficiency of Organic Light-Emitting Diodes with Self-Organized Microlens Arrays, Jpn. J. Appl. Phys. 45 (2006) L1100-L1102.

[8] A.J. Lennon, A.W.Y. Ho-Baillie, S.R. Wenham, Direct patterned etching of silicon dioxide and silicon nitride dielectric layers by inkjet printing, Solar Energy Materials and Solar Cells. 93 (2009) 1865-1874.

[9] R.D. Deegan, O. Bakajin, T.F. Dupont, G. Huber, S.R. Nagel, T.A. Witten, Capillary flow as the cause of ring stains from dried liquid drops, Nature. 389 (1997) 827-829.

[10] R.D. Deegan, Pattern formation in drying drops, Phys. Rev. E. 61 (2000) 475.

[11] R.D. Deegan, O. Bakajin, T.F. Dupont, G. Huber, S.R. Nagel, T.A. Witten, Contact line deposits in an evaporating drop, Phys. Rev. E. 62 (2000) 756.

[12] B.-J. de Gans, S. Hoeppener, U.S. Schubert, Polymer relief microstructures by inkjet etching, J. Mater. Chem. 17 (2007) 3045.

[13] B. J de Gans, S. Hoeppener, U.S. Schubert, Polymer-Relief Microstructures by Inkjet Etching, Advanced Materials. 18 (2006) 910-914.

[14] T. Kawase, H. Sirringhaus, R.H. Friend, T. Shimoda, Inkjet Printed Via□Hole Interconnections and Resistors for All□Polymer Transistor Circuits, Advanced Materials. 13 (2001) 1601-1605.

[15] E. Bonaccurso, H.-J. Butt, B. Hankeln, B. Niesenhaus, K. Graf, Fabrication of microvessels and microlenses from polymers by solvent droplets, Appl. Phys. Lett. 86 (2005) 124101.

[16] E. Tekin, E. Holder, D. Kozodaev, U.S. Schubert, Controlled Pattern Formation of Poly[2-methoxy-5-(2′-ethylhexyloxyl)–1,4-phenylenevinylene]

(MEH–PPV) by Ink-Jet Printing, Advanced Functional Materials. 17 (2007) 277-284.
[17] H. Hu, R.G. Larson, Marangoni Effect Reverses Coffee-Ring Depositions, The Journal of Physical Chemistry B. 110 (2006) 7090-7094.
[18] T. Miyashita, Standardization for Microlenses and Microlens Arrays, Jpn. J. Appl. Phys. 46 (2007) 5391-5396.
[19] C.-T. Chen, C.-L. Chiu, Z.-F. Tseng, C.-T. Chuang, Dynamic evolvement and formation of refractive microlenses self-assembled from evaporative polyurethane droplets, Sensors and Actuators A: Physical. 147 (2008) 369-377.
[20] F. Villani, I.A. Grimaldi, G. Nenna, A.D.G. Del Mauro, F. Loffredo, C. Minarini, Study of the interference effects in an optical cavity for organic light-emitting diode applications, Opt. Lett. 35 (2010) 3333-3335.
[21] J.H. Burroughes, D.D.C. Bradley, A.R. Brown, R.N. Marks, K. Mackay, R.H. Friend, et al., Light-emitting diodes based on conjugated polymers, Nature. 347 (1990) 539-541.
[22] S.R. Forrest, The road to high efficiency organic light emitting devices, Organic Electronics. 4 (2003) 45-48.
[23] C.J. Lee, R.B. Pode, D.G. Moon, J.I. Han, N.H. Park, S.H. Baik, et al., On the problem of microcavity effects on the top emitting OLED with semitransparent metal cathode, Physica Status Solidi (a). 201 (2004) 1022-1028.
[24] Weixin Li, R.A. Jones, S.C. Allen, J.C. Heikenfeld, A.J. Steckl, Maximizing Alq/sub 3/ OLED internal and external efficiencies: charge balanced device structure and color conversion outcoupling lenses, Journal of Display Technology. 2 (2006) 143-152.
[25] V. Cimrová, D. Neher, Microcavity effects in single-layer light-emitting devices based on poly(p-phenylene vinylene), J. Appl. Phys. 79 (1996) 3299.
[26] D. Hill, K. Leo, G. He, Q. Huang, Analysis of spatial coherence of organic light-emitting devices through investigation of interference effects observed in top-emitting devices, Appl. Phys. Lett. 90 (2007) 101111.
[27] P. Vacca, M. Petrosino, A. Guerra, R. Chierchia, C. Minarini, D.D. Sala, et al., The Relation between the Electrical, Chemical, and Morphological Properties of Indium−Tin Oxide Layers and Double-Layer Light-Emitting Diode Performance, The Journal of Physical Chemistry C. 111 (2007) 17404-17408.
[28] H.-C. Hsieh, S.-C. Chang, Y.-M. Tsai, P-73: ITO Characteristics on Different Under-Layer for AM-OLED Displays, SID Symposium Digest. 34 (2003) 498-501.
[29] B.J. Chen, X.W. Sun, B.K. Tay, L. Ke, S.J. Chua, Improvement of efficiency and stability of polymer light-emitting devices by modifying indium tin oxide anode surface with ultrathin tetrahedral amorphous carbon film, Appl. Phys. Lett. 86 (2005) 063506.
[30] L. Mandel, E. Wolf, Optical Coherence and Quantum Optics, 1st ed., Cambridge University Press, 1995.
[31] D. Daly, R.F. Stevens, M.C. Hutley, N. Davies, The manufacture of microlenses by melting photoresist, Meas. Sci. Technol. 1 (1990) 759-766.
[32] Z.D. Popovic, R.A. Sprague, G.A.N. Connell, Technique for monolithic fabrication of microlens arrays, Appl. Opt. 27 (1988) 1281-1284.
[33] H.P. Herzig, Micro-Optics: Elements, Systems And Applications, 1st ed., CRC Press, 1997.

[34] M. Wakaki, Y. Komachi, G. Kanai, Microlenses and Microlens Arrays Formed on a Glass Plate by Use of a CO2 Laser, Appl. Opt. 37 (1998) 627-631.
[35] D.L. MacFarlane, V. Narayan, J.A. Tatum, W.R. Cox, T. Chen, D.J. Hayes, Microjet fabrication of microlens arrays, IEEE Photonics Technology Letters. 6 (1994) 1112-1114.
[36] M. He, X.-C. Yuan, N.Q. Ngo, J. Bu, S.H. Tao, Single-step fabrication of a microlens array in sol–gel material by direct laser writing and its application in optical coupling, J. Opt. A: Pure Appl. Opt. 6 (2004) 94-97.
[37] W. Cheong, L. Yuan, V. Koudriachov, W. Yu, High sensitive SiO2/TiO2 hybrid sol-gel material for fabrication of 3 dimensional continuous surface relief diffractive optical elements by electron-beam lithography, Opt. Express. 10 (2002) 586-590.
[38] F. Beinhorn, J. Ihlemann, K. Luther, J. Troe, Micro-lens arrays generated by UV laser irradiation of doped PMMA, Applied Physics A: Materials Science & Processing. 68 (1999) 709-713.
[39] C. Croutxé-Barghorn, O. Soppera, D.J. Lougnot, Fabrication of refractive microlens arrays by visible irradiation of acrylic monomers: influence of photonic parameters, Eur. Phys. J. AP. 13 (2001) 31-37.
[40] J.-P. Lu, W.-K. Huang, F.-C. Chen, Self-positioning microlens arrays prepared using ink-jet printing, Opt. Eng. 48 (2009) 073606.
[41] Y.S. Yang, D.-H. Youn, S.H. Kim, S.C. Lim, H.S. Shim, S.Y. Kang, et al., Preparation and Characteristics of PMMA Microlens Array for a BLU Application by An Inkjet Printing Method, Molecular Crystals and Liquid Crystals. 520 (2010) 239/[515]-244/[520].
[42] J.-hua Zhu, J.-xia Shi, Y. Wang, P.-sheng He, Spherical Micro-lens Array of PMMA Produced by Micro-molding, Chin. J. Chem. Phys. 19 (2006) 443-446.
[43] H. Ottevaere, B. Volckaerts, J. Lamprecht, J. Schwider, A. Hermanne, I. Veretennicoff, et al., Two-dimensional plastic microlens arrays by deep lithography with protons: fabrication and characterization, J. Opt. A: Pure Appl. Opt. 4 (2002) S22-S28.
[44] M.-S. Kim, T. Scharf, H.P. Herzig, Small-size microlens characterization by multiwavelength high-resolution interference microscopy, Opt. Express. 18 (2010) 14319-14329.

CHAPTER 4
ORGANIC FIELD EFFECT TRANSISTOR

Organic Field Effect Transistors (OFETs) based on solution processable semiconducting small molecules have obtained impressive improvements in their performances during recent years. These devices have been developed to realize low-cost, large-area electronic products. Indeed, the good solubility in common organic solvents opens the way to the fabrication of OFETs by direct printing methods, like the inkjet technology, which are able to guarantee many advantages including low costs, low material wastage, selective deposition of materials and non-contact patterning.

Recently, the research in the field of OFETs was focused on n-type semiconductors due to low air stability and limited processing capability of the organic materials reported in literature. To this purpose, the most promising n-channel candidates are the Cyanated Perylene Carboxylic Diimide derivatives which combine good solubility in organic solvents and good and stable electrical properties in ambient conditions.

In the present chapter, a study on the optimization of the methodology based on the employment of solvent mixtures suitably combined with the printing parameters for the inkjet deposition of N,N'-bis(n-octyl)-1,6-dicyanoperylene-3,4:9,10-bis(dicarboximide) (PDI-8CN_2), used as semiconductor in hybrid organic/inorganic OFET structure, is reported.

4.1 Introduction of OFETs

The transistor was probably the most important invention of the 20th Century and the story behind its invention is one of clashing egos and top secret research.

The transistor was invented in 1947 at Bell Telephone Laboratories by a team led by physicists John Bardeen, Walter Brattain and William Shockley. At first, few scientists saw in them the seeds of a technology that, in few decades, would come to permeate almost every sphere of human life. The transistors became the building block for all modern electronics and have been incorporated into cars, cellular telephones, display screens, computers and an ever expanding list of other applications.

The possibility to expand the research field to flexible substrates and to reduce the fabrication costs of this electronic component for its use in inexpensive applications has driven the scientific research towards the development of Organic Field Effect Transistors (OFETs). In these devices, organic semiconductors replace traditional inorganic semiconductors, such as amorphous silicon, in realizing the active channels. These materials can be solution processed by means of innovative techniques like spin-coating, spray-coating and inkjet printing. Furthermore, they require very low annealing temperatures (less than 150 °C) and can be processed in atmospheric conditions.

4.2 Current-voltage characteristics of OFETs

The first functional polymer OFET was first introduced by Tsumura 1986 [1]. This structure is particularly suitable to be used in combination with low conductivity materials and organic transistors belonged to the TFT family. In general, the main component of a TFT is a parallel plate capacitor, where a conducting electrode, the gate electrode (G), is electrically separated from the semiconducting layer by an insulating dielectric layer. Two other electrodes, source (S) and drain (D), are contacted to the semiconductor layer to provide the charge carrier injection.

In Figure 4.1, the three most common device configurations used in OFET are illustrated: bottom-gate bottom-contacts (BGBC), bottom-gate top-contacts (BGTC) and top-gate bottom-contacts (TGBC).

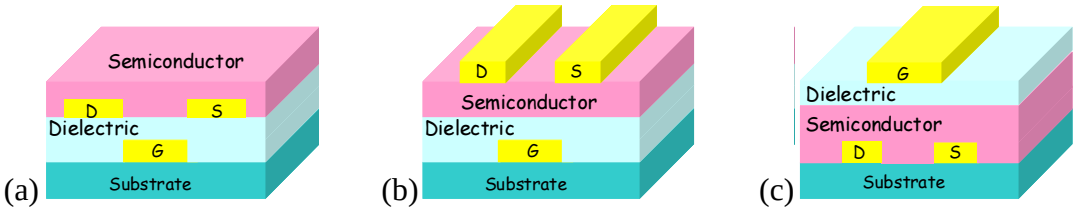

Figure 4.1 Common OFET configurations: bottom-gate bottom-contacts (a), bottom-gate top-contacts(b) and top-gate bottom-contacts (c).

By applying a positive gate voltage (V_{GS}), for n-type semiconductor, charge carriers are electrostatically accumulated in the semiconductor at the interface with insulating barrier. When the gate electrode is biased negatively the channel region is depleted of carriers and the semiconductor operates in the depletion mode. Due to this field-effect, the charge carrier density in the semiconductor can be modulated in reversible way. Hence, the resistivity of the semiconducting channel comprised between the source and drain is a function of V_{GS} . This means that the current I_{DS} through the semiconductor (upon application of a source-drain field V_{DS}) can be varied over many orders of magnitude [2]. Since the TFT can be switched between a conducting and a non-conducting state, it is widely used as the basic building block of binary logic circuits.

One of the most important physical parameter defining the quality of the OFET electrical response is the field-effect mobility, μ [2–6], which is the drift velocity of the charge carriers flowing through the semiconductor when a unit electric field is applied. This parameter strongly affects the operation speed of the transistor and has a fundamental importance when fast logic circuits are desired.

Two different and complementary methods are commonly employed to characterize the electrical response of TFTs: either V_{GS} is kept constant and V_{DS} is swept (output curves, Figure 4.2a) or V_{DS} is held constant and V_{GS} is swept (transfer characteristics, Figure 4.2b).

The electrical characteristic of a transistor can be divided into two regions: linear and saturation regime. The transistor is told to operate in linear regime when the

drain (V_{DS}) biases are much lower the gate (V_{DS}) voltages. Instead, the saturation regime takes place when V_{DS} becomes higher than V_{GS}. In the linear regime the current flowing between drain and source through the channel follows the Ohm's law being proportional to the drain and gate voltages. As the V_{DS} increases and approaches the gate voltage, V_{DG} drops to zero and the pinch-off of the channel occurs. At this point the I_{DS} becomes independent of the drain bias.

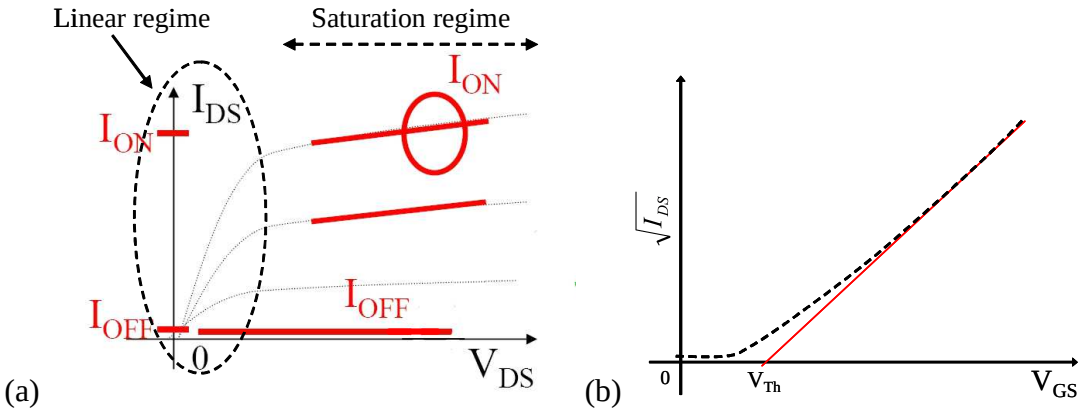

Figure 4.2 Plots of output curve (a) and transfer curve (b) for a n-type TFT.

Another important parameter is the threshold voltage (V_{Th}), defined as the gate voltage beyond which the conducting channel forms. A quasi-universal method used in OFETs to extract this parameter consists of plotting the square root of the saturation current as a function of the gate voltage (Figure 4.2b). The intercept of the extrapolated linear curve with the gate-voltageaxis defines the threshold voltage.

In linear regime ($V_{DS} \leq V_{GS} - V_{Th}$), I_{DS} increases linearly with V_{DS} and is described by the following equation:

$$I_{DS} = \mu C_i \frac{W}{L}\left[(V_{GS} - V_{Th})V_{DS} - \frac{V_{DS}^2}{2}\right] \qquad \text{(eq. 4.1)}$$

where L is channel length, W is the channel width, C_i is the capacitance per unit area of the insulating layer, V_{Th} is the threshold voltage. The mobility can be determined in linear regime from the transconductance:

$$g_m = \left(\frac{\partial I_{DS}}{\partial V_{GS}}\right)_{V_{DS}=\cos t} = \mu C_i \frac{W}{L} V_{DS} \qquad \text{(eq. 4.2)}$$

by plotting I_{DS} versus V_{GS} at constant low V_{DS} with $V_{DS} < (V_{GS} - V_{Th})$ and equating the value of the slope of this plot to g_m.

For $V_{DS} > V_{GS} - V_{Th}$, I_{DS} tends to saturate (saturation regime) due to the pinch-off the accumulation layer, and is modelled by the following equation:

$$I_{DS} = \frac{1}{2}\mu C_i \frac{W}{L}(V_{GS} - V_{Th})^2 \qquad \text{(eq. 4.3)}$$

In the saturation regime, μ can be determined from the slope of the plot of $\sqrt{I_{DS}}$ vs. V_{GS}. Although it is expected that mobility values extracted from linear and saturation transfer-curves are very similar, this is not always the case for OFET[3]. Indeed, source and drain contact resistances (which are not taken into account in the previous equations) can strongly influence the electrical behaviour of the organic transistors.

The ratio of the current in the accumulation mode over the current in the depletion mode is referred to as I_{ON}/I_{OFF}. The I_{ON}/I_{OFF} ratio measures the efficiency of the device switch.

4.3 n-type OFETs based on Perylene Diimide derivatives

Organic Thin Film Transistors have received much attention for the fabrication of low cost, flexible and large area electronic circuitry [7]. Both p-type and n-type OFETs are required for the development of organic complementary metal oxide semiconductor (CMOS) circuits [8–10], which are able to provide electronic components with superior performances in terms of low static power consumption and higher noise margins. Different from p-channel semiconductors which have been widely studied for more than 20 years and exhibit excellent field-effect characteristics [11,12], today n-channel semiconductors are less commonly employed because of the low air stability and limited processing capability. Indeed, despite many experimental works carried out over the past few years, nowadays the number of n-channel compounds able to operate in ambient conditions with good charge mobility (μ) remains very limited. Among them, Cyanated Perylene

Carboxylic Diimide derivatives are certainly the most promising n-channel candidates owing to the high μ values (0.1 - 1 cm^2/V s) [13,14], low sensitivity to oxygen and moisture [15,16], remarkable environmental stability [17], good solubility in common organic solvents such as toluene (TOL), chloroform (CF) and o-dichlorobenzene (DCB). In particular, this last feature opens the way to the fabrication of OFETs by direct printing methods, like the inkjet technology, which are able to guarantee many advantages including low costs, low material wastage, selective deposition of materials and non-contact patterning [18]. In electrically-active organic devices, the semiconductor morphology plays a crucial role in determining the final performances given the widely demonstrated correlation between the crystalline microstructure of the organic layer and the corresponding charge transport properties [19]. This issue is even more critical if the semiconductor is deposited by inkjet printing, since the drop drying process drastically modifies the morphology of the deposited material and can strongly affect also its overall uniformity [20]. The poor uniformity of inkjet printed films is mainly caused by the so called ‘coffee-stain’ effect. This phenomenon is ruled by the convective flow occurring inside the sessile drop from its centre towards the edges, where the evaporation rate is higher, for replenishing the evaporation losses [21]. As a consequence, at the end of the drying process, the organic semiconductor results largely localized at the rim of the printed droplet. A possible approach to reduce the “coffee-stain” effect is based on the use of mixtures of solvents with different boiling points and surface tensions. By mixing suitable high- and low-boiling point solvents, indeed, temperature and surface tension gradients can be generated producing a Marangoni flow from droplet rim to the centre [22–24]. This capillary flow balances the ‘coffee-stain’ effect providing an appropriate spatial redistribution of the material. In this way, morphology and uniformity of the printed films and, more in general, the performances of the final devices can be improved by choosing the appropriate component solvents, with particular care to their volatility and surface tension properties, and their mixing ratio [23,24].

4.3.1 OFETs fabrication

In this thesis work, N,N'-bis(n-octyl)-1,6-dicyanoperylene-3,4:9,10-bis(dicarboximide) (PDI-8CN_2) films were deposited by inkjet printing on Si(gate)/bare SiO_2 (dielectric)/Au (contacts) substrates for the fabrication of n-channel organic transistors. PDI-8CN_2 is a molecule characterized by a rigid core ad by the presence of cyanated groups which make it soluble (Figure 4.3).

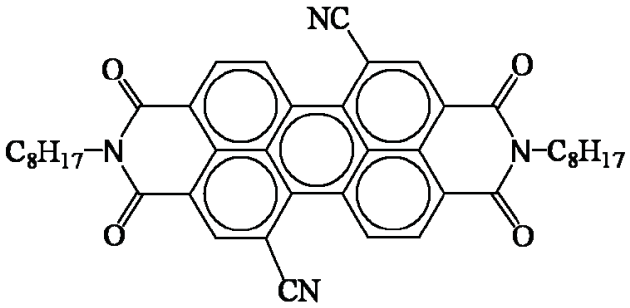

Figure 4.3 Perylene PDI-8CN_2 molecule. The circles inside the five core hexagons indicate conjugated bonds with delocalized π orbitals.

Inkjet printed bottom-gate bottom-contact OFETs were fabricated on substrates consisting of a 500 μm thick highly doped Silicon (Si^{++}) layer, thin (200 nm) SiO_2 dielectric barriers and pairs of interdigitated gold source-drain electrodes with 3-5 nm of chromium employed as primer to improve the adhesion. The schema of the structure of the transistor is reported in Figure 4.4a.

The active channels of the manufactured transistors have two possible lengths: L = 20 μm (Type I devices, FET3,4) and L = 40 μm (Type II devices, FET1,2) (Figure 4.4b). For all devices, however, the ratio between width (W) and length (L) of the active channels is fixed at 550. Taking into account the size of the interdigitated electrodes, the overall area printed was about 0.56 mm^2 for Type I devices and 1.65 mm^2 for Type II devices.

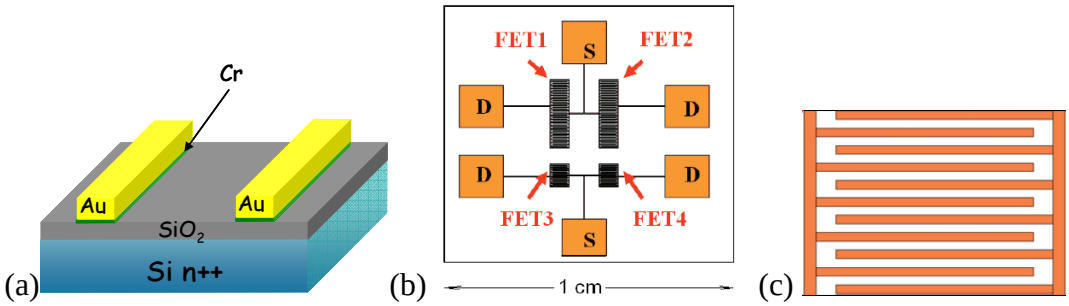

Figure 4.4(a) Schema of the OFET structure, (b) test pattern layout with source and drain gold contacts and (c) magnification of the interdigitated electrode/channel structure.

Before printing of the semiconductor, the bare substrates were cleaned in sequence in ultrasonic baths of acetone and isopropanol and dried with pure nitrogen (N_2) flow. PDI-8CN_2 (Polyera ActivInk N1200, Polyera Corporation) was dissolved at 6 mg/mL concentration in mixtures of o-dichlorobenzene and chloroform at different mixing volume ratios (DCB:CF 1:0, 4:1, 3:2, 1:4) in order to investigate the effect of solvents and their mixtures on the printing quality. The possibility to use the single-solvent system (0:1 DCB:CF) was not considered, since CF low boiling point prevents to get the stable drop emission condition. The chosen solvents are the most suitable to dissolve the semiconductor material and have right volatility and surface tension properties for the inkjet printing processing (DCB: T_b = 180 °C, γ = 26.84 mN/m; CF: T_b = 61 °C, γ = 27.5 mN/m).

The prepared solutions were used as inks after filtering by means of a 0.2 µm PTFE filter in order to remove possible agglomerates. The organic semiconductor based inks were deposited by means of the inkjet equipment already described in the chapter 1. The piezoelectric Drop on Demand (DoD) Microdrop printhead is characterized by a 30 µm opening nozzle which corresponds to 20 pL droplet volume. Moreover, the system allows to control the substrate temperature from the ambient conditions (T_{amb}) up to 100 °C. Sequences of droplets were printed at 10 Hz drop emission frequency and at printhead speed of 0.3 and 0.5 mm/s. During the printing process, the substrate temperature was optimized for each mixing ratio in order to prevent coalescence of the droplets printed on the target substrate.

4.3.2 Morphological characterization

Morphological characterization were performed on the printed PDI-8CN_2 semiconductor films in order to analyze the effects of the mixing ratio of the solvents and printing parameters (drop overlapping degree, substrate temperature) on the film quality.

In Figure 4.5 are reported the polarized optical microscopy images (Polyvar MET Reichert-Jung) and the corresponding profilometric analyses (Tencor P10) of printed PDI-8CN_2 droplets.

This figure shows that the single-solvent system 1:0 DCB:CF generates an uneven deposition of the material due to the "coffee-stain" effect. Hence, a ring like profile, with lateral humps at the droplet rim and a thinner layer in the centre, is observed in both the optical image (Figure 4.5a) and the corresponding 2D profile (Figure 4.5e).

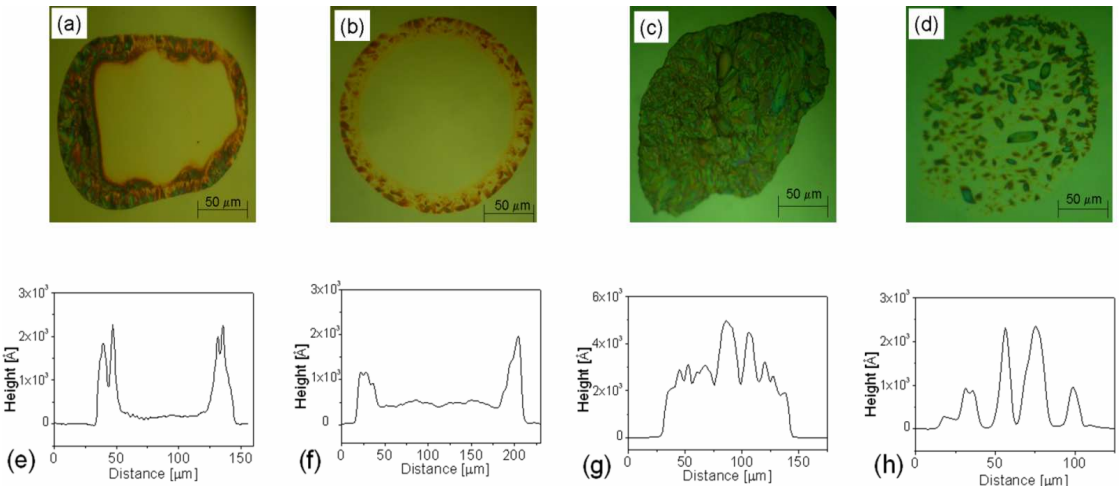

Figure 4.5 Polarized optical images and corresponding 2D profiles of PDI-8CN_2 drops on bare SiO_2 substrates. The drops are inkjet printed by using DCB:CF mixtures at different volume mixing ratios and substrate temperatures: a,e) 1:0 @ T=90°C; b,f) 4:1 @ T=90°C; c,g) 3:2 @ T=90°C; d,h) 1:4 @ T=35°C.

On the other hand, by increasing the CF content, which has a lower boiling point and a higher surface tension than DCB, an inward Marangoni flow was generated during the droplet drying process in such a way to reduce the height of the humps at the droplet rim. This phenomenon is clearly observable in the 2D profiles of the investigated mixtures, as depicted in Figure 4.5f,g,h. In particular, Figure 4.5f

outlines how the CF presence reduces the ratio between the lateral hump height and the height of the droplet centre. Moreover, it was found that the film uniformity can be further improved if a suitable mixing ratio of the component solvents is considered. Thus, the optical images and the related profilometric analyses reveal that the best condition is achieved using 3:2 DCB:CF mixture (Figure 4.5c,g). At this condition, the substrate region on which the single drop was printed appears fully covered by the material, without the presence of empty zones. Finally, the further increase of the CF content (1:4 DCB:CF, Figure 4.5d) leads to the formation of small crystallites spread over the printed drop region and separated each other with marked empty regions.

Organic thin film transistors were fabricated by inkjet printing PDI-8CN_2 films on Si^{++}/SiO_2 substrates with interdigitated gold source-drain electrodes. Films were obtained by printing overlapped lines (50% overlapping degree), each one realized by the sequence of overlapped drops. The lines were obtained with a drop overlapping degree of 50% and 70%, nevertheless for all the mixing ratios the optimal condition for forming uniform printed layers resulted 50%. The devices were realized with all the analyzed mixing ratios in order to investigate the effect of the drop overlapping on the printed film uniformity and, hence, on the performances of the final transistors.

In Figure 4.6 the polarized optical images and the corresponding SEM (LEO 1530) analyses of the printed PDI-8CN_2 films are reported for each mixing ratio. For the mixing ratios 1:0, 4:1 and 3:2 DCB:CF, where the contribution of the higher boiling point solvent was greater, the substrate temperature was kept at 90 °C in order to reduce the coalescence of the printed droplets. For 1:4 DCB:CF mixing ratio, where the concentration of the lower boiling point solvent is higher, the substrate temperature was optimized at T = 35 °C in order to avoid nozzle clogging that could be thermally induced by higher temperatures for the proximity effect between the printhead and substrate.

Despite the occurrence of the “coffee-stain” phenomenon for the printed single-drops by using pure DCB as solvent (1:0 DCB:CF) (Figure 4.5a), the overlapping effect induces the formation of an almost uniform film (Figure 4.6a). In this case, the morphology of PDI-8CN_2 film is characterized by the presence of large sized grains

induced by the slow crystallization process due to the DCB high boiling point, similarly to the observed structure at the rim of the printed single-drop (Figure 4.5a). On the contrary, as represented in Figure 4.6b,c,d, the increasing content of the lower boiling point solvent causes the fast precipitation of PDI-8CN_2 generating a more and more pronounced concentration of smaller crystallite grains.

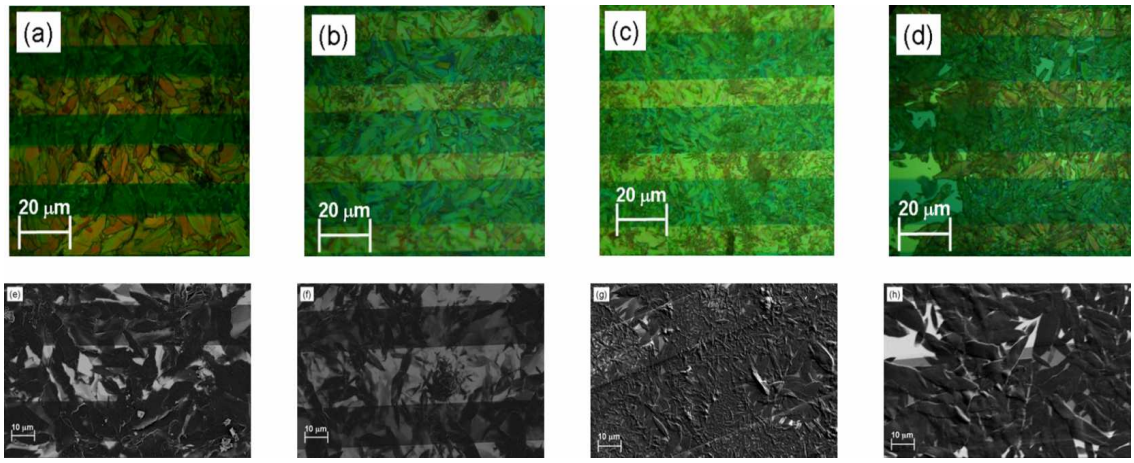

Figure 4.6 Polarized optical images and corresponding SEM analyses for PDI-8CN2 films printed transverse to interdigitated fingers by different DCB:CF mixtures: (a,e) 1:0; (b,f) 4:1; (c,g) 3:2; (d,h) 1:4.

The results of the optical analysis were further supported by the SEM images showing the presence of a large grain structure for the sample obtained by the single solvent system (Figure 4.6e), a more uniform structure formed of larger grain domains (average size 15 μm) intercalated with smaller crystallites (with average size 2 μm), mostly oriented along the printing direction transverse to interdigitated fingers, for the DCB:CF mixing ratio equal to 3:2 (Figure 4.6g), and, finally, an uneven configuration with small crystallites alternated to empty regions for the 1:4 DCB:CF (Figure 4.6h). In the last case, a wide disorder of the crystallite orientation is observed with a non uniform and random distribution with respect to the interdigitated contacts. Moreover, for these devices, in order to take into account the incomplete coverage of the active channels, the theoretical W/L ratios were corrected after a careful inspection by the optical microscope.

A more detailed view of the film morphology in the regions where large and small sized crystallites coexist is shown in Figure 4.7, in which are reported the atomic

force microscopy (AFM, XE100 Park instruments) for all the mixing ratio analyzed. AFM characterization was carried out in non-contact mode amplitude modulation by using a silicon nitride cantilever from Nanosensor.

The analysis of 30x30 μm^2 AFM images showed that for the DCB:CF mixing ratios of 1:0 and 3:2 (Figure 4.7a,c) the root mean square roughness (R_q) was about 100 nm with the presence of film regions characterized by the presence of peaked zones with height up to 200 nm. For the optimized 3:2 DCB:CF mixture it is possible to observe the presence of large crystallite (red dashed line in Figure 4.7c) where the film surface appears flatter and the surface roughness is about 40 nm. The AFM images for the 4:1 and 1:4 DCB:CF mixtures (Figure 4.7b,d) gave a higher roughness value of about 150 nm due to the presence of peaked zone intercalated by disordered crystallites. In particular, considering the mixture with higher presence of CF solvent (which have the lower boiling point and surface tension properties) (Figure 4.7d), the morphology was characterized by the presence of larger crystallite intercalated with empty zones which could make the charge transport more difficult.

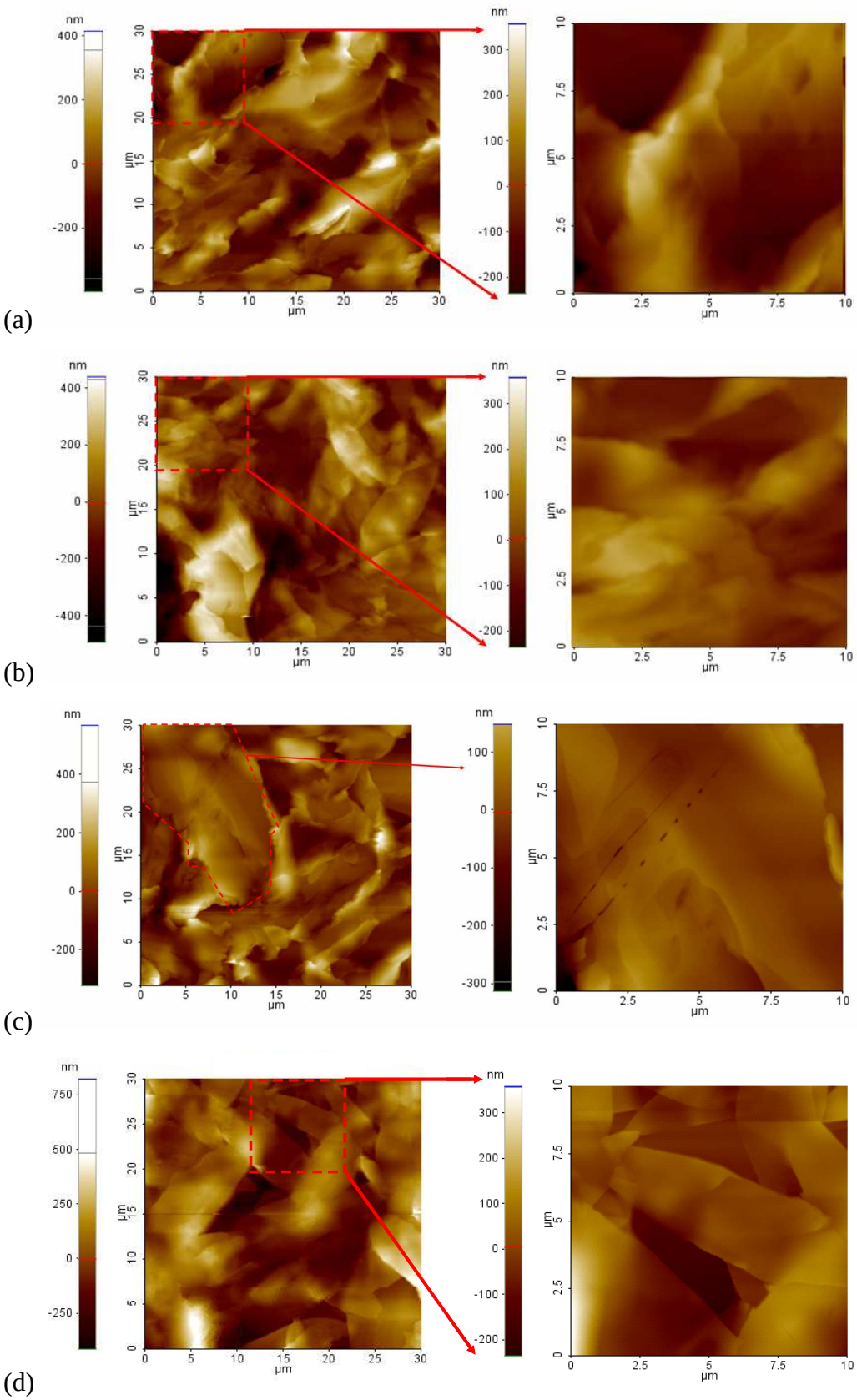

Figure 4.7 AFM images 30x30 μm^2 and a magnification of 10x10 μm^2 of printed PDI-8CN_2 films employing mixing ration DCB:CF (a) 1:0; (b) 4:1; (c) 3:2 and (d) 1:4.

4.4.3 Electrical characterization

The electrical response of the fabricated OFETs was investigated through the output and transfer-curves. All electrical measurements were carried out in vacuum (10^{-4} mbar) and in dark by using Janis Cryogenic Probe-Station system connected to a Keithley 2612A Dual-Channel source-meter instrument.

Figure 4.8a shows the typical output-curves recorded for the inkjet printed PDI-$8CN_2$ transistors. These measurements refer to a device fabricated by the 3:2 DCB:CF mixture, however, the main qualitative features of these curves were found common to all the analyzed devices independently from the solvent mixture. In particular, the electrical response of all devices was characterized by the presence of not negligible contact resistances (R_C) between the source-drain electrodes and the organic layer. This occurrence is specifically represented by the well evident sub-linear behavior of the output curves in the low drain-source (V_{DS}) voltage region. At this stage, the physical origin of the contact resistances is not clear and further experiments are required for the better understanding of this issue. It is likely, however, that the main contribution to R_C can be ascribed to the charge injection process from the gold source electrode to the disordered semiconductor, which is energetically characterized by a wide distribution of localized states close to the PDI-$8CN_2$ LUMO level.

On the other hand, the output curves (Figure 4.8a) reveal that the manufactured transistors are able to carry significant currents (in the range of μA) even if no gate-source (V_{GS}) voltage is applied. This feature should be mainly related to the large electron affinity of Cyanated Perylene derivatives which, interacting with the chemical species (carbonyl and silanol groups) present on the SiO_2 surface, give rise to an unintentional doping process providing a significant density of free charge carriers. In this way, these transistors can be considered as “normally on” and could be operated both in accumulation and depletion modes.

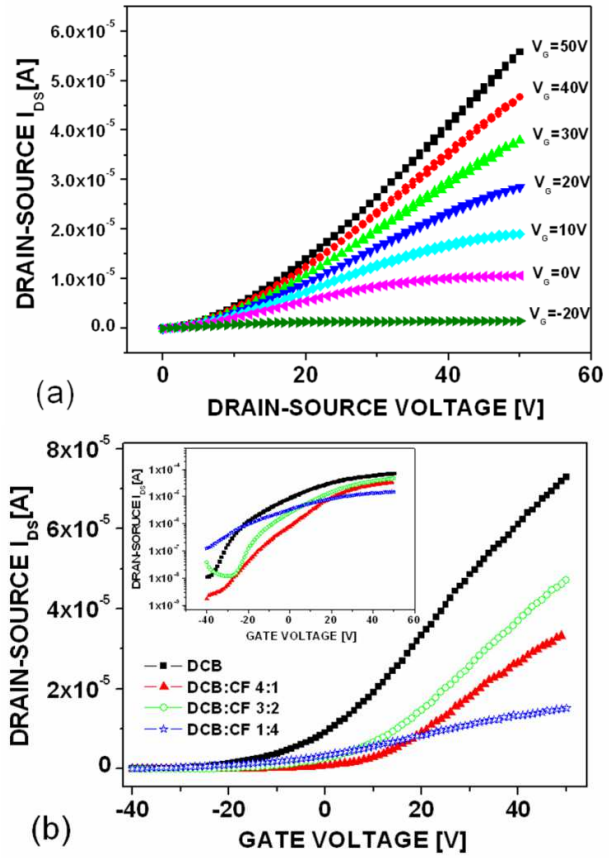

Figure 4.8 Electrical response of inkjet printed PDI-8CN_2 OFETs: a) 3:2 DCB:CF output curves; b) transfer-curves in saturation regime (V_{DS} = 50 V) of OFETs printed by employing different DCB:CF mixtures (in the inset the same curves are reported in semi-log scale).

In order to gain a straight comparison among the electrical performances of transistors fabricated starting from different DCB:CF mixtures, the corresponding transfer-curves measured in saturation regime (V_{DS} = 50 V) are shown in Figure 4.8b. These curves were recorded for Type I devices with L = 20 μm. The ability of the devices to exhibit a significant conductance also in absence of V_{GS} is further confirmed by these measurements. The values of the onset voltage (V_{on}), defined as the voltage where the current I_{DS} starts to increase in the semi-log plot, are in the range between -30 V and -40 V (inset of Figure 4.8b). No clear correlation was found between V_{on} values and the composition of the solvent mixture.

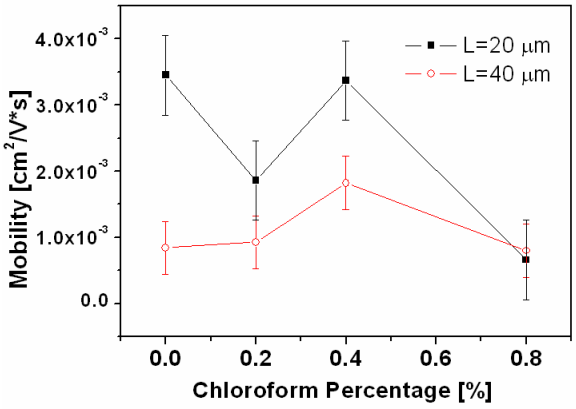

Figure 4.9 Mobility values evaluated from the transfer-curves in the saturation regime for inkjet printed PDI-8CN2 OFETs as a function of CF volume percentage in DCB: CF mixtures.

On the contrary, concerning both the maximum current and mobility values, the best performances were found for transistors fabricated by 1:0 and 3:2 DCB:CF mixtures. In particular, Figure 4.9 reports the plot of the mobility values, calculated in the saturation regime by using the standard MOSFET equations, as function of the chloroform percentage contained in the solvent mixing ratios. Mobility (μ) values are given for both Type I (square symbols) and Type II (circle symbols) devices. This analysis shows that for transistors with channel length L = 20 μm, the electrical performances of 3:2 DCB:CF devices are similar (μ ~ 0.0035 $cm^2/V*s$) to the single-solvent samples obtained by employing pure DCB. These mobility values, much lower than the maximum mobility values (about 0.1 $cm^2/V*s$) reported in literature for PDI-$8CN_2$ transistors [13,14], can be attributable to both the transistor configuration (bottom-gate bottom-contact) and the specific deposition process (inkjet printing). In detail, it should be mentioned that PDI-$8CN_2$ transistors fabricated by evaporation on the same substrate type ($Si/SiO_2/Au$) display maximum mobility values ranging between 0.02 and 0.03 $cm^2/V*s$ [15]. Hence, the mobility reduction by one order of magnitude, observed for the inkjet printed PDI-$8CN_2$ active layers, can be ascribed solely to the specific characteristics of the deposition method in good agreement with other results recently reported in literature (see in particular ref. [14] and Table 1 therein).

Figure 4.9 also reveals that, when devices with L = 40 μm are considered, the 3:2 DCB:CF OFETs exhibit higher mobility values in comparison with the pure DCB solvent devices. In particular, it is possible to point out that, even if the mobility decrease between L= 40 μm and L= 20 μm devices is common to all the solvent mixing ratios, the reduction factor is smaller than 2 when 3: 2 DCB:CF solvent mixture is considered, while it exceeds 4 for the transistors deposited from the pure DCB solvent. This finding seems to confirm that the solvent mixture approach, with the optimized mixing ratio of 3:2 DCB:CF, is able to better ensure the film uniformity and to limit the degradation of the device performances when larger printed areas are considered. Finally, it can be noticed how, in agreement with the optical analysis, the worst transistor performances were found for 1:4 DCB:CF devices.

4.5 Summary

In this fourth chapter of this thesis activity the fabrication of n-channel Cyanated Perylene (PDI-8CN_2) organic thin film transistors using the inkjet technique as method for printing the semiconductor layers is performed. In order to improve the uniformity of the printed films, an approach based on the employment of solvent mixtures, with different boiling points and surface tensions, was followed. For each mixture composition, the printing parameters, such as substrate temperature and drop overlapping degree, were optimized to improve the reproducibility of the deposition process and the structural quality of the final films.

The competing effect of the convective and inward Marangoni flows on the crystalline microstructure of PDI-8CN_2 was studied through morphological analyses by means of polarized optical microscopy, scanning electron microscopy (SEM) and atomic force microscopy (AFM).

The choice of an optimized ink composition was demonstrated to induce a specific morphology of PDI-8CN_2 films where larger grain domains are intercalated with smaller crystallites mostly oriented along the printing direction. The analysis of the electrical responses indicates that devices fabricated by the optimized solvent

mixture (3:2 DCB:CF) can retain good electrical performances even when the size of the active channel is significantly increased. The analysis of the results showed that the performances of the OFETs depends critically on understanding and controlling the organic material's molecular organization at interfaces gold/semiconductor. These results confirm that the solvent mixture approach is an interesting route to better address the uniformity issue in the inkjet printing technique applied to the development of organic electronic circuitry.

Bibliography

[1] A. Tsumura, H. Koezuka, T. Ando, Macromolecular electronic device: Field-effect transistor with a polythiophene thin film, Applied Physics Letters. 49 (1986) 1210.
[2] S.M. Sze, Physics of Semiconductor Devices, 2nd ed., Wiley-Interscience, 1981.
[3] C.D. Dimitrakopoulos, D.J. Mascaro, Organic thin-film transistors: A review of recent advances, IBM Journal of Research and Development. 45 (2001) 11-27.
[4] G. Horowitz, R. Hajlaoui, R. Bourguiga, M. Hajlaoui, Theory of the organic field-effect transistor, Synthetic Metals. 101 (1999) 401-404.
[5] A.R. Brown, C.P. Jarrett, D.M. de Leeuw, M. Matters, Field-effect transistors made from solution-processed organic semiconductors, Synthetic Metals. 88 (1997) 37-55.
[6] G. Horowitz, Organic Field-Effect Transistors, Advanced Materials. 10 (1998) 365-377.
[7] V. Subramanian, J.M.. Frechet, P.C. Chang, D.C. Huang, J.B. Lee, S.E. Molesa, et al., Progress Toward Development of All-Printed RFID Tags: Materials, Processes, and Devices, Proceedings of the IEEE. 93 (2005) 1330-1338.
[8] H. Klauk, U. Zschieschang, J. Pflaum, M. Halik, Ultralow-power organic complementary circuits, Nature. 445 (2007) 745-748.
[9] T.D. Anthopoulos, B. Singh, N. Marjanovic, N.S. Sariciftci, A. Montaigne Ramil, H. Sitter, et al., High performance n-channel organic field-effect transistors and ring oscillators based on C[sub 60] fullerene films, Appl. Phys. Lett. 89 (2006) 213504.
[10] F. Dinelli, R. Capelli, M.A. Loi, M. Murgia, M. Muccini, A. Facchetti, et al., High□Mobility Ambipolar Transport in Organic Light□Emitting Transistors, Advanced Materials. 18 (2006) 1416-1420.
[11] M. Mas-Torrent, M. Durkut, P. Hadley, X. Ribas, C. Rovira, High Mobility of Dithiophene-Tetrathiafulvalene Single-Crystal Organic Field Effect Transistors, Journal of the American Chemical Society. 126 (2004) 984-985.
[12] S. Allard, M. Forster, B. Souharce, H. Thiem, U. Scherf, Organic Semiconductors for Solution-Processable Field-Effect Transistors (OFETs), Angewandte Chemie International Edition. 47 (2008) 4070-4098.
[13] H. Yan, Z. Chen, Y. Zheng, C. Newman, J.R. Quinn, F. Dotz, et al., A high-mobility electron-transporting polymer for printed transistors, Nature. 457 (2009) 679-686.
[14] H. Yan, Y. Zheng, R. Blache, C. Newman, S. Lu, J. Woerle, et al., Solution Processed Top-Gate n-Channel Transistors and Complementary Circuits on Plastics Operating in Ambient Conditions, Advanced Materials. 20 (2008) 3393-3398.
[15] B.A. Jones, A. Facchetti, M.R. Wasielewski, T.J. Marks, Effects of Arylene Diimide Thin Film Growth Conditions on n-Channel OFET Performance, Advanced Functional Materials. 18 (2008) 1329-1339.
[16] M. Barra, F.V.D. Girolamo, F. Chiarella, M. Salluzzo, Z. Chen, A. Facchetti, et al., Transport Property and Charge Trap Comparison for N-Channel Perylene

Diimide Transistors with Different Air-Stability†, The Journal of Physical Chemistry C. 114 (2010) 20387-20393.
[17] A.S. Molinari, H. Alves, Z. Chen, A. Facchetti, A.F. Morpurgo, High Electron Mobility in Vacuum and Ambient for PDIF-CN2 Single-Crystal Transistors, Journal of the American Chemical Society. 131 (2009) 2462-2463.
[18] T. Kawase, T. Shimoda, C. Newsome, H. Sirringhaus, R.H. Friend, Inkjet printing of polymer thin film transistors, Thin Solid Films. 438-439 (2003) 279-287.
[19] K.-J. Baeg, D. Khim, J.-H. Kim, M. Kang, I.-K. You, D.-Y. Kim, et al., Improved performance uniformity of inkjet printed n-channel organic field-effect transistors and complementary inverters, Organic Electronics. 12 (2011) 634-640.
[20] F. Villani, P. Vacca, G. Nenna, O. Valentino, G. Burrasca, T. Fasolino, et al., Inkjet Printed Polymer Layer on Flexible Substrate for OLED Applications, The Journal of Physical Chemistry C. 113 (2009) 13398-13402.
[21] R.D. Deegan, O. Bakajin, T.F. Dupont, G. Huber, S.R. Nagel, T.A. Witten, Contact line deposits in an evaporating drop, Phys. Rev. E. 62 (2000) 756.
[22] H. Hu, R.G. Larson, Marangoni Effect Reverses Coffee-Ring Depositions, The Journal of Physical Chemistry B. 110 (2006) 7090-7094.
[23] J.A. Lim, W.H. Lee, H.S. Lee, J.H. Lee, Y.D. Park, K. Cho, Self Organization of Ink-jet Printed Triisopropylsilylethynyl Pentacene via Evaporation Induced Flows in a Drying Droplet, Advanced Functional Materials. 18 (2008) 229-234.
[24] D. Kim, S. Jeong, S.H. Lee, J. Moon, J.K. Song, Ink-jet printing of organic semiconductor for fabricating organic thin-film transistors: Film uniformity control by ink composition, Synthetic Metals. 159 (2009) 1381-1385.

CHAPTER 5
ORGANIC SOLAR CELLS

Recently, great interest has been devoted to cost-effective alternative energy sources such as organic solar cells due to the low cost of fabrication, the mechanical flexibility and the versatility of chemical structure from advances in organic chemistry and ease of processing. As concerning this last point, the possibility of organic materials processing by solutions at low temperatures makes them employable for fabricating printed solar cells by using inkjet printing technology.

Polymer solar cells were manufactured by inkjet printing the regioregular poly(3-hexylthiophene) (P3HT):[6,6]-phenyl-C61-butyric acid methyl ester (PCBM) blend dissolved in pure solvents or solvent mixtures.

The influence of the chemico-physical properties of the solvents on the morphology of the active layer was investigated through morphological and electrical analyses.

5.1 Introduction of OPV

For the past two hundred years, global economic growth has been fuelled almost exclusively by conventional energy sources such as oil, coal and natural gas. Unfortunately, this fossil fuels are finite energy sources that are rapidly depleting. Moreover, greenhouse gas emissions from the use of fossil fuel have been widely agreed as one of the major contributor to man-made climate change. Considering these challenges, a more sustainable energy source is required as a long term solution to the energy needs.

One of the most attractive method for the generation of electricity is based on the photovoltaic (PV) technology. To date, silicon based-solar cells are the most employed photovoltaic devices but, recently, interests are involving in polymer solar cells (PSC) based on organic semiconductors. This class of materials permits to meet the electricity demand as well as offer secondary benefits such as the extension of the applications fields. In particular, this PSC can be used for laptop-recharging briefcases, window tinting, put into tents, umbrellas, awnings and others.

The solubility of the organic semiconductor and the processability at low temperatures allow their printability and, hence, the extension of the deposition methods for fabrication of organic solar cells to printing technologies which guarantee high production rate and low costs.

5.2 Photovoltaic working principle

The photovoltaic effect was discovered in 1839 by Edmund Becquerel by using an electrolytic cell made up of two metal electrodes. Becquerel observed that certain materials produced small amounts of electric current when exposed to light. In 1905, Einstein explained the photoelectric effect, which is the theoretical base for understanding the photovoltaic effect. When photons illuminate a metal surface, free electrons can escape from the metal surface due to excitation energy from the incident light. In most cases, the absorbed photons pump ground state electrons to the

excited state. In photovoltaic devices, the excited electrons and the produced hole in the ground state can be collected separately to produce power.

In order to convert sunlight into electricity, a solar cell devices should absorb as much light as possible in the solar spectrum range (Figure 5.1).

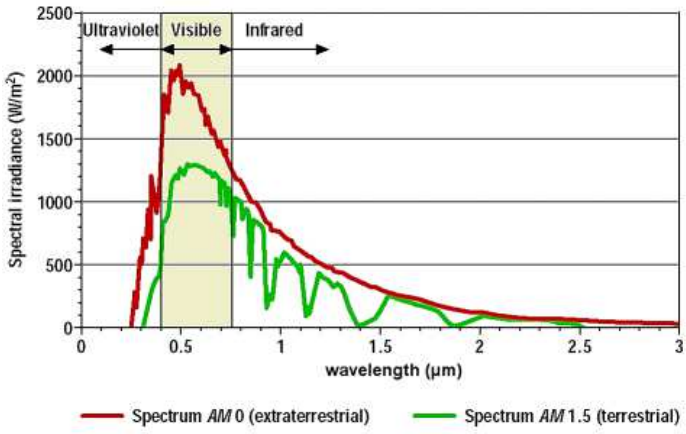

Figure 5.1 AM0 and AM 1.5 solar spectra.

The organic photovoltaic process, schematically reported in Figure 5.2, is composed of four steps: light absorption, charge generation, charge transport, and charge collection [1].

The first step is the light absorption which depends on the bandgap energy (E_g) of the semiconducting material and its intrinsic extinction coefficient. The second step is the charge generation due to sunlight photons which bring the electrons from the HOMO level (highest occupied molecular orbital) to excited state in the LUMO level (lowest unoccupied molecular orbital). The excited electrons slightly relax and then form an exciton, a bounded electron-hole pair. The exciton can diffuse inside the organic semiconductor with a characteristic diffusion length of about 10-20 nm. Because the exciton dissociation occurs only at the interface between the donor and the acceptor, if excitons don't reach the interface, they can recombine and the absorbed energy is dissipated without generating photocurrent [2]. Therefore, in order to realize a good organic solar cell an efficient dissociation of excitons is needed. The third step is the charge transport process which involves the transport of the dissociated charges towards the electrodes. During the charge pathways, if the transporting medium has defects such as charge traps or barriers that hinder charge

transport, the cell performance decreases. Therefore, in order to increase the cell performance it is necessary to optimize the transport process by reducing the losses. The fourth step is the charge collection, which occurs when the transported charges from the semiconductor to the cathode or anode are collected at the interface.

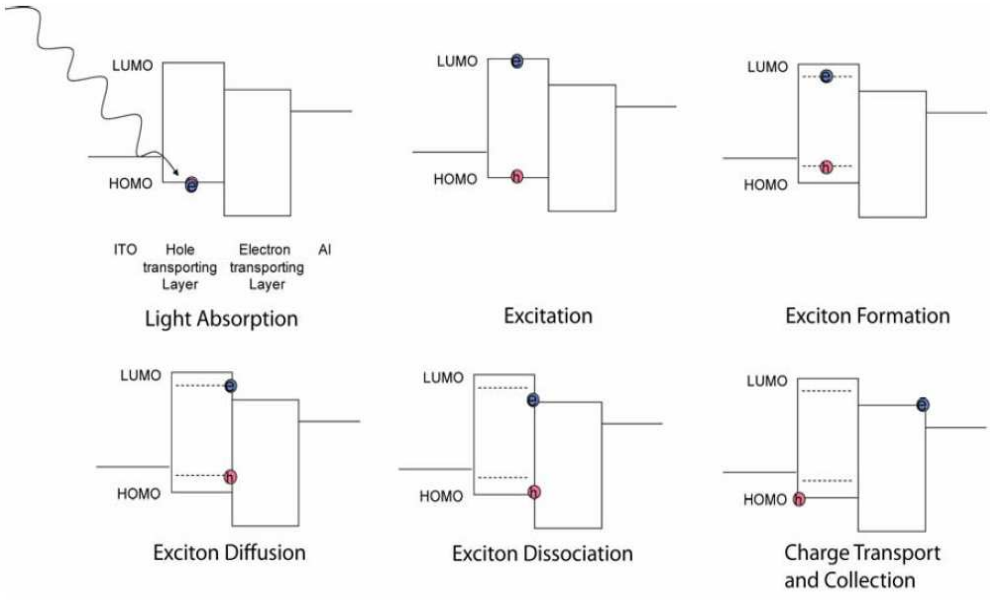

Figure 5.2 OPV working principle.

The electrical performance of an OPV cell is characterized by a current density-voltage curve (J-V), schematically reported in Figure 5.3a.

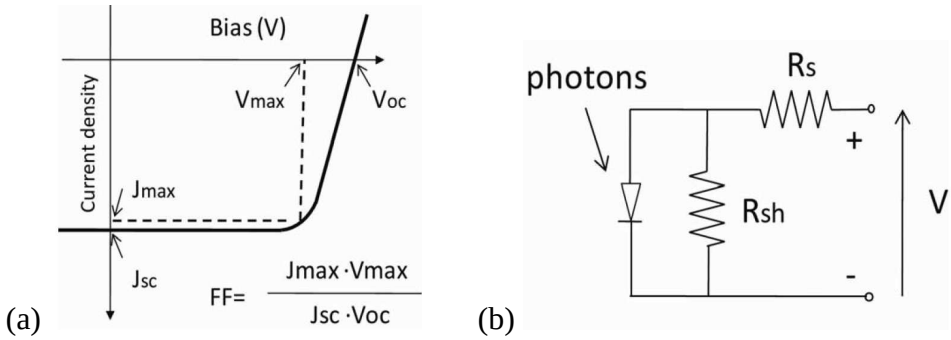

Figure 5.3 (a) Typical current density–voltage curve of an OPV solar cell and (b) schema of the equivalent circuit of a solar cell.

The main parameters that quantitatively characterize the working of a OPV cell are the short circuit current (J_{sc}), open circuit voltage (V_{oc}), fill factor (FF), and power conversion efficiency (PCE).

Figure 5.3a shows that the current-voltage product is negative and the cell generates power when the voltage is between 0 and V_{oc}. At V<0, the illuminated device acts as a photodetector, consuming power to generate a photocurrent that is light dependent but bias independent. At V>V_{oc}, the device again consumes power. This is the region where light emitting diodes operate.

The fill factor (FF) is defined as the ratio of the maximum obtainable power to the product of the open circuit voltage and short circuit current:

$$FF = \frac{J_{\max} V_{\max}}{J_{SC} V_{OC}} \qquad \text{(eq. 5.1)}$$

With this, the power conversion efficiency (η) can be written as:

$$\eta = \frac{P_{\max}}{P_{in}} = \frac{J_{\max} V_{\max}}{E \cdot A_C} = \frac{FF J_{SC} V_{OC}}{E \cdot A_C} \qquad \text{(eq. 5.2)}$$

where $J_{\max}$ is the maximum current density, $V_{\max}$ is the maximum voltage, E is the input light irradiance (in W/m^2) and A_C is the surface area of the solar cell.

In the real cell, power is dissipated through the resistance of the contacts and through leakage currents. These effects are electrically equivalent to two parasitic resistances placed in series (R_s) and in parallel (R_{sh}) as reported in Figure 5.3b. The series resistance arises from the resistance of the cell material to current flow, mainly through the front surface to the contacts. The parallel or shunt resistance arises from leakage of current through the cell. Since series and shunt resistances reduce fill factor, smaller R_s and larger R_{sh} values are required in order to fabricate an efficient OPV cell.

5.3 OPV solar cells based on P3HT:PCBM blend

Polymer solar cells (PSC) are evolved as a promising cost-effective alternative to silicon-based solar cells for their main advantages, such as low cost of fabrication, very high speed and easiness of processing, mechanical flexibility and versatility of chemical structure in organic chemistry [3–6].

Concerning the last item, the most exploited active material for photovoltaic devices is the regioregular poly(3-hexylthiophene) (P3HT), p-type conjugated polymer, blended with [6,6]-phenyl-C61-butyric acid methyl ester (PCBM), n-type material [7,8] (Figure 5.4).

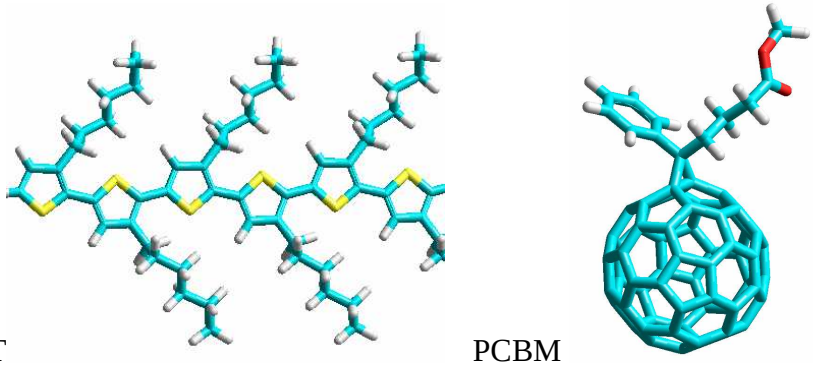

Figure 5.4 Chemical structures of P3HT and PCBM.

The high efficiency and the solubility of this two materials in organic solvents, like dichlorobenzene (DCB), chlorobenzene (CB) and chloroform (CF), allow the employment of industrial deposition methods like inkjet printing for the fabrication of large area organic solar cells. Among the various printing methods of functional materials for PSC applications, the inkjet printing (IJP) technology is particularly suited to realize patterned structures allowing an efficient use of the material, that means a reduction of the waste products and the processing steps and, hence, a reduction of the processing costs [5,9–13].

In organic solar cells, the active layer morphology plays a crucial role in determining the final device performances because it strongly influences the charge transport properties [14]. In particular, this issue is even more critical if the active material is deposited by inkjet printing due to the “coffee-stain” effect that governs the drop drying process [15]. This phenomenon determines an inhomogeneity of the

printed material that can be reduced by using mixtures of solvents with different boiling points and surface tensions so that a Marangoni flow is generated [16–18]. Therefore, the right formulation and processing of the ink through the control of the ink chemico-physical properties, the wetting of the ink/substrate system and the definition of the printing parameters, are fundamental elements in organic solar cell fabrication in order to improve the quality of the printed layers [11,15].

5.3.1 OPV fabrication

In the present work, the influence of single solvents, 1,2-dichlorobenzene (DCB) and chlorobenzene (CB), and their mixtures on the morphology and uniformity of P3HT:PCBM films, which were deposited by inkjet printing on glass substrates for the fabrication of polymer solar cells, was investigated. After optimizing the printing parameters (printhead speed, drop emission frequency and substrate temperature), the effect of the solvents on the morphology of P3HT:PCBM layer was analyzed through optical microscopy, scanning electron microscopy (SEM) and profilometric analysis. Organic photovoltaic cells were manufactured with ITO/PEDOT:PSS/ P3HT:PCBM/Ca/Al stack according to bulk heterojunction (BHJ) structure, currently the most efficient architecture for polymer solar cells, where the active layer was sandwiched between two electrodes with different work functions. The schematic of the device stack is shown in Figure 5.5.

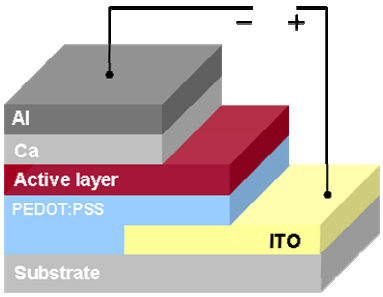

Figure 5.5 Schematic device structure of the manufactured polymer/fullerene bulk heterojunction solar cell.

ITO-coated commercial coated glass was used as substrate. The employed ITO on Corning®1737 glass (120 nm thick, sheet resistance < 15Ω/square) was cleaned through standard process with detergent, subsequently with acetone and isopropanol in ultrasonic bath, and, finally, drying in oven.

For PSC cell fabrication, ITO patterning was carried out through conventional photolithography to define the front electrode geometry.

A 50 nm thick film of poly(3,4-ethylenedioxythiophene) (PEDOT) doped with poly(styrenesulfonate) [(PEDOT:PSS), Baytron P HC Starck] was spin-coated from a watery solution at 5000 rpm for 60 sec onto the substrates, after filtering through a 0.45 μm filter. The PEDOT:PSS films were then dried at 140 °C for 10 min under nitrogen.

The active material, consisting of a blend of P3HT and PCBM, was then deposited onto the hole transport layer (PEDOT:PSS) using the IJP technique. Regioregular P3HT (Plextronics), electron donating material (p-type), and PCBM (Solenne BV), electron accepting material (n-type), were used as received. The blend was prepared by employing P3HT (6 mg/mL) and PCBM (4.8 mg/mL) with mixing ratio of 1:0.8 by weight and dissolving in two different single solvents, DCB (Tb = 180 °C, γ= 26.84 mN/m) and CB (Tb = 131 °C, γ = 33.4 mN/m), and in DCB:CB mixture at volume mixing ratios 1:4, 1:1 and 4:1. The solvents DCB and CB were chosen because they dissolve well the photoactive material and have right volatility and surface tension properties for inkjet printing processing. All the solutions were stirred on hotplate at 50 °C for 48 h.

The prints were carried out by means of the inkjet equipment already described in the chapter 1 using Microdrop printhead with 30 μm opening nozzle. Solar cells with 34 mm^2 active area were fabricated by printing the active material on the PEDOT:PSS/ITO bottom electrode. The printing parameters were 5 Hz drop emission frequency and 0.4 mm/s printhead speed with 50% overlapping degree. The substrate temperature was optimized for each ink in order to prevent the coalescence of the droplets printed on the target substrate and to reach the best film uniformity condition.

The thickness of the P3HT:PCBM layer were analyzed by means of a surface profilometer (KLA Tencor P-10 Surface Profiler). Optical micrograph, scanning

electronic microscopy (SEM, LEO 1530) and atomic force microscopy (AFM, Veeco Nanoscope IV) analyses were carried out to investigate the morphology of the printed films.

The devices were completed depositing Ca/Al top electrodes by thermal evaporation in ultra-high vacuum (10^{-7} mbar) through shadow mask.

The devices were annealed on hotplate at 150 °C for 20 min in a nitrogen filled glow box and then electrically characterized through external quantum efficiency (EQE) and current-voltage (I-V) measurements performed under simulated AM 1.5G illumination. I-V measurements were carried out by a Keithley 236 source measure unit (Keithley Instruments Inc., Cleveland, USA) applying a voltage ramp rate of 10 mV/s from positive to negative potential. A Spectrosun® Solar Simulator (X25, MARK II-Spectrolab USA) equipped with a AM1.5G filter was employed to provide the simulated AM 1.5G white light illumination, whose intensity was calibrated with an unfiltered mono-Si cell SC80 (certified by Fraunhofer ISE) for 1 sunlight intensity of 100 mW/cm^2. All the photovoltaic characterizations were performed in air at room temperature.

5.3.2 Morphological characterization

Optical micrograph images and the profilometric analyses of the printed P3HT:PCBM films by dissolving the blend in pure CB and DCB solvents and DCB:CB solvent mixtures are reported in Figure 5.6 and Figure 5.7, respectively.

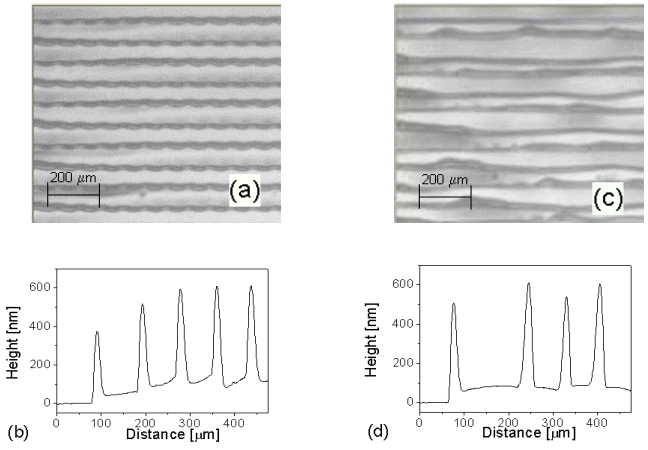

Figure 5.6 Optical images and corresponding 2D-profiles of films of P3HT:PCBM dissolved in (a, b) CB, (c, d) DCB.

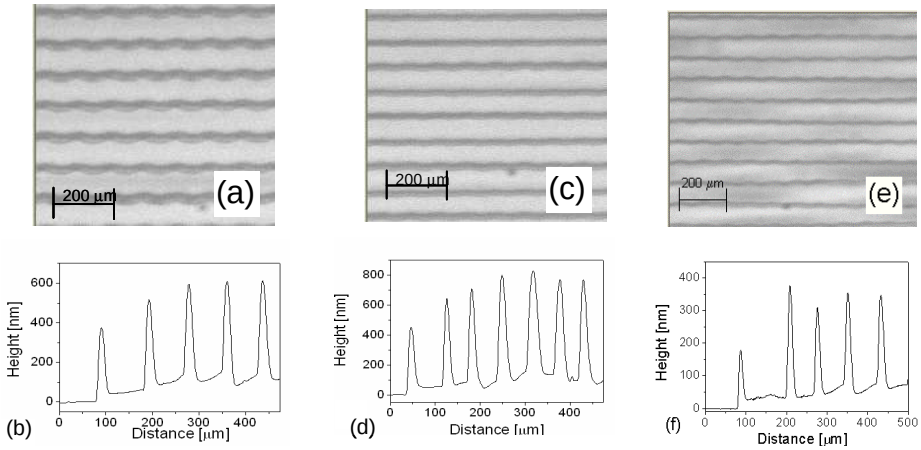

Figure 5.7 Optical images and corresponding 2D-profiles of films of P3HT:PCBM dissolved in DCB:CB @ (a, b) 1:4, (c, d) 1:1 and (e,f) 4:1 mixing ratios.

For all the printed films, the analyses showed a morphology characterized by the presence of the solute accumulation at the printed line edges. This effect is related to the solute diffusion from the droplet centre towards the rim due to the higher evaporation rate at the edge of the droplet. This phenomenon, known as "coffee-stain effect", induces an inhomogenity in the profile at the end of the drying process clearly observable in the Figure 5.6b,d and Figure 5.7b,d,f. Although the chemico-physical properties of each ink (vapour pressure, boiling, surface tension) induced a different wetting of the ink-substrate system, the profile features were almost the same for all the printed films obtained from different investigated solutions. This was the result of the optimization of the printing parameters performed for each ink in order to obtain continuous and uniform films.

The thicknesses of the printed films were estimated around 150 nm.

In Figure 5.8, the SEM analyses of the printed polymer:fullerene films are reported. The images showed the typical surface profile previously observed both in optical and profilometric analyses. Additionally, this analysis highlighted the presence of some structures (circle in Figure 5.8d,e) preferentially close to the printed line edges. These structures could be related to the phase demixing at the film surface.

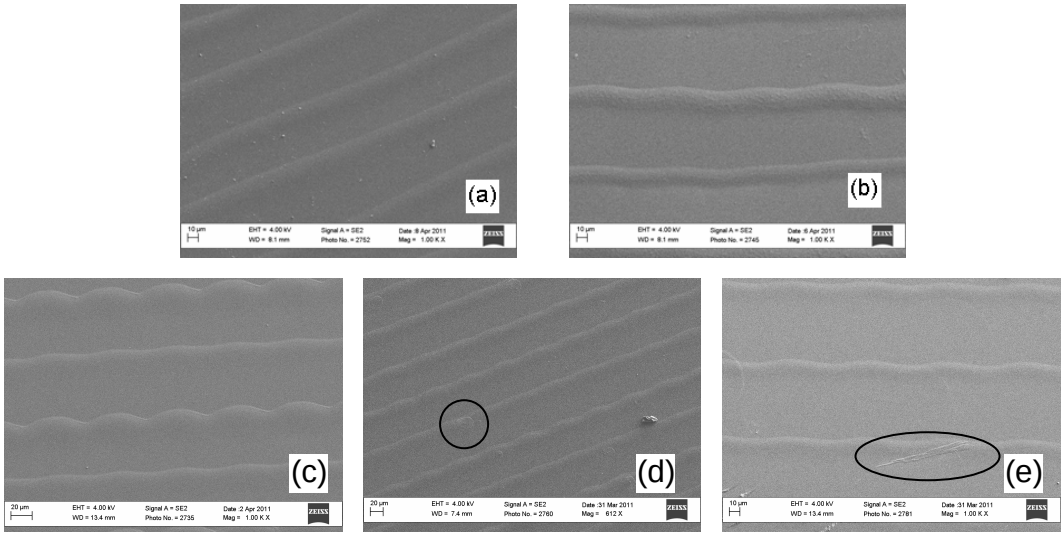

Figure 5.8 SEM images of the inkjet printed films of P3HT:PCBM dissolved in (a) CB, (b) DCB, and DCB:CB @ (c) 1:4, (d) 1:1, (e) 4:1 mixing ratios.

In order to investigate the influence of the quality of the active material films on the solar cells performances, the devices were completed with Ca/Al cathode and characterized immediately after the annealing process.

5.3.3 Electrical characterization

The current density versus voltage (J-V) curves for the manufactured solar cell by using pure solvents and the DCB:CB 4:1, are shown in Figure 5.9.

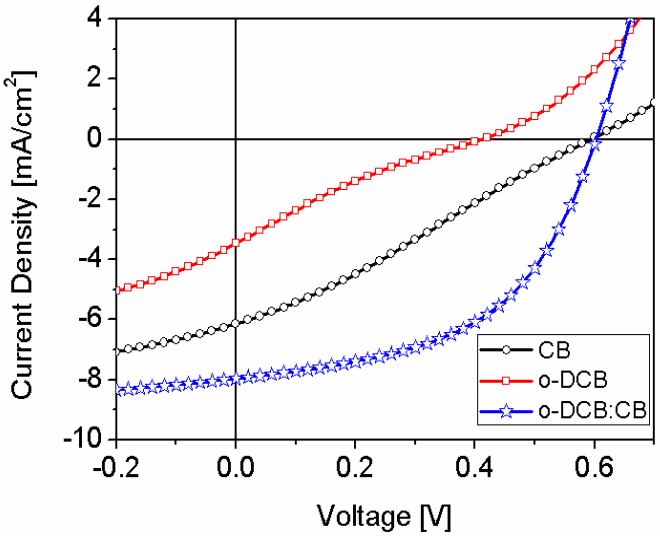

Figure 5.9 J-V light curves for photovoltaic devices realized by inkjet printing a blend of P3HT:PCBM dissolved in CB (circle), DCB (square) and DCB:CB (4:1) (star).

The corresponding parameters extracted from J-V curves for all the investigated devices, such as V_{oc}, J_{sc}, fill factor (FF) and power conversion efficiency (η) of the devices are summarized in Table 5.1.

Solvent	**η [%]**	**FF[%]**	**J_{SC} [mA/cm^2]**	**V_{OC} [mV]**
CB	1.0	28	6.1	594
DCB	0.3	20	3.5	412
DCB:CB 1:4	1.2	35	7.5	465
DCB:CB 1:1	2.2	53	7.1	568
DCB:CB 4:1	2.4	51	8.0	602

Table 5.1 Summary of the characteristics of the photovoltaic devices showing the power conversion efficiency (η),the fill factor FF, the short circuit current J_{SC} and the open circuit voltage V_{OC} .

The electrical analysis showed that the use of the solvent mixture strongly enhances the device performances. This can be attributed to the improvement of the homogeneity of the active material film as previously observed and also to a suitable phase separation induced from the solvent mixture.

In particular, on the solar cell realized by using DCB:CB 4:1 which showed the best electrical performances, AFM analysis was performed (Figure 5.10).

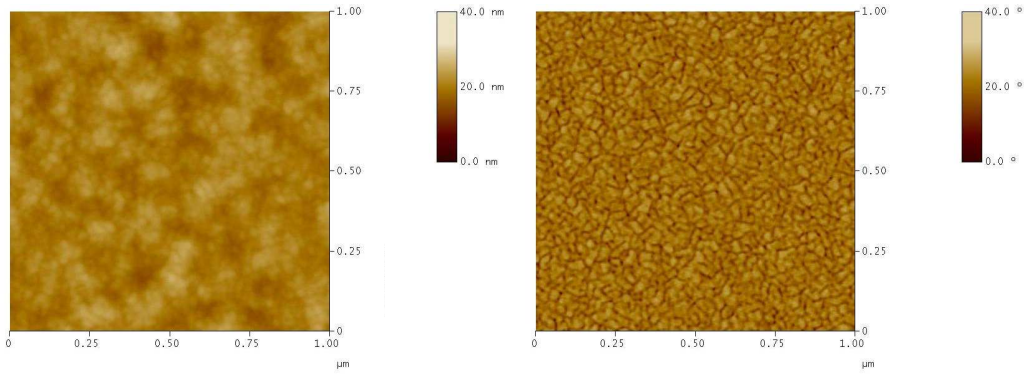

Figure 5.10 AFM images (topography (left) and phase(right)) of the P3HT:PCBM blend printed by using DCB:CB 4:1 as solvent mixture.

The results of this analysis showed that for the optimized mixing ratio the morphology of the printed active layer is almost uniform with a clear phase separation between P3HT and PCBM. This phase separation is characterized by domains with average size of about 20 nm. This is a result of polymer self organization that leads to an increase in device power conversion efficiency.

5.4 Summary

In this fifth chapter the fabrication of P3HT:PCBM based solar cells using the inkjet printing technique as method for depositing the active material layer is reported. In order to improve the uniformity of the printed films, an approach based on the employment of solvent mixtures, with different boiling points and surface tensions, was followed. The best polymer solar cell realized by using a DCB:CB 4:1 volume mixing ratio has a power conversion efficiency of 2.4%. This higher electrical performance can be attributed to an improved film uniformity and morphology. Indeed, the analyses showed that the active material is characterized by a clear phase separation between the P3HT and PCBM (the donor and the acceptor, respectively) thanks to an optimized polymer organization which induces an higher conversion efficiency.

Bibliography

[1] S.R. Forrest, The Limits to Organic Photovoltaic Cell Efficiency, MRS Bulletin. 30 (2005) 28-32.
[2] M. Knupfer, Exciton binding energies in organic semiconductors, Applied Physics A: Materials Science & Processing. 77 (2003) 623-626.
[3] C.J. Brabec, V. Dyakonov, J. Parisi, N.S. Sariciftci, Organic Photovoltaics: Concepts and Realization, 1st ed., Springer, 2003.
[4] S. Günes, H. Neugebauer, N.S. Sariciftci, Conjugated polymer-based organic solar cells, Chem. Rev. 107 (2007) 1324-1338.
[5] F.C. Krebs, J. Fyenbo, M. Jørgensen, Product integration of compact roll-to-roll processed polymer solar cell modules: methods and manufacture using flexographic printing, slot-die coating and rotary screen printing, J. Mater. Chem. 20 (2010) 8994-9001.
[6] H. Hoppe, N.S. Sariciftci, Organic Solar Cells: An Overview, Journal of Materials Research. 19 (2004) 1924-1945.
[7] W. Ma, C. Yang, X. Gong, K. Lee, A.J. Heeger, Thermally Stable, Efficient Polymer Solar Cells with Nanoscale Control of the Interpenetrating Network Morphology, Advanced Functional Materials. 15 (2005) 1617-1622.
[8] Hwajeong Kim, Minjung Shin, Jiho Park, Youngkyoo Kim, Effect of Long Time Annealing and Incident Light Intensity on the Performance of Polymer: Fullerene Solar Cells, IEEE Transactions on Nanotechnology. 9 (2010) 400-406.
[9] C.N. Hoth, S. a Choulis, P. Schilinsky, C.J. Brabec, High Photovoltaic Performance of Inkjet Printed Polymer:Fullerene Blends, Advanced Materials. 19 (2007) 3973-3978.
[10] N. Moldovan, R. Picos, E. Garcia-Moreno, Parameter Extraction of a Solar Cell Compact Model usign Genetic Algorithms, in: Spanish Conference on Electron Devices, 2009. CDE 2009, IEEE, 2009: pagg. 379-382.
[11] T. Aernouts, T. Aleksandrov, C. Girotto, J. Genoe, J. Poortmans, Polymer based organic solar cells using ink-jet printed active layers, Applied Physics Letters. 92 (2008) 033306.
[12] Lange, A., A new approach to the solvent system for inkjet-printed P3HT:PCBM solar cells and its use in devices with printed passive and active layers, Solar energy materials and solar cells. 94 (2010) 1816-1821.
[13] S.H. Eom, H. Park, S.H. Mujawar, S.C. Yoon, S.-S. Kim, S.-I. Na, et al., High efficiency polymer solar cells via sequential inkjet-printing of PEDOT:PSS and P3HT:PCBM inks with additives, Organic Electronics. 11 (2010) 1516-1522.
[14] J. Liu, Y. Shi, Y. Yang, Solvation-Induced Morphology Effects on the Performance of Polymer-Based Photovoltaic Devices, Advanced Functional Materials. 11 (2001) 420-424.
[15] R.D. Deegan, O. Bakajin, T.F. Dupont, G. Huber, S.R. Nagel, T.A. Witten, Capillary flow as the cause of ring stains from dried liquid drops, Nature. 389 (1997) 827-829.
[16] H. Hu, R.G. Larson, Marangoni Effect Reverses Coffee-Ring Depositions, The Journal of Physical Chemistry B. 110 (2006) 7090-7094.

[17] J.A. Lim, W.H. Lee, H.S. Lee, J.H. Lee, Y.D. Park, K. Cho, Self□Organization of Ink-jet-Printed Triisopropylsilylethynyl Pentacene via Evaporation□Induced Flows in a Drying Droplet, Advanced Functional Materials. 18 (2008) 229-234.

[18] D. Kim, S. Jeong, S.H. Lee, J. Moon, J.K. Song, Ink-jet printing of organic semiconductor for fabricating organic thin-film transistors: Film uniformity control by ink composition, Synthetic Metals. 159 (2009) 1381-1385.

CONCLUSIONS

The present thesis work concerns the realization and characterization of organic electronic devices fabricated by means of inkjet printing technique. The experimental results pointed out that the characteristics of this technology makes it versatile for the manufacturing of different devices like sensors, field effect transistors, solar cells and optical structures.

The focus of this research is the feasibility study on the control of the morphology and the uniformity of printed materials acting on the ink chemico-physical parameters (solvent composition, viscosity), on printing parameters (substrate temperature, drop emission frequency, drop overlapping degree, number of the overlapped layers) and on substrate properties (wetting, surface energy, roughness). The methodology for optimizing the working parameters is studied for each manufactured device since these parameters act in different way on the various ink/substrate systems. The right combination of these parameters allows to obtain the more appropriate morphology for each application, sometimes inducing also microstructural modifications, which are the main responsible of the final device working.

For the realization of the sensor devices, a polymer nanocomposite (PNC) was used as sensing material for fabricating VOCs (volatile organic compounds) chemiresistive sensors. The polystyrene (PS)/carbon black (CB) based ink was printed on different substrates, non-flexible (alumina, glass) and flexible (PET (polyethylene terephthalate), glossy paper). By depositing one or more lines of PNC based ink, differently orientated with respect to the fingers of the interdigitated electrodes, the relation between the sensing material geometry and the device

performances was studied. The results pointed out that the PNC based chemical sensors fabricated by IJ printing lines ‘transverse’ to the transducer fingers showed the best electrical performances when exposed to organic vapours. This optimized configuration was used for studying the effect of the substrate morphology on the printed film quality and, hence, on the device performances. The substrates employed were glass, PET and glossy paper and they were used untreated and after plasma treatments (O_2, CF_4). The optimized condition to obtain a continuous and uniform deposition of the sensing material was reached by CF_4 surface treatment. By combining this condition with the optimization of geometry and thickness of the printed layer, it was possible to improve the sensing material morphology and, hence, to enhance the sensor performances. All the sensors realized showed good electrical responses to acetone and ethanol vapours. In particular, the sensors inkjet printed on glossy paper showed the best electrical responses to the different analytes opening new perspectives for food distribution, electronics and textile industry applications. The study developed in the sensor field highlighted the peculiarity of this innovative technology in performing patterns which are exclusive of this deposition method and which allow to realize optimized architectures for enhancing the device performances. Moreover, the analysis on the surface treatments pointed out that the chemico-physical properties of the substrate have a key role in printing process since these parameters control the wetting and so the right adhesion of the sensing material.

The research activity related to the optical applications was focused on the realization of microlenses by additive deposition of a optical grade polymer material and on the structuring of polymer layers by means of inkjet etching (IJE), an application of IJP technology. The IJE technique consists in depositing drops of solvents or solvent mixtures onto a soluble polymer layer, inducing the local dissolution of the polymer with a final redistribution whose shape depends on the surface tension properties of the solvent mixtures. Concave- and convex- shaped microstructures were realized by using single solvents (N-Methyl-2-pyrrolidone (NMP), toluene (TOL)) and solvent mixture (TOL:NMP), respectively. The effects of the substrate temperature and the number of the printed droplets on the geometrical parameters of the microstructures were investigated. As application, the

concave-shaped structures were employed as texturing of polymer under-layer of OLED devices in order to destroy the interference effects observable in the device emission spectrum. The convex-shaped microstructures were used as microlenses coupled to OLED devices in order to improve the OLED out-coupling efficiency.

Concerning the optical structures realized by additive deposition, microlenses were fabricated by inkjet printing drops of PMMA (Poly(methyl methacrylate)) dissolved in different solvents (toluene -TOL-, N-Methyl-2-pyrrolidone -NMP-, chlorobenzene -CB-, ortho-dichlorobenzene -DCB-) and their mixtures (NMP:TOL, CB:NMP, CB:DCB, DCB:TOL, NMP:DCB). The substrate was glass covered by a transparent hydrophobic film with the aim to freeze the printed droplet. During the printing, the substrate temperature was kept at 17 °C in order to increase the drying time so improving the microstructure quality. The effects of the ink viscosity and solvents on the optical quality of the structures were investigated by profilometric and optical analyses. In particular, the results pointed out that the surface tensions properties of the solvents and the viscosity of the solutions are main responsibles of the shape and of the spherical symmetry of the microlenses. The optical properties of such microlenses were analyzed through a Mach–Zehnder interferometer in confocal configuration. This analysis allowed to evaluate the wave aberrations of the realized microlenses with respect to an ideal spherical shape and the results demonstrated that the right choice of the solvent and the polymer concentration in preparing the ink can enhance the optical quality of the microlenses. The activity related to optical application pointed out that the chemico-physical ink properties, which can suitably modified by formulating the ink by means of the right solvents, strongly influences the optical quality of microstructures manufactured by highly reproducible deposition method.

The research activity about OFETs was focused on the formulation and processing of a n-type semiconductor material based on Cyanated Perylene Carboxylic Diimide derivative, soluble in organic solvents and with good electrical properties and air stability. This study pertained the definition of the ink chemico-physical properties combined with the printing parameters in order to improve the quality of the printed layer. Films of N,N’-bis(n-octyl)-1,6-dicyanoperylene-3,4:9,10-bis(dicarboximide) (PDI-8CN2) were printed by solution prepared with different solvent mixtures

(dichlorobenzene (DCB), chloroform (CF)) on Si (gate)/bare SiO_2 (dielectric)/Au (contacts) substrates for the fabrication of n-channel organic transistors. For each mixture composition the printing parameters, such as substrate temperature and drop overlapping degree, were optimized to define the reproducibility condition of the deposition process and to improve the structural quality of the films. Morphological analyses were performed by means of polarized optical microscopy, scanning electron microscopy (SEM) and atomic force microscopy (AFM). The identification of the optimized ink composition was demonstrated to induce a specific morphology of PDI-8CN_2 films where larger grain domains are intercalated with smaller crystallites mostly oriented along the printing direction. The analysis of the electrical responses indicated that the devices fabricated by the optimized solvent mixture of DCB:CF have higher electrical performances, depending on the improved molecular organization at the interfaces between gold and the organic semiconductor.

The research activity related to the OPV was focused on the realization of solar cells by printing P3HT:PCBM blend as active material. The study was focused on the optimization of the device performances by employing different solvents and solvent mixtures to dissolve the blend. The effects of the working parameters on the electrical performances of devices were investigated by means of optical and morphological analyses. The results indicated that the employment of the right solvent mixture greatly influence the film morphology and the solar cell performances. Such behaviour was due to optimum phase separation of the two blend components, improved light absorption properties and reduced recombination losses that are attributed to an improved morphology and charge transport. Both OFET and OPV activities highlighted that the control of the ink and printing parameters is crucial for the morphological and, mainly, structured quality of the printed active material.

ACKNOWLEDGEMENT

“The time you spend on helping others is time gained”….

…“Il tempo che usi per aiutare gli altri è tempo guadagnato”. Così recita un bigliettino dei baci perugina (e chi mi conosce sa che è proprio nel mio stile cominciare così!). Ed è questo motivo che mi spinge a scrivere i ringraziamenti: per dire GRAZIE a tutti quelli che hanno speso il loro tempo per aiutarmi e farmi crescere… non è stato tempo perso ma tempo guadagnato! ☺

Il primo grazie va ovviamente a Carla che mi ha permesso di passare questi 3 anni in ENEA e che ho imparato in questi anni ad apprezzare per la sua bontà.

Un MEGA ringraziamento va a Fulvia che mi ha seguito e guidato per tutti questi anni, facendomi crescere sia professionalmente che personalmente. So di non sbagliarmi quando dico che è una delle persone più forti, intraprendenti e affettuose che io conosca. Grazie di cuore!

Un grande ringraziamento va anche ad Antonio C. che mi ha seguito come mio tutor in questo “viaggio” durato 3 anni.

E come dimenticare il mitico Mario B. Grazie per tutti i tuoi consigli e spiegazioni. Ho imparato veramente tanto grazie a te!TNK.

E un grazie va a Fausta, una persone più buone e “felici” che abbia mai conosciuto, grazie dell’aiuto, delle chiacchierate e della compagnia nei viaggi in treno. TVB

E grazie anche ad Anna e Peppe Nenna, che mi hanno sopportato in questi anni, sempre pronti ad aiutarmi in tutte le mie richieste. Lo so che a volte sono stata insopportabile e perciò vi meritate un SUPER-MEGA GRAZIE!

Grazie di tutto cuore al mio gigante buono Peppe P., una delle persone più volenterose, intraprendenti e soprattutto buone che conosco. Grazie di tutto!

Un grazie al mio compagno di “bis colazione!”, Peppe. Grazie dei tuoi consigli e delle chiacchierate in cima alle scale che mi hanno fatto capire molte cose!

Un grande grazie va a Pasquale e Rosita. Lavorare con voi mi ha permesso di apprezzare la vostra passione per il lavoro e mi ha spronato ad impegnarmi sempre di più. Grazieeee!!

E poi come dimenticare Antonio I., sempre disposto ad aiutarmi ad ogni mia richiesta. Grazie della disponibilità e dell'amicizia. Sei un grande!

Un grazie a Emilia che, anche se per poco, ha condiviso le gioie e i dolori della convivenza di ufficio! Grazie della tua amicizia, infinita pazienza e dei tuoi consigli!

Un grazie va a Dante, Matteo, Michele, Ciro e a tutti quelli del "Centro di calcolo" che mi hanno potuto apprezzare i miei "Karaoke live" post pranzo anti abbiocco! "anima mia" è per voi!

Grazie anche ad Antonio D.G. per la sua collaborazione e la sua pazienza. Spero di non essere entrata nella tua lista nera in così poco tempo! Hihi

E grazie di cuore a Aneesh, Romina, Tommaso, Vera, Ettore, Tiziana, Paola per tutto l'aiuto, la pazienza e… ….i dolci che mi avete offerto!!!

E poi grazie ancora a tutti coloro che hanno condiviso i "lunghi viaggi verso casa": Antonio, Carla, Franco, Grazia, Raffaele, Franco R., Giuseppe F., Danilo, Antonella, Gianni, e tutti coloro che per colpa dei miei poveri neuroni ho dimenticato.

E grazie devo dirlo anche alle mie amiche Laura, Tina, Katia, Mariateresa, Annarita, Giovanna ed Annapaola per le infinite chiacchierate ed uscite insieme.

E infine una SUPER-MEGA-GIGA ringraziamento va a Emanuele che in questi anni mi ha veramente sopportato e supportato in ogni momento. Il mio vero angelo sei tu.

GLOSSARY

Symbol	Full expression	Unit

Latin letters

d	Nozzle diameter	m
E	Energy	eV
f	Frequency	s-1
h	Height	m
L	Channel Length	m
n	Refractive index	-
M_w	Molecular Mass	-
R	Resistance	Ω
R_e	Reynolds number	-
SE	Surface Energy	mN m^{-1}
T	Temperature	°C
T_b	Boiling temperature	°C
V	Tension	V
W	Channel width	m
W_e	Weber number	-
Z	Fromm number	-

Greek letters

η	Viscosity	Pa s
η	Power conversion efficincy	
μ	Mobility	cm^2 V^{-1} s^{-1}
γ	Surface tension	N m^{-1}
θ	Contact angle	°
ρ	Density	Kg m^{-3}
τ	Shear stress	Pa
$\dot{\gamma}$	Shear rate	s^{-1}

Abbreviations

AFM	Atomic Force Microscopy
Au	Gold
BE	Bottom Emitting
BHJ	Bulk heterojunction
CB	Chlorobenzene
CB	Carbon black
CF	Chloroform

CF_4	Carbon tetrafluoromethane plasma
Cr	Chromium
CIJ	Continuous Inkjte
DCB	Dichlorobenzene
DLS	Dynamic Laser Scattering
DoD	Drop on Demand
EL	Electroluminescence
HOMO	Highest occupied molecular orbital
IJE	Inkjet etching
IJP	Inkjet printing
LoD	Limit-of-detection
LUMO	Lowest unoccupied molecular orbital
NMP	N-Methyl Pirrolidone
O_2	Oxygen plasma
OFET	Organic Field Effect Transistor
OLED	Organic Light Emitting Diode
OPD	Optical path difference
OPV	Organic photovoltaic
P3HT	poly(3-hexylthiophene)
PCBM	[6,6]-phenyl-C61-butyric acid methyl ester
PDI	Polydispersity index
PDI-$8CN_2$	n-type organic semiconductor
PEDOT:PSS	Poly(3,4-ethylenedioxythiophene):poly(styrenesulfonate)
PET	Polyethylene terephthalate
PI	Polyimmide
PMMA	Polymethyl methacrylate
PNC	Polymer Nanocomposite
ppm	Parts per million
PS	Polystyrene
PSC	Polymer solar cell
P-V	peak-to-valley
RMS	root-mean-square
RF	Radio Frequency
SEM	Scanning Electron Microscopy
Si	Silicon
SiO_2	Silicon Oxide
Si_3N_4	Silicon Nitride
TE	Top Emitting
TEOS/PFTEOS	Hydrophobic layer
TOL	Toluene
VOC	Volatile Organic Compounds
VRH	Variable Range Hopping Theory
ZnO	Zinc Oxide